Structure and Dynamics in Amphiphilic Bilayers: NMR and MD simulation Studies

Ferreira, Tiago

2013

[Link to publication](#)

Total number of authors:
1

STRUCTURE AND DYNAMICS IN AMPHIPHILIC BILAYERS
NMR AND MD SIMULATION STUDIES

Tiago Mendes Ferreira

Doctoral Thesis
2013

Avhandling för Filosofie Doktorsexamen
Naturvetenskapliga Fakulteten

The thesis will be publicly defended on Wednesday 5th of June 2013, in lecture hall B, 13.15 pm, Center for Chemistry and Chemical Engineering, Lund.
The faculty opponent is Dr. Klaus Gawrisch, Chief Director of the Laboratory of Membrane Biochemistry & Biophysics at the National Institute on Alcohol Abuse and Alcoholism, Maryland, USA.

Popular Science Summary

Drizzle a thin stream of olive oil into water. The oil splashes into tiny little drops first, and in a fraction of a second, they emerge from bulk to the surface, and then coalesce to form a thin layer. This phenomenon relates to the molecular properties of the liquids. Olive oil is composed, in a large extent, of molecules with a fierce name, triglycerides, which are built by a glycerol group and three fatty acid chains attached to it. Although glycerol alone dissolves in water, the fatty acid chains are insoluble which renders the olive oil immiscible in water.

Lecithins are natural molecules very similar to triglycerides, except for one of the fatty acid groups that is replaced by a water-soluble chain. Thus, when lecithins are mixed with water, a part of the molecules wants to be hydrated but their fatty acid chains will force their way to avoid any occasional contact with the water molecules.[1] This love/hate duality makes lecithin molecules to adopt a position that pleases both parties: they self-assemble into a two molecule thick bilayer film, with the insoluble parts forming an inner core of fat, and the water soluble parts directing outwards to the aqueous medium.

This thesis concerns how lecithins and other molecules with a similar love/hate duality towards water, behave within a fluid bilayer. Focus is put on applying and developing methods to find out how they displace themselves and how fast they move. The studies were carried out by combining two types of techniques. One uses an intrinsic property of particles called spin which can be accessed in a truly ingenious way by nuclear magnetic resonance (NMR) spectroscopy. The second method dismisses the real molecules, and instead calculates, through the single use of computers, how the molecules should move, in order to ultimately generate an atomic-detail computer animation of the bilayer.

If one can already watch the molecules in the computer why to worry with performing experiments then? This thesis delves around this and other related questions, and represents a little contribution as part of a wide effort to make the movies better.

---

[1]Scientific studies indicate that rather water wants to avoid fat but that's another story.

ACKNOWLEDGEMENTS

This thesis represents a five year journey a long way from home. During this time I met extraordinary people, scientific wise and personal, to whom I would like to express my deep gratitude.

- Daniel Topgaard, for guiding my way through the winding road of science and for sharing good ideas and good laughs.

- Samuli Ollila, for all the scientific discussions and support given.

- Robertinha, for the music and your tiny little bursts of frustration.

- Aleksandra, for the last minute samples and your comments on the thesis.

- To all the other co-authors in the papers with special thanks to Prof. Winchil Vaz.

- Gunnar Karlström, for his invariable good mood and coolness.

- The best working group possible - the Physical Chemistry Division.

- The Friends I made in Möllev and in the German Embassy, which made me feel good.

- Aos moto-ratos: o mestre Miguel e o puto Tiago; por me aturarem.

- Ao melhor da vida, os meus Pais, o João Miguel e a Ana Catarina.

LIST OF PUBLICATIONS

This thesis is based on the following papers, which will be referred to by their roman numerals in the text.

I **Cholesterol and POPC segmental order parameters in lipid membranes: solid state ^{1}H–^{13}C NMR and MD simulation studies**
Ferreira T. M., Gomes-Coreta F., Ollila O. H. S., Moreno M. J., Vaz W. L. C. , and Topgaard D..
Phys. Chem. Chem. Phys. **15**, 1976-1989 (2012).

II **Segmental order parameters in a nonionic surfactant lamellar phase studied with ^{1}H–^{13}C solid-state NMR**
Ferreira T. M., Medronho B., Martin R. W., and Topgaard D..
Phys. Chem. Chem. Phys. **10**, 6033–6038 (2008).

III **Molecular conformation and bilayer pores in a nonionic surfactant lamellar phase studied with ^{1}H–^{13}C solid-state NMR and MD simulations**
Ollila O. H. S., Ferreira T. M., and Topgaard D..
Manuscript.

IV **Model-free estimation of the effective correlation time for C–H bond reorientation in amphiphilic bilayers: ^{1}H–^{13}C solid-state NMR and MD simulations**
Ferreira T. M., Ollila O. H. S., Pigliapochi R., Dabkowska A., and Topgaard D..
Manuscript.

CONTENTS

Papers

INTRODUCTION

If a molecule is amphiphilic, its structure is composed of molecular blocks with an opposite behavior towards water, parts being water soluble others insoluble. Due to this duality, amphiphilic molecules self aggregate in an aqueous medium in a number of arrangements, such as spheres, cylinders, vesicles and liquid crystals to mention a few [1]. These different configurations for the self assembly have unique properties such as viscosity, light diffraction or rheological properties and the control of these properties may be useful for technological purposes [2].

The ultimate realization of amphiphilic nature is the structure of cells [3]. A myriad of bilayer shapes can be found throughout the organelles in the cytoplasm and all of these are kept as an agglomerate fenced by another bilayer, the plasma membrane. Inside the cell, these inner bilayers enclose spatial regions where different cellular processes take place and significant differences are found experimentally for their compositions [4]. Thus, the bilayer composition in different organelles should relate to their function. Also the molecular composition of plasma membranes varies throughout different cell types and living organisms [4].

The present view is that cell membranes are mainly composed of two key players, lipids and proteins. The more traditional perspective has been that function relates primarily to proteins. However, variations in lipid composition will affect the permeability of a membrane to different solutes and may also change the behavior of other molecules embedded in the lipid matrix, e.g. membrane proteins [5, 6]. Therefore, the structural and dynamical details of bilayers due to the molecular composition other than proteins is also of interest. This represents in great extent the motivation of the work that is here presented.

1.1 NMR and MD studies of bilayers

Nuclear magnetic resonance (NMR) spectroscopy has provided a great number of details of membrane model systems [7–10]. In terms of bilayer structure, one approach that has been particularly important, is the measurement of C–H bond order parameters, denoted S_{CH}, which give precise information on the orientation of C–H bonds in the bilayer by the definition

$$S_{CH} = \frac{1}{2}\langle 3\cos^2\theta - 1\rangle, \qquad (1.1)$$

where θ is the angle between the C–H internuclear vector and the principal axis of symmetry of the bilayer system. Such measurements have been done mostly by determining ^{2}H quadrupolar couplings from samples with ^{2}H isotopically labeled lipids [11, 12]. The first to report this ^{2}H NMR method on lipid bilayers were Seelig and Niederberger in 1974 [13] and the method has become widely used in various laboratories. Later, the development of dipolar recoupling methodology for magic angle spinning (MAS) NMR [14, 15] made possible to obtain S_{CH} values from samples with natural abundance of isotopes, and at present, it is achievable to ascertain complete S_{CH} molecular profiles, i.e. the S_{CH} values from all the distinct C–H bonds of a given molecule within a bilayer. These method developments are notable and a great number of experimental studies based on measurements of S_{CH} have been reported. A public database of such measurements has been made recently available by Leftin and Brown [16].

The interpretation of S_{CH} molecular profiles is not straightforward due to the S_{CH} geometrical definition. In the early beginning of these studies, the interpretation was done using statistical analysis of the molecular conformations accessible in a bilayer, many times supported by the use of Corey-Pauling-Koltun (CPK) molecular models made of wood or plastic [17]. At present time, the plastic models have been replaced by molecular dynamics (MD) computer simulations, a powerful method for picturing bilayers at the Ångstrom level of detail [18–21]. MD computer simulations provide, not only a static picture of simple bilayer systems with atomic resolution, but also how molecular structure evolves with time.[1]

The interplay between MD simulations of bilayers and experiments has enormous potential. On one hand, if the MD simulations predict atomic trajectories from which correct experimental values may be calculated, there is strong possibility that these trajectories represent reality. On the other hand, if the simulated and experimental quantities do not match, it means that either the

---

[1] Among the fabricators of plastic, wood and wire frame molecular models manufactured in the 70's, there were two which were actually providing battery-operated products to use as molecular dynamics visualizers, one of them entitled " The Molecular Dynamics Simulator ". [22]

simulations or the experiments were not correctly performed, which hints for further work. With respect to NMR, up to date, the most important tests for validating the structures predicted by simulations have been done by means of calculation of order parameters S_{CH} [16]. For validation of the time-scales of motion in the simulations, comparisons of NMR spin-lattice relaxation rates R_1 have been employed by the determination of time correlation functions [23, 24].

1.2   Aim and Outline

The aim of the work reported in this thesis is to apply and develop state-of-the-art methods to study the structure and dynamics of simple bilayer systems by combining nuclear magnetic resonance (NMR) spectroscopy with molecular dynamics (MD) simulations. The research presented has been done at the Physical Chemistry Division of Lund University from 2008 to the present date. All NMR experiments were conducted on an in-house Bruker Avance AVII-500 NMR spectrometer operating at a 1H frequency of 500.23 MHz. The MD simulations were performed in the LUNARC center for scientific and technical computing at Lund University.

The thesis is divided in two separate parts. The first part gives a basic description of the systems studied, and of the NMR and MD simulation methods used, setting the scientific background needed for the second part of the thesis, where the research is presented in a concise manner as follows.

- Paper **I** reports a study of the effect of cholesterol on a POPC bilayer. It is shown that the combined use of the INEPT and CP polarization transfer in R-type Proton Detected Local Field (R-PDLF) NMR spectroscopy enables to make a stringent comparison of NMR experiments with MD simulations by means of a large set of order parameters.

- Papers **II** and **III** aim to unravel structural features in nonionic surfactant bilayers made of pentaethyleneglycol mono n-dodecyl ether combining MD simulations and R-PDLF NMR experiments. The results and discussion center on the temperature dependence of the bilayers and on their overall structure.

- Paper **IV** presents a NMR protocol suitable for determining an intrinsic dynamical quantity of C–H bonds denoted effective correlation time, which enables to elucidate a very well defined quantity of the auto-correlation function for C–H bond reorientation in amphiphilic bilayers. Moreover, it is shown that the method can be extended further to demonstrate that it is possible to use spin lattice relaxation rates at the rotating frame $R_{1\rho}$, in addition to spin lattice relaxation rates R_1, to validate MD simulations of lipid bilayers.

AMPHIPHILIC BILAYERS

Some types of amphiphilic molecules can aggregate in aqueous media into a fluid bilayer. A bilayer is a film two molecules thick where molecules arrange themselves with their hydrophilic blocks directed outward to the aqueous environment, and hydrophobic parts inward forming an inner hydrocarbon core. As seen at a nm length scale, a bilayer is normally a planar sheet, but at longer length scales of μm or higher, bilayer films may be found in various morphologies. Simple examples are planar lamellae stacks, single uni-lamellar vesicles, or onion-like structures called multi-lamellar vesicles [1, 25, 26]. More complex bilayer topographies occur in living cells [3]. In this chapter, a description of the structure and motion of amphiphilic molecules in bilayer systems is presented.

2.1 Self-Assembly

From a thermodynamics point of view, molecules self-assemble in liquid mixtures of amphiphiles and water to lower the free energy of mixing [1, 25, 26]. The driving force for self-assembly is the low solubility of the molecular hydrophobic moieties, the so-called hydrophobic effect [25], and the aggregation is counterbalanced by the solubility of the hydrophilic parts. Due to such duality, rather than attaining complete macroscopic phase separation as in mixtures of oils and water, an amphiphile-water system reaches equilibrium by means of self-assembly organization on the nanometer scale. The formation of fluid bilayers is one of such type of arrangements.

The self-assembly structure adopted by a given amphiphilic system depends on multiple factors [1, 25–27]. At amphiphile concentrations close to the so-called critical micellar concentration (CMC), at which the aggregation starts to occur significantly, it depends mostly on two [1, 26]. A surface free energy contribution, describing a balance between: an attractive interaction, due to
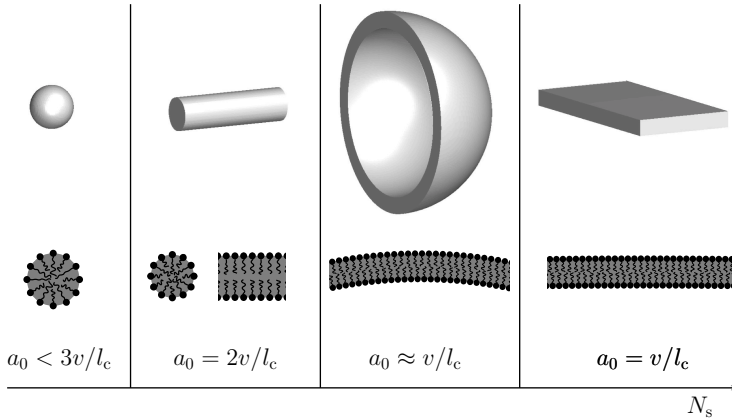
Figure 2.1: The self-assembly structures predicted by Israelachvili's packing parameters $N_s = v/a_0 l_c$ [27]. Although, in terms of packing requirements, all structures are allowed at $a_0 < 3v/l_c$, spherical micelles are formed due to the entropic increase in free energy. At higher N_s values, less entropically favored structures are preferred over smaller aggregates due to packing restrictions. The tiny black circle and twisted line are used to schematically represent the head group and tail of an amphiphilic molecule, respectively.

the hydrophobic effect, and a repulsive interaction due to repulsions at the surface e.g. electrostatic or steric repulsions among head groups[1]. And a second contribution due to the packing arrangement of the tails in the hydrophobic core of the aggregate.

To help rationalize why different morphologies are adopted in favor of others, Israelachvili et al. [27] introduced a dimensionless quantity, the packing parameter or shape factor N_s, which relates three physical quantities of an amphiphile as

$$N_s = \frac{v}{l_c a_0}, \tag{2.1}$$

where v is the volume occupied by the amphiphilic molecule in the hydrophobic core of the aggregate, l_c is the maximum length of the amphiphile's hydrophobic chain, and a_0 represents the area per head group of the aggregate. By knowing N_s, one may exclude the formation of certain aggregate morphologies due to geometrical packing restrictions. And from the set of possible aggregates left, one could expect the occurrence of the smallest possible morphologies, i.e. the aggregates with highest entropy gain. Figure 2.1 illustrates the self-assembly structures predicted for a number of cases.

---

[1]The terms head group and tail will be used as commonly done to denote the hydrophilic and hydrophobic parts of an amphiphilic molecule, respectively.

Although it is possible to roughly estimate l_c and v for a given amphiphilic molecule [1, 25, 26], there is no simple way to determine a_0 non-empirically since expressing the interfacial tension as a molecular property is difficult. In practice, by observing experimentally the structures into which a given amphiphilic molecule assembles, it is possible to infer about its a_0 and also to interpret how a_0 is affected by changing conditions such as temperature or ionic strength. Most of biological lipids have a N_s approximately equal to 1, i.e. they never form spherical micelles or cylinders but readily aggregate as bilayer vesicles at dilute conditions [4]. Amphiphiles that form micelles or cylinders may also form bilayers at higher concentrations [2].

The two types of bilayer systems studied in this thesis may be separated in terms of N_s. One type is made of 1-palmitoyl-2-oleoyl-sn-glycero-3-phosphocholine (POPC), a phospholipid abundant in cell membranes, that readily aggregates into bilayer vesicles in water at concentrations as low as 10^{-7} M [4]. The second type is a solution of an alkylethylene oxide surfactant which assembles into micelles, at a CMC of around 10^{-5} M but which forms bilayer structures at higher concentrations [2].

2.2   Cell membranes

While prokaryotic cells lack any membranes other than the ones surrounding the cells, the higher degree of organization inside eukaryotic cells is achieved by a number of specialized membranes [3]. These membranes have exquisite shapes in contrast with the simple self-assembled structures shown above.

The main components of biological membranes are proteins and lipids, and their molecular composition depends on organelle and cell type as illustrated in Table 2.1. Although the content of protein in a biological membrane may be higher than the lipid (in weight %), often large parts of membrane proteins are hydrophilic and extend outward of the membrane plane. Therefore, it becomes reasonable to assume that a biological membrane is a lipid bilayer film with immersed proteins [1]. The composition of the lipid bilayer also depends on the species, cell and organelle types [3] and may even depend on nutrition and metabolic activity [29]. For instance, cholesterol is generally a major lipid in the plasma membranes of mammalian cells, with concentrations up to 45 mol% in total lipid content, although in endoplasmic reticulum membranes, the cellular site where cholesterol is naturally synthetized, it amounts to quantities around 10 mol% [31]. Cholesterol alone is not soluble in water, nor does it form amphiphilic aggregates (it has a solubility of 10^{-7} M), but mixed with phospholipids (another major class of lipids) it readily incorporates into the bilayers of phospholipid vesicles [31]. The effects of cholesterol in a lipid bilayer are good examples of how the lipid composition of a lipid bilayer
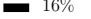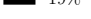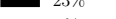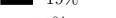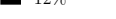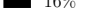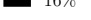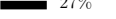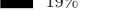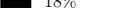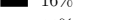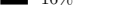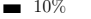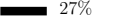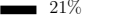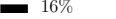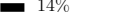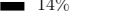
Membrane type	▬ Lipid ▬ Protein (% total dry weight)	Types of Lipid[†] (% total lipid weight)		Fatty acids in PC[‡] (% total PC weight)	
Plasma Membranes:					
Myelin (CNS)	79%	28%	Chol	52%	18:1
	18%	23%	GalCer	40%	16:0
		16%	PE		
		11%	PC		
Red Blood Cells	43%	31%	Chol	31%	16:0
	49%	20%	PC	23%	18:2
		19%	SM	19%	18:1
		19%	PE	12%	18:0
Mitochondria:					
Inner membrane	24%	38%	PC	27%	16:0
	76%	24%	PE	19%	20:4
		16%	PI	18%	18:0
		16%	CL	16%	18:1
				16%	18:2
Outer membrane	48%	46%	PC	27%	16:0
	52%	33%	PE	21%	18:0
		10%	PI	16%	20:4
				14%	18:1
				14%	18:2

Table 2.1: The lipid composition of different membranes. Data abstracted from references [4, 25, 28–30]. [†] Lipid abbreviations: cholesterol (Chol), galactocerebroside (GalCer), phosphatidylethanolamine (PE), phosphatidylcholine (PC), sphingomyelin (SM), phosphatidylinositol (PI), and cardiolipin (CL). Most of the chemical structures for these lipids are shown in Figure 2.2. [‡] Composition of PC lipids in terms of acyl chains $n{:}m$ with a length of n carbons and with m double bonds as in reference [4]. The compositions shown for myelin refer to myelin sheaths of axons in the central nervous system (CNS).

may change its properties (see for instance Paper **I** and references therein). Its presence orders the phospholipid hydrocarbon chains which increases the thickness, impermeability and viscosity of the bilayer [32, 33]. It may also affect membrane proteins by direct binding or indirectly by changing the elastic properties of the membrane [34]. Furthermore, it has been suggested that cholesterol induces the formation of lateral heterogeneities in the lipid bilayer, the so-called lipid rafts [35].

Glycerophospholipids   Sphingophospholipids   Cholesterol

PC: X=$(CH_2)_2N^+(CH_3)_3$ SM: X=$(CH_2)_2N^+(CH_3)_3$
PE: X=$(CH_2)_2N^+H_3$
PI: X=$CH(CHOH)_5 \bullet$ M
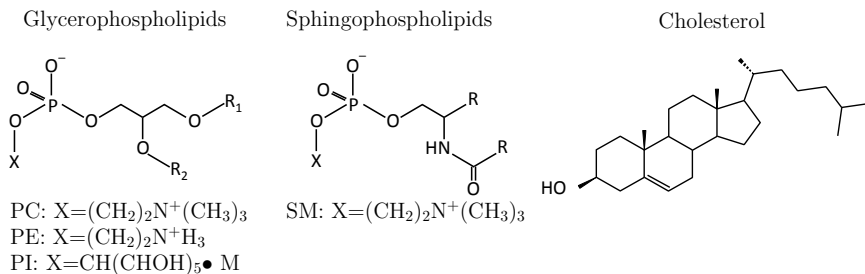
Figure 2.2: Chemical structures of naturally occurring lipids in living cells: Glycerophospholipids: Phosphatidylcholine (PC), Phostidylethanolamine (PE), Phosphatidylinositol (PI); Sphingophospholipids: Sphingomyelin (SM); and Cholesterol. For PI lipids, M is a monovalent cation or H. R_1 and R_2 may denote alkyl (R) or acyl (CO-R) chains. Acyl chains are usually represented by the numerical symbol $n{:}m$ denoting the total number of carbons n and number of double bonds m. Glycolipids, the other type of bilayer-forming lipids present in biological membranes, are not shown. To find a detailed description of their chemical structure and physical properties see e.g. reference [4].

Figure 2.2 shows the chemical molecular structures of cholesterol and of phospholipids that occur naturally in biological membranes. Most of the phospholipids in cellular membranes have two long hydrocarbon tails and are bilayer forming amphiphiles, i.e. they self-assemble into bilayer vesicles at dilute conditions. There are other phospholipids that occur in nature, albeit in lesser amounts, that have single or short hydrocarbon chains which form micelles [4]. Usually, most of the phospholipids in cells have at least one unsaturated hydrocarbon chain, which assures a liquid-like character to the lipid bilayer [25]. Some exceptions to this rule exist; for instance, alveolar cells are primarily composed of a phospholipid with two long saturated hydrocarbon tails [36].

The current understanding of cellular membranes in terms of lipid behavior is strongly supported by studies on simple model bilayer systems. Due to the extreme complexity of biological membranes, it is invariably difficult to make any relevant conclusions on the molecular level from investigations performed on real biological membranes only. Thus, the study of simple models, e.g. systems formed by a single type of phospholipid, and their behavior with respect to variables as composition, temperature and so forth, are important to support the studies on the more intricate biological systems [37–40].

The analogies between the model systems and real membranes need to be done with special caution. The model systems are most often studied in conditions of thermodynamic equilibrium, while the lipid bilayer state in biological

membranes is controlled by metabolic processes. For instance, the inner and outer leaflets of biological bilayers have different compositions that are maintained by flipases and flopases that sort distinct lipids between both sides of the bilayer [41, 42]. Even so, the information from simple models is invaluable since at present it is the only means of obtaining accurate information on the molecular level.

2.3 Molecular observables

A number of molecular properties may be experimentally obtained from amphiphilic bilayers. Here, emphasis is given to molecular properties that may also be calculated from molecular dynamics simulations within the current computation limits. Structural parameters are usually measured by X-ray and neutron diffraction [43] or NMR [8, 16, 44]. Dynamical observables have been measured with fluorescence recovery after photobleaching (FRAP) [45], Electron Spin Resonance (ESR) [46], and NMR techniques [8, 16, 44]. Rather than presenting the experimental methods in detail, a concise definition of the most relevant observables is given in the following subsections. Static observables, i.e. quantities which may be defined equally by ensemble or time averages, and dynamical observables are described separately.

2.3.1 Static

Distances and areas

At appropriate conditions, many amphiphiles form stable multi-layer vesicles (MLVs) in aqueous media, as illustrated in Figure 2.3, and/or lamellar phase (L_α) liquid crystals which are stacks of flat bilayers. Such systems may be subjected to measurements of the average repetition distance $\langle d_R \rangle$ between layers using X-ray or neutron diffraction techniques [1, 25]. In turn, the average bilayer thickness $\langle d_B \rangle$ may be estimated using the partial molal volumes of amphiphile $\bar{v}_A$ and water $\bar{v}_W$, and $\langle d_R \rangle$ in the expression [4]

$$\langle d_B \rangle = \langle d_R \rangle / \left(1 + \frac{\bar{v}_W}{\bar{v}_L} \cdot \frac{(1-c)}{c} \right), \tag{2.2}$$

where c is the weight fraction of lipid in the multilayer system. $\langle d_B \rangle$ and other average distances in the bilayer, e.g. the bilayer hydrophobic thickness $\langle d_C \rangle$, may also be resolved directly from scattering experiments on uni-lamellar vesicles which are obtained by extrusion of MLVs through microporous filters [47].

The various distances that can be measured are normally used to calculate interfacial areas $\langle A \rangle$ of the amphiphilic molecules in the bilayer. This is generally done by using relations such as $\langle A \rangle = 2V_B/\langle d_B \rangle$, where V_B is the volume
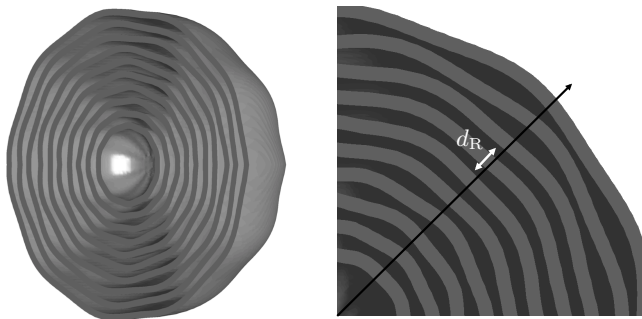
Figure 2.3: Repetition distance d_R in a multi-lamellar vesicle. For vesicles with two components, e.g. alternating layers of a given amphiphile and water, the measurement of $\langle d_R \rangle$ enables the estimation of the amphiphile's molecular area at the transverse plane of the bilayer.

that one amphiphilic molecule occupies in the bilayer, or equivalent expressions relating a given volume with the corresponding distance associated [47].

Order parameter S_{CH}

Order parameters can be accurately measured with atomic detail by a number of NMR techniques [12, 16, 44]. The order parameters measured for a given C–H bond may be expressed as the time average

$$S_{\mathbf{cl}} = \langle P_2(\cos \theta_{\mathbf{cl}}) \rangle, \tag{2.3}$$

where $P_2(\cos \theta_{\mathbf{cl}}) = \frac{1}{2}(3 \cos \theta_{\mathbf{cl}}^2 - 1)$, is the second Legendre polynomial of the cosine of $\theta_{\mathbf{cl}}$ that is the angle between the C–H bond vector $\mathbf{c}$ and the laboratory frame axis $\mathbf{l}$ defined by the direction of the external magnetic field $\mathbf{B_0}$ used in the NMR setup. The average is taken over time lengths around 100 μs or less depending on the NMR method used. As it will be shown below, during such a short time interval, an amphiphilic molecule diffuses laterally in a bilayer no more than a distance of 10–100 nm. Thus, with respect to the time average in Equation 2.3, a phospholipid MLV or a L_α liquid crystal, can both be considered as a set of liquid crystallite sites with dimensions below or approximately equal to 100 nm. Most of the macroscopic samples studied contain a distribution of crystallite sites with different alignments. For a given liquid crystallite, $S_{\mathbf{cl}}$ is given by

$$S_{\mathbf{cl}}(\theta_{\mathbf{dl}}) = S_{CH} P_2(\cos \theta_{\mathbf{dl}}), \tag{2.4}$$

where $\theta_{\mathbf{dl}}$ is the angle between the symmetry axis director $\mathbf{d}$ of the crystallite and the external magnetic field, and where the C–H bond order parameter S_{CH} is as defined in Equation 2.3 but in terms of the angle $\theta_{\mathbf{cd}}$ between the C–H

A. $\theta_{\mathbf{dl}}$ B. $\theta_{\mathbf{nd}}$ C. $\theta_{\mathbf{cn}}$
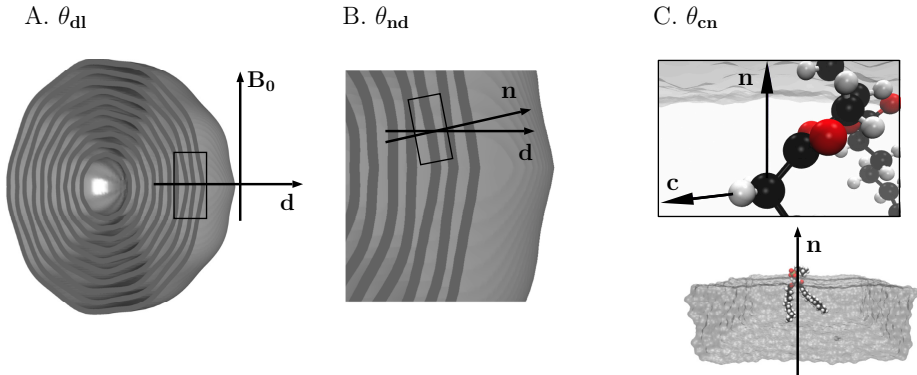
Figure 2.4: Illustration of the three angles that may be used to describe the orientation of C–H bonds in respect to a given laboratory frame axis **l**. (A) $\theta_{\mathbf{dl}}$ denotes the angle between the symmetry director axis **d** of a liquid crystallite site and the fixed laboratory axis frame **l** defined by the direction of the external magnetic field $\mathbf{B_0}$. (B) $\theta_{\mathbf{nd}}$ denotes the angle between a molecular frame axis with the direction of the bilayer normal **n** and the symmetry director axis **d**. (C) $\theta_{\mathbf{cn}}$ represents the angle between the chemical bond principal axis of a given C–H pair and the bilayer normal **n**. NMR order parameters $S_{\mathbf{cl}}$ are time averages taken at short time intervals below 100 μs through which molecules diffuse slowly at restricted sites. During short times, around 10-100 ns, C–H bond reorientation is exclusively due to the variation of the angle $\theta_{\mathbf{cn}}$ by means of fluctuations in C–C torsion angles and overall wobbling of the molecular segments. At longer time scales, variations of $\theta_{\mathbf{nd}}$ due to lateral diffusion can also contribute to the time averaging of order parameters.

bond vector **c** and the director axis **d**. It is possible to experimentally determine S_{CH}, by using liquid crystals composed of crystallites oriented at a single angle $\theta_{\mathbf{dl}}$, or by using liquid crystals composed of randomly oriented crystallites as in e.g. MLVs. [48].

For the purpose of interpreting S_{CH}, it is useful to further decompose it in the product

$$S_{\mathrm{CH}} = S_{\mathbf{cn}} S_{\mathbf{nd}}, \tag{2.5}$$

where $S_{\mathbf{cn}}$ denotes an order parameter with respect to the angle $\theta_{\mathbf{cn}}$ between the C–H bond vector and the instantaneous local bilayer normal **n**, and $S_{\mathbf{nd}}$ is defined by the angle $\theta_{\mathbf{nd}}$ between **n** and the director **d** of the liquid crystallite. $S_{\mathbf{cn}}$ depends on the internal motions in the amphiphilic molecules and the overall molecular wobbling, while $S_{\mathbf{nd}}$ accounts for contributions from fluctuations of the instantaneous bilayer normal due to e.g. lateral diffusion of the amphiphilic molecules. The angles $\theta_{\mathbf{dl}}$, $\theta_{\mathbf{nd}}$ and $\theta_{\mathbf{cn}}$ are illustrated in Figure 2.4.

The angle $\theta_{\mathbf{nd}}$ may be equal to zero over the time interval for averaging, as illustrated in Figure 2.4B, or may change as exemplified in Figure 2.5. S_{CH} val-

ues can therefore be interpreted as consequence of conformation effects, thermal wobbling of the molecules, and due to the geometry of the bilayer surface. It is not possible to measure S_{cn} and S_{nd} separately, nevertheless, Equation 2.5 is useful as a conceptual framework for analyzing S_{CH} values.
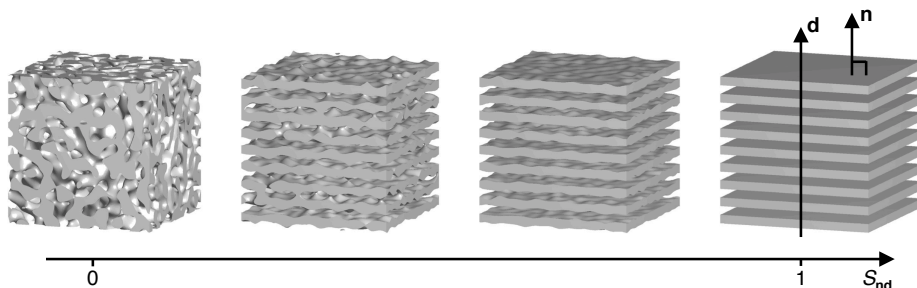
Figure 2.5: Illustration of the effect of perforations to the S_{nd} value in Equation 2.5. In the case of rough or perforated bilayer surfaces, also molecular diffusion may contribute to the averaging by changes of θ_{nd}. For a given liquid crystallite, θ_{nd} depends on the angle between a molecular frame axis n, defined as the direction of the local bilayer normal, and the symmetry director axis d of the liquid crystallite. Redrawn from reference [44] with permission.

2.3.2 Dynamics

Information about the time-scale of translational displacements of molecules in a bilayer as illustrated in Figure 2.6A can also be obtained. The time-scale of lateral displacements can be determined by measuring the lateral diffusion

A. Lateral diffusion
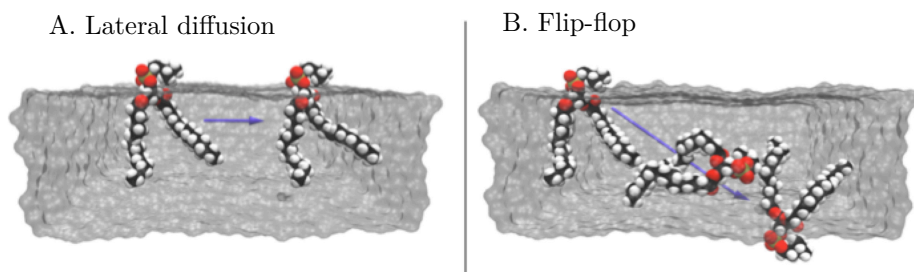
B. Flip-flop

Figure 2.6: Illustration of lateral diffusion displacements (left) and of flip flop dynamics (right). Mean square displacements for phospholipids in bilayers are on the order of μm^2 per second. Flip-flop diffusion is an extremely slow process on the order of hours or days.

coefficient D_T, which relates to the two-dimensional mean square displacement $\langle r^2 \rangle$ as $\langle r^2 \rangle = 4D_T t_T$, where t_T is the time step of the lateral displacement. Flip flop or transverse diffusion rates from one leaflet of the bilayer to the opposite can also be measured. Flip flop processes are extremely slow, and a phospholipid molecule remains on average around hours or even days without changing leaflet [4].

In addition to lateral and transverse diffusion, rotational diffusion of amphiphilic molecules also occurs. The reorientation of C–H bonds in a phospholipid bilayer may be analyzed in terms of the auto-correlation function

$$g(t) = \langle P_2[\boldsymbol{\eta}(\tau)\boldsymbol{\eta}(\tau + t)] \rangle, \tag{2.6}$$

where $\boldsymbol{\eta}(\tau)\boldsymbol{\eta}(\tau + t)$ is equal to the cosine of the angle between the C–H internuclear vector at time τ with itself at a time $\tau + t$. The expected behavior of $g(t)$ for a given C–H bond of an amphiphilic molecule in a bilayer, according to MD simulations, is shown in Figure 2.7. In Paper **IV** a solid-state NMR method is presented to measure the so-called C–H bond effective correlation time τ_e from bilayer systems. The τ_e definition for a given C–H bond is also depicted in Figure 2.7. The advantage of measuring τ_e in comparison to other rotational diffusion related C–H bond observables, is its simple (visual) definition and its model-free dependence. All other observables measured so far, have a more complicated interpretation in terms of correlation times, that generally depends on data fitting by the use of C–H bond motional models.
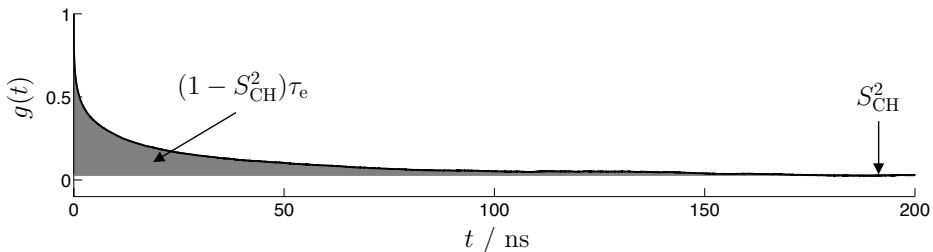
Figure 2.7: Example of an auto-correlation function for C–H bond reorientation in a lipid bilayer as predicted by a lipid bilayer MD simulation (Paper **IV**). The plateau at 200 ns is equal to the square of the C–H bond order parameter S_{CH}. The magnitude of the gray area reflects the time scale for reorientation and is usually defined as $(1 - S_{CH}^2)\tau_e$ with the parameter τ_e being normally called the effective correlation time. In a real system, for longer time scales of ms to s, $g(t)$ would decay to zero due to lateral and flip-flop diffusion processes.

2.4   Phospholipids

As shown in Table 2.1, phospholipids represent a large portion of the total lipids present in a cellular membrane. This section presents some factual data on their general properties and molecular observables. Phosphatidylcholines are emphasized in connection to the original results reported in Papers **I** and **IV**.

At room temperature all phospholipids form solid crystals and most types have high melting points, e.g long chain phosphatidylcholine (PC) lipids melt at temperatures around 235 °C [4]. Upon addition of water and depending on the phospholipid type, concentration and temperature, phospholipid molecules may assemble into micellar, hexagonal, lamellar, cubic and reverse hexagonal fluid phases [4, 49]. Long double chained PC lipids normally display lamellar phases only. Single chain PC lipids, termed lyso-PC, show a more complex lyotropic behavior and form micellar, hexagonal, cubic and lamellar phases [50].

2.4.1   Phosphatidylcholines

The chemical structure of phosphatidylcholines is shown in Figure 2.2. The molecular properties introduced above are here discussed for PC lipids with different fatty acid chains, giving quantitative examples for POPC (R_1=16:0 and R_2=18:1), DPPC (R_1=18:0 and R_2=18:0), DMPC (R_1=14:0 and R_2=14:0), and DOPC (R_1=18:1 and R_2=18:1) bilayers. Such type of comparison enables to illustrate effects such as adding double bonds to the acyl chains or increasing the acyl chain length while keeping the polar region of the bilayer fixed. The distribution of fatty acid tails in PC lipids found in nature varies for different organelles and cells as illustrated in Table 2.1.

Structure

Upon hydration, phosphatidylcholines may form MLVs as in Figure 2.3. The sizes observed for uni-lamellar vesicles are around 30 nm to 1 μm, thus the size range of MLV shells should be within these limits or higher [51]. The average distance $\langle d_\mathrm{R} \rangle$ between shells depends on hydration. For fully hydrated PC MLVs, $\langle d_\mathrm{R} \rangle$ is around 7 nm and depends on the hydration procedure adopted [52].

Recently reported values of molecular distances and areas, show for fully hydrated uni-lamellar vesicles of POPC, an area of approximately 64 Å^2, an overall bilayer thickness of 39 Å, and a hydrophobic thickness of 29 Å, at a temperature of 30 °C [47]. DPPC shows a gel phase at 30 °C reflecting the more efficient packing between linear saturated chains. At 50 °C, fluid bilayers are observed for both DPPC and POPC, and the hydrocarbon and bilayer lengths are equal for both systems, with the main contrast being the higher molecular area of POPC around 67 Å^2 in comparison to 63 Å^2 for DPPC. The

slightly higher molecular area of POPC is most likely due to the kink induced by the double bond in the unsaturated POPC acyl chain.

A large number of investigations based on order parameters S_{CH} of phospholipid bilayers have been reported, and a database for such measurements have been published recently [16]. A detailed description of the complete S_{CH} profile of POPC bilayers is given in Paper **I**. The S_{CH} values from the choline headgroup, glycerol backbone are very similar for different phosphatidylcholine systems. On the other hand, the acyl chain S_{CH} profiles vary strongly with acyl chain composition. This indicates the possibility of building phosphatidylcholine bilayers with very distinct hydrocarbon cores while maintaining the same structural properties of the polar region.

Since the beginning of NMR order parameter studies on bilayers, models have been proposed to convert order parameter profiles of saturated chains into projected overall lengths $\langle L_C \rangle$ (reference [53] and references therein). In Paper **I** the application of the mean torque model [53] to POPC order parameters yields a total projected length for its *sn*-1 chain of approximately 11.5 Å from the second acyl methylene to the methyl at the tip of the acyl chain. If a maximum length from the carbonyl carbon to the second methylene is assumed, for a non-interdigitated bilayer, a hydrophobic length of approximately 25.5 Å is obtained, which is 3.5 Å smaller than the value determined with scattering experiments. Such small difference might be attributed to both the gap between leaflets and the thermal motions of phospholipids in the direction perpendicular to the bilayer plane.

Dynamics

The lateral diffusion D_T is around 1-10 $\mu m^2/s$ in phospholipid bilayers. Since the radius of phospholipid MLVs of phospholipids generally range from 0.1-10 μm, depending on the MLVs preparation and phospholipid type [51], a phospholipid molecule in a MLV layer with such dimensions takes around 0.1-1 s to diffuse from an initial point in the vesicle to its antipode. Filippov et al. [54] measured the lateral diffusion coefficients of 5.7, 8.87 and 9.32 $\mu m^2/s$ for DMPC, POPC and DOPC bilayers, respectively, at 25 °C. The differences in D_T indicate that the unsaturation of phospholipid acyl chains makes phospholipids diffuse faster along the plane of the bilayer. In respect to transverse diffusion, flip flop half times of 3 to 15 days have been measured for fluorescent analogs of phosphatidylcholine in POPC bilayers at 25 °C.

Model dependent values of rotational diffusion in lipid bilayers have been reported previously for DMPC bilayers in terms of three correlation times: $\tau_{R\parallel}$ and $\tau_{R\perp}$ describing the overall rotation of the phospholipid molecules, and τ_J representing jumps between discrete conformations. Within this model, the values found for $\tau_{R\parallel}$ and $\tau_{R\perp}$ in the lamellar phase at 25 °C were 20 ns and 40 ns respectively and the values of τ_J was around 0.1 ns. Using the new method sug-

gested in Paper **IV** the first estimations of model-free effective correlation times in a phospholipid bilayer range from 0.1 to 3 ns in a POPC bilayer depending on the C–H bond location in the phospholipid molecule. Such measurement confirms a previous suggestion that the glycerol backbone and carbonyl groups form a rigid pivot of the phospholipids [55].

2.4.2   Cholesterol effect

If cholesterol is inserted into a phospholipid membrane, the phospholipid acyl chains become more stretched and the cross-sectional area of the phospholipid molecules in the bilayer plane decreases. Such observation is often referred to as the *condensing effect*. The cholesterol effect on phospholipid bilayers is highly dependent on the chemical structure of the phospholipid acyl chains. In bilayers of lipids with fully saturated acyl chains, e.g DPPC, DMPC, or sphingomyelin, inclusion of cholesterol to concentrations above 10 mol% induces a formation of two distinct liquid phases, the so-called liquid disordered and liquid ordered phases [54, 56, 57]. The disordered phase has a low concentration of cholesterol and has properties analogous to the pure phospholipid phase while the liquid ordered phase is cholesterol rich and displays highly stretched phospholipid hydrocarbon chains. These effects can be observed by measuring NMR order parameters since the different phases yield distinct order parameters and phase domains are big enough in respect to the time length for S_{CH} averaging. Such clear-cut NMR observations of two distinct phases are not achieved for unsaturated PC lipids, and at present, there is some controversy if whether any type of heterogeneities are also induced by cholesterol or not in unsaturated PC bilayers as discussed in Paper **I**. With respect to two-component systems, it has been clearly demonstrated that the inclusion of cholesterol in mixtures of DOPC/DPPC induces a phase separation into a liquid ordered phase rich in DPPC and a liquid disordered phase rich in DOPC [58]. More complex mixtures e.g. PC(18:0-22:6)/PE(18:0-22:6)/PI(18:0-22:6)/Chol, have also been investigated by means of NMR, from which it was suggested that cholesterol can form micro-domains with PC molecules and that it interacts more favorably with saturated chains [39].

In general, the variation of the C–H order parameters in respect to the cholesterol concentration in a POPC bilayer, show two clear trends. One is that the acyl chains become more ordered with the increase of cholesterol concentration in the bilayer. Second, that the glycerol and choline head group conformational structure is rather unaffected. On the other hand, it is shown in Chapter 5 (section 5.5.1) that while the rotational diffusion dynamics of the choline head group in a bilayer with 50 mol% of cholesterol are approximately the same as in a bilayer without cholesterol, the motions of C–H bond reorientations in the glycerol backbone become considerably slower.
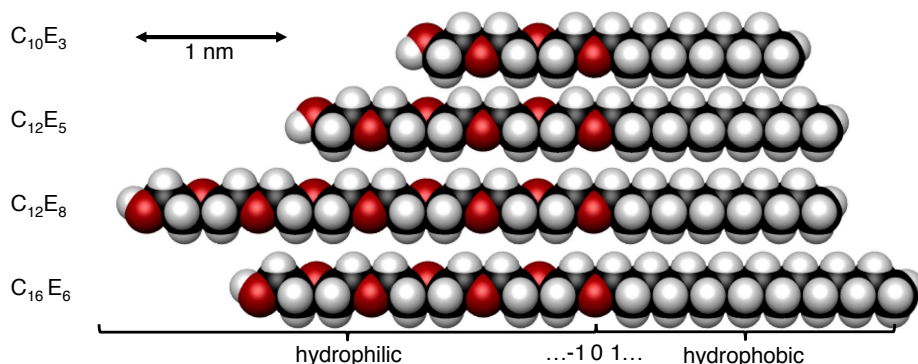
Figure 2.8: Representation of various grades of oligo(ethylene oxide) monoalkyl ether surfactants. All the original results from oligo(ethylene oxide) monoalkyl ether systems presented in this thesis reduce to $C_{12}E_5$. The carbon and oxygen atoms are normally numbered with respect to the origin defined at the oxygen labelled 0, with positive numbers denoting the alkyl chain and negative numbers labeling atoms in the hydrophilic part. Redrawn from reference [44] with permission.

2.5 Nonionic surfactants

The main difference between nonionic surfactants and phospholipids is the weaker strength of the interaction between water and the hydrophilic moiety, since by definition nonionic surfactants only bear partial localized charges. A more casual difference is the fact that most nonionic surfactants have only a single alkyl/acyl chain while most phospholipids are double-tailed amphiphiles.

2.5.1 Polyethyleneoxide-based surfactants

Polyethyleneoxide (PEO) based surfactants represent the class of nonionic surfactants that has been more extensively studied [2]. The simplest type of PEO-based surfactants are oligo(ethylene oxide) monoalkyl ethers with chemical structures as shown in Figure 2.8. PEO-based amphiphiles have been studied by multiple NMR methods, X-ray and light scattering techniques [1, 2, 44, 59, 60]. The early physical chemistry studies have focused mostly on phase behavior and its systematic dependence on the hydrophobic and hydrophilic sizes of the surfactants, or on intensive variables such as temperature and surfactant concentration [61]. PEO surfactants present a complex phase behavior and a particular C_nE_m grade may adopt a number of structures, some of which are illustrated in Figure 2.9. Temperature anomalies are specially exquisite [62]. One particular aspect of interest is the instability at high temperatures where a *cloud point* is reached, i.e. the amphiphile-water mixtures separate into a surfactant rich and a water rich phases. Controlling such effects by fine tuning of intensive variables

cubic micellar   2D hexagonal   lamellar   cubic gyroid
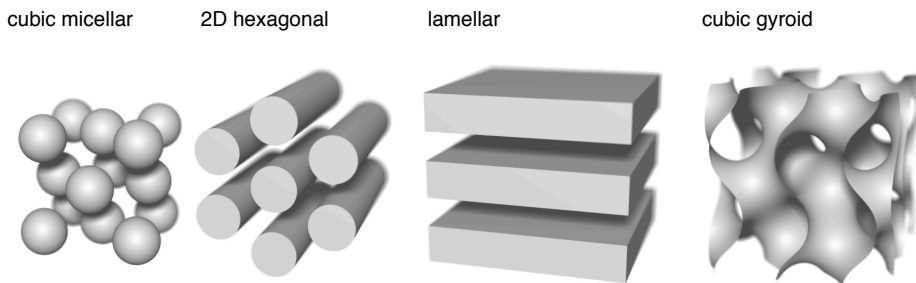
Figure 2.9: Illustration of some of the aggregation structures adopted by oligo(ethylene oxide) monoalkyl ether surfactants in aqueous media. Changes from one phase to another may be induced by variations of temperature or by varying the composition of surfactant and water. Increasing temperature leads to the sequence: spherical micelles, micellar cubic phase, elongated micelles, hexagonal phase, lamellar phase, bicontinuous cubic phase, sponge phase, and reversed micellar solution [61]. A given C_nE_m surfactant displays such sequence but often with some phases missing. Redrawn from reference [44] with permission.

or molecular size is of interest for a number of technological applications, e.g. in detergency methods or pharmaceutical formulations [2, 62].

Temperature effect

The temperature anomalies in PEO-based surfactants are normally attributed to the behavior of the hydrophilic ethyleneoxide groups. PEO molecules show a reversed solubility in water, i.e. at higher temperatures the solubility of PEO molecules decreases [62, 63]. From a thermodynamic view point, since the entropic contribution to the free energy of mixing increases with temperature, such decrease in solubility must be consequence of a temperature dependence of the enthalpy of mixing [1, 2, 62]. Three different underlying mechanisms to elucidate this behavior have been proposed [62]. Here, the suggestion of Karlström is adopted in order to interpret experimental results. Based on theoretical calculations and on solubility measurements of PEO in various solvents, Karlström suggested that the effect of a temperature increase on the distribution of PEO conformational states is to induce a decrease on the average polarity of EO groups [64, 65]. As consequence, in a PEO-based surfactant-water system there is a buildup of the hydrophobic effect with increasing temperature leading to the phase separation.

Bilayer permeability

The model proposed by Karlström and described above, can be used to interpret the temperature dependence of S_{CH} profiles from bilayers made of $C_{12}E_5$.
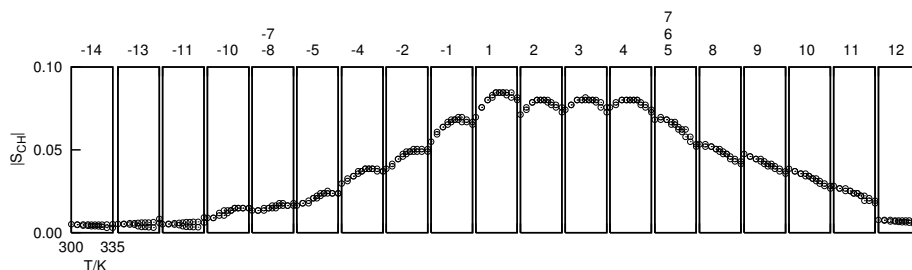
Figure 2.10: Temperature dependence of the complete $|S_{CH}|$ profile of $C_{12}E_5$ in a lamellar phase. Two values are shown for each temperature, one was measured while heating ant other while cooling down the sample. The labels on the top of each plot denote the distinct carbons in $C_{12}E_5$ according to Figure 2.8. Adapted from Paper **II**.

Such temperature dependence is rather striking. From the definition of S_{CH} in Equation 2.5, it is usually expected that an increase of temperature will induce a decrease on the order parameters by means of: an increase of the *gauche* configurations in the alkyl chain, which would induce a decrease on S_{cn}; or due to an increase on the fluctuations of the instantaneous bilayer normal **n** which would in turn decrease S_{nd}. It is however observed that in a $C_{12}E_5$ lamellar phase, the order parameter magnitude of C_1 (Figure 2.8 for labels) increases continuously throughout a temperature interval of 30-55°C to reach a maximum plateau value at approximately 55°C [66, 67]. From 55 °C on, towards the upper temperature boundary of the lamellar phase, the magnitude of S_{CH} then starts to decrease as normally expected. The temperature at which the $|S_{CH}|$ plateau value is reached was first interpreted as a boundary separating two distinct phases, a classic flat bilayer and the so-called random mesh phase where the bilayer displays porous defects [66, 67]. With the formation of pores, and due to an increase of pore size or density towards lower temperatures, S_{nd} would then decrease as observed due to the diffusion of molecules along pores. The possibility for pore formation in similar systems had already been suggested previously [48, 68–70].

Such observation motivated part of the work presented in this thesis (Papers **II** and **III**). By accessing further experimental information on the $|S_{CH}|$ profile from all the remaining carbon sites, a more complete picture emerges as shown in Figure 2.10. EO groups show generally an increase of $|S_{CH}|$ in respect to an increase of temperature, similarly to what had been previously observed for C_1, albeit with a shift of the plateau towards higher temperatures. On the other hand, the S_{CH} magnitudes of the remaining alkyl chain segments show a decrease, from the lower to the upper temperature limit of the lamellar phase, as it would be normally expected for a classical lamellar phase system. These

results strongly support the hypothesis suggested by Karlström described in the previous section, since the redistribution of PEO conformational states induced by temperature will cause a higher average extension or stretch of the PEO chains with subsequent increase of $|S_{\mathbf{cn}}|$. The question has been then posed, if the $|S_{\mathrm{CH}}|$ temperature dependence of the C_1 should be interpreted by means of $|S_{\mathbf{nd}}|$, due to the occurrence of two types of lamellar phases, a porous and a non-porous structure, or by $|S_{\mathbf{cn}}|$, due to the opposite trends induced by the conformational changes of the head group and tails.

To further understand the temperature effects, MD simulations were carried out using a recently reported force-field to describe PEO chains (Paper **III** for details about the MD simulations). The bilayers obtained in these simulations (Figure 2 in Paper **III**) have order parameters very close to the experimentally measured ones and therefore they may be taken as reasonable structural models. A number of perforations are indeed observed in these MD models at all temperatures investigated from 25 to 55 °C. Moreover, at low temperatures the pores become more extended. Thus, the dependence of $|S_{\mathrm{CH}}|$ on temperature is most likely originated by a combination of variations in $S_{\mathbf{cn}}$, due to the conformational changes, and in $S_{\mathbf{nd}}$ due to a change in pore surface area.

According to the MD simulations, at a temperature of 55 °C, the plateau value at which the classical lamellar phase should occur, the bilayers still display various perforations as illustrated in Figure 2.11. Thus, rather than two types of lamellar phase regions, most likely only one composed of bilayers with a high density of pores, occurs.

All the alkyl chain $|S_{\mathrm{CH}}|$ profiles that have been obtained from other C_nE_m bilayer systems, have very low magnitudes, normally half or less of those in bilayers e.g. of phospholipids or ionic surfactants [48, 66, 67]. Based on the above discussion, it is reasonable to assume that all C_nE_m bilayer systems will then be porous. Such generalization needs however to be well tested by performing both more experiments and MD simulations on different C_mE_n lamellar phases.
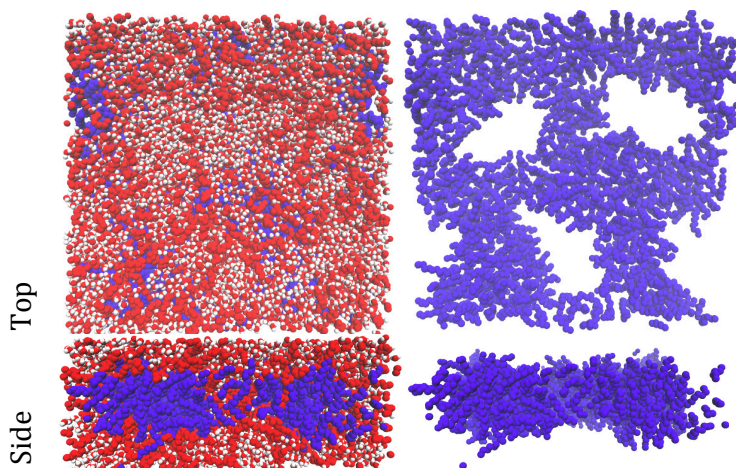
Figure 2.11: Side and top views of the structure of a $C_{12}E_5$ bilayer with 30 wt% of water at a temperature of 55°C predicted by a MD simulation as in Paper **III**. The left views show a van der Waals representation of all atoms and united-atoms used in the MD simulation with colors: red for the EO CH_2 united-atom groups and oxygen atoms, white for hydrogens and blue for alkyl chain CH_2 united-atoms groups. The right view shows only the hydrophobic core of the bilayer in order to depict the bilayer pores in the structure.

BASIC NMR

NMR techniques enable to access molecular information by means of nuclear spins. In modern NMR spectrometers the general scheme can be summarized in the following way. First, the sample under study is plunged into a region with a strong, static and homogeneous magnetic field. A perturbation is then applied by means of an electronic apparatus that generates pulses of radio frequency (RF) currents through a coil that surrounds the sample. The type of perturbation applied, i. e. the sequence of RF pulses used, depends on the molecular information desired. Directly after this perturbation, the evolution of the spin state of the system induces a Faraday induction in the coil. The frequency of the induced current generated is then downshifted through a quadrature detector, and the resulting complex analogue signal is digitally recorded. The information reported by the spins is posteriorly processed by Fourier transform analysis.

This chapter introduces the basic quantum theory for understanding a number of NMR experiments. The description is based on the textbooks of Levitt [71], Sakurai and Napolitano [72], Keeler [73], Duer [74], Kowalewski and Mäler [75], and Harris [76].

3.1 Spin

Spin is an intrinsic property of particles which was first postulated by Uhlenbeck and Goudsmidt in 1925. Although spin is a form of angular momentum, it cannot be understood as the more familiar concept of rotational angular momentum. A particle has an intrinsic spin S and its total spin angular momentum is constant and equal to $\hbar\sqrt{S(S+1)}$ [71]. Spin-1/2 particles have a total spin angular momentum of $\hbar\sqrt{3}/2$. The spin angular momentum is a vector, but unlike rotational angular momentum, this vector does not represent an axis of

rotation [71]. Magnetism is closely related to spin by the relation [71, 72]

$$\hat{\mu} = \gamma \hat{S} \tag{3.1}$$

which states that the magnetic moment of a particle is also a vector and is proportional to its spin angular momentum by a constant γ, the so-called gyromagnetic ratio of the particle.

3.2 Microscopic magnetization

The magnetic interaction of a macroscopic object which possesses a magnetic moment $\boldsymbol{\mu}$ with a magnetic field $\mathbf{B}$ is characterized by the energy [71]

$$E = -\boldsymbol{\mu} \cdot \mathbf{B}, \tag{3.2}$$

given by the dot product of the two vectors. A magnet, such as a compass needle, orients with the Earth's magnetic field to minimize energy. The effect of a magnetic field on the magnetic moment of a particle is however different because it has spin angular momentum. If the magnetic moment is tilted at a certain angle in respect to the external magnetic field, it remains at such angle but precessing around the field [71]. These two distinct behaviors are illustrated in Figure 3.1.
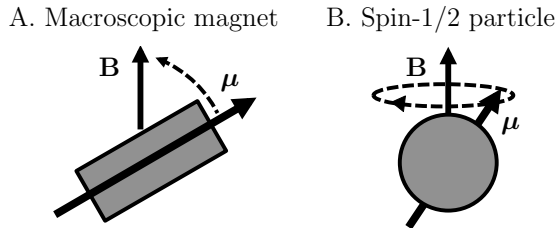
Figure 3.1: The effect of a strong magnetic field $\mathbf{B}$ on a macroscopic magnet and on a spin-1/2 particle. The precession of vector $\boldsymbol{\mu}$ is not to be confused with a rotation of the particle. A detailed description of the vector representation $\boldsymbol{\mu}$ used in (B) is given in section 3.3, and the frequency at which it precesses is introduced in section 3.4.

3.3 Spin representation

According to the quantum theory of angular momentum, the spin state of a spin-1/2 particle may be represented in a complex vector space in Dirac notation

by [72–74]

$$|\psi\rangle = c_\alpha|\alpha\rangle + c_\beta|\beta\rangle, \tag{3.3}$$

using the Zeeman basis eigenvectors defined by the eigenequations of the z–component of spin angular momentum:

$$\hat{I}_z|\alpha\rangle = \frac{\hbar}{2}|\alpha\rangle,$$

$$\hat{I}_z|\beta\rangle = -\frac{\hbar}{2}|\beta\rangle. \tag{3.4}$$

It is convenient to introduce a few rules from quantum mechanics [72]. The spin-1/2 particle will only have a well defined z–component of spin angular momentum if its spin state is either of the form $|\psi\rangle = c_\alpha|\alpha\rangle$ or $|\psi\rangle = c_\beta|\beta\rangle$ which will be $-\hbar/2$ and $\hbar/2$, respectively. If this is not the case, and the spin state is described by two non-zero coefficients c_α and c_β, the particle does not have a precise or sharp z-component of spin angular momentum [71], i.e. if the particle is manipulated to be in such a state, a single measurement of the z-component of its magnetic moment, $\hat{\mu}_z = \gamma\hbar\hat{I}_z$, may give one of two possible outcomes: $-\hbar\gamma/2$ or $\hbar\gamma/2$. It is possible however to know the average measured throughout a series of single measurements for any spin state $|\psi\rangle$ by the equation [72, 73]

$$\begin{aligned} \langle\hat{\mu}_z\rangle &= \langle\psi|\hat{\mu}_z|\psi\rangle \\ &= (c_\alpha^*\langle\alpha| + c_\beta^*\langle\beta|)\hat{\mu}_z(c_\alpha|\alpha\rangle + c_\beta|\beta\rangle) \\ &= \frac{\gamma\hbar}{2}(c_\alpha^* c_\alpha - c_\beta^* c_\beta). \end{aligned} \tag{3.5}$$

The same applies to the x– and y– components of spin angular momentum but in terms of their own eigenvectors. An illustration of these rules is given in Figure 3.2.

Another observation is that if a spin is manipulated to be say in a spin state $|\alpha\rangle$, although a single measurement of $\hat{\mu}_z$ performed to that state always yields $-\hbar\gamma/2$, if the x–component of the magnetic moment is measured before measuring $\hat{\mu}_z$, the spin state will change and the average outcome for such a mesurement of $\hat{\mu}_z$ becomes zero. The simultaneous measurement of more than one component of spin magnetic momentum is not possible, and the simultaneous definition of these components is forbidden by the quantum theory of angular momentum since the angular momentum operators $\hat{I}_x$, $\hat{I}_y$ and $\hat{I}_z$ do not commute.

Thus the magnetic moment vector $\boldsymbol{\mu}$ represented in Figure 3.1B is to be interpreted as a schematic picture of the spin polarization axis of a given spin state $|\psi\rangle$, by defining $\boldsymbol{\mu}$ as a vector with components equal to the average outcomes $\langle\hat{\mu}_x\rangle$, $\langle\hat{\mu}_y\rangle$ and $\langle\hat{\mu}_z\rangle$, respectively, if only single measurements, i.e. not
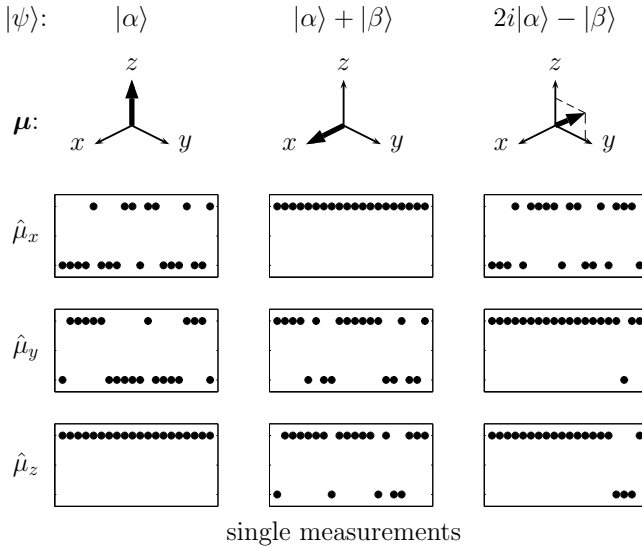
Figure 3.2: Illustration of single measurements performed to spin-1/2 particles manipulated to be in three distinct spin states. Such experiments are possible by e.g. performing Stern-Gerlach experiments [72]. Each point represents a single measurement after the particle has been manipulated to be in the state denoted on top. The states $|\psi\rangle = |\alpha\rangle$ and $|\psi\rangle = |\alpha\rangle + |\beta\rangle$ yield sharp values of $\mu_z = \hbar\gamma/2$ and $\mu_x = \hbar\gamma/2$, respectively. The state $|\psi\rangle = 2i|\alpha\rangle - |\beta\rangle$ does not give rise to any sharp expectation values in the used laboratory axis frame coordinate system. The vector representation $\boldsymbol{\mu}$ of the spin states is also shown.

as a sequence, are performed to a spin manipulated to be in such a state. Such vector representation is of extreme usefulness in NMR spectroscopy and is frequently used in most modern NMR textbooks [71, 73–75]. Note also that the vectors $\boldsymbol{\mu}$ and $\hat{\mu}$, used above, are not equal, one denotes a vectorial representation of a spin state and other the quantum operator of magnetic moment, respectively.

3.4 Spin precession

The evolution of the spin state of a given particle can be predicted by solving the equation of motion [73]

$$-i\hbar\frac{d}{dt}|\psi\rangle = \hat{H}|\psi\rangle, \tag{3.6}$$

where $\hat{H}$ is the Hamiltonian operator which represents the energy of the particle. The eigenstates of $\hat{H}$ are equal to the eigenstates of the z-component of angular momentum in a laboratory frame defined such that its z axis coincides with the magnetic field **B**. This choice of laboratory frame is recurrent in NMR spectroscopy and is also adopted here. For a single spin under the effect of a constant magnetic field **B**, $\hat{H}$ can be expressed as the Zeeman Hamiltonian [71, 73]

$$\hat{H}_{\mathrm{Z}} = -\gamma B_0 \hat{I}_z \tag{3.7}$$

where B_0 is the magnetic field strength. The solution of Equation 3.6 for the Zeeman Hamiltonian is [73]

$$|\psi(t)\rangle = c_\alpha(0)e^{-\frac{i}{2}\omega^0 t}|\alpha\rangle + c_\beta(0)e^{\frac{i}{2}\omega^0 t}|\beta\rangle, \tag{3.8}$$

with the coefficients $c_\alpha(0)$ and $c_\beta(0)$ defining the spin state at the time instant $t = 0$, and ω^0, in units of radians per second, as the frequency of spin precession

$$\omega^0 = (E_\beta - E_\alpha)/\hbar = -\gamma B_0/\hbar, \tag{3.9}$$

which is the frequency at which the vector $\boldsymbol{\mu}$ would precess in Figure 3.1B, referred to as the Larmor angular frequency and defined by the energy eigenvalues $E_\alpha = -\hbar\gamma B_0/2$ and $E_\beta = \hbar\gamma B_0/2$.

3.5 Magnetization

The frequency of spin precession ω^0 depends linearly on the magnetic field strength. In NMR experiments, samples which contain a very large number of spins, on the order of 10^{23}, are plunged into a strong, static and homogeneous magnetic field **B**, the inner part of the NMR magnet. When the sample is put in place, the spins instantaneously start to precess much more rapidly due to the increase in magnetic field strength.[1] Not as instantaneously, the net or bulk magnetization

$$\mathbf{M} = \sum_i \boldsymbol{\mu}_i, \tag{3.10}$$

where the sum is over the number of spins in the sample, starts to develop in the direction of the external magnetic field.

Such net magnetization buildup happens because in practice spins that are surrounded by other spins with thermal motions, never experience only a static magnetic field. Spins themselves generate a magnetic field due to their magnetic moments, and their thermal motions generates fluctuating magnetic fields in the surroundings. Because of these fluctuations, in a region with a very weak

---

[1]The difference depends on both the place where the experiment is done and the strength of the magnet used.
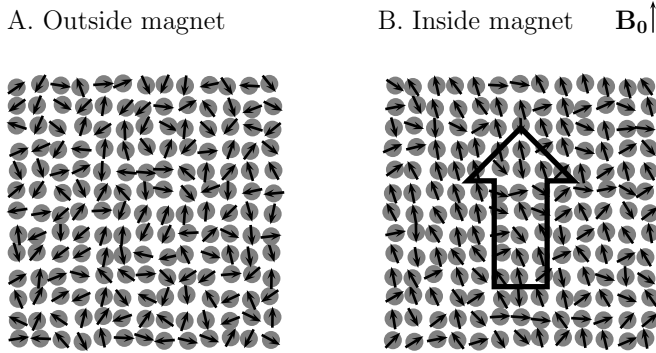
Figure 3.3: Net magnetization buildup by plunging a sample into a a region with a strong magnetic field. On average, the magnetic moments become slightly aligned along the field. The magnetic field strengths currently used in NMR spectrometers are around 1 to 20 T. Comparatively to the Earth's magnetic field of around 25 to 65 μT, the magnetization buildup becomes 10^5 times higher. The orientation distribution used in (B) is overly exaggerated for the purpose of a clear illustration of the biased orientations of spin vectors $\boldsymbol{\mu}$.

external magnetic field, the spin polarization axes are always randomly changing direction over time without a preferential orientation. When placed in a strong magnetic field, because the energy of the spins depends on the direction of their spin polarization axis, this wandering motion of the magnetic moments becomes biased; after some time there will be more spins pointing along the static field than opposite to it. Such process is illustrated in Figure 3.3. The magnetic field fluctuations, which depend on the thermal motion of spin particles, are the subject of relaxation NMR and will be discussed in Chapter 5.

3.6   RF pulses

The common way of manipulating spin states in NMR experiments is by applying RF fields which are perpendicular to the main magnetic field B_0. For an effective perturbation of spin states, the applied RF fields need to oscillate in resonance with the individual spin state precessions, and in experiments using nuclei with different gyromagnetic ratios, multiple coils and channels are needed performing at the Larmor frequencies of the distinct nuclei under investigation. The oscillation of RF pulses makes the Hamiltonian during a pulse to be time dependent which is undesirable in terms of calculating the pulse effect on the spin states. This can be circumvented by expressing the spin states and the

A. Equilibrium   B. After $(\frac{\pi}{2})\hat{I}_x$ pulse
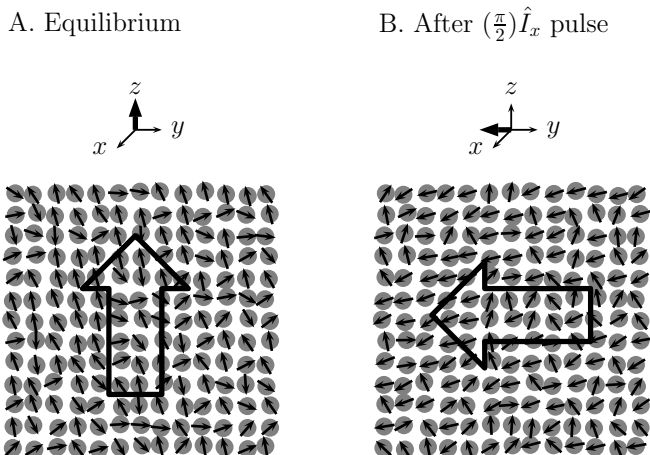
Figure 3.4: The effect of a 90° RF pulse to an ensemble of spins as observed using a rotating frame. Usually RF pulses with time lengths around 1-10 μs are used.

Hamiltonian in respect to a rotating frame at the Larmor frequency of spins. In this frame the magnetic moments are thus observed as static vectors in the absence of pulses (ignoring relaxation and offset effects), and the application of an RF pulse induces a counterclockwise rotation of magnetic moment vectors around the axis in which the pulse is applied. This is illustrated in Figure 3.4 for a RF pulse applied in the x direction. In experiments involving two nuclear species a double rotating laboratory frame is needed [74].

3.7   NMR signal and spectra

When the net magnetization vector is tilted from equilibrium e.g as in Figure 3.4, a coherent precession of individual magnetic moments will occur which generates an electromagnetic induction in the coil. In this condition, the transition frequency can be recorded using an analogue-to-digital converter (ADC) coupled to a quadrature receiver performing with a carrier frequency ω^{ref} close to the Larmor frequency of spins. Such measurement gives rise to the free induction decay (FID)

$$s(t) \propto e^{i(\Omega^0 t)} e^{-(R_2 t - \phi_{\text{rec}})}, \tag{3.11}$$

A. Precession   B. Signal acquisition   C. Spectrum
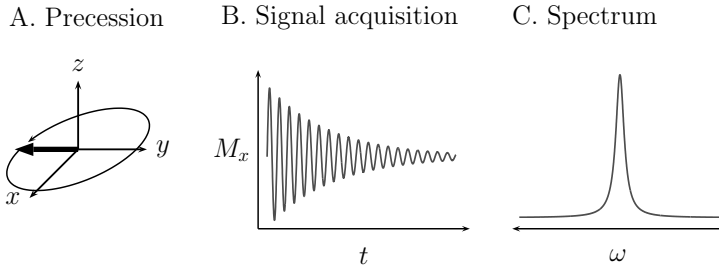
Figure 3.5: Illustration of the procedure to obtain a NMR spectrum (a single frequency is used for simplicity). After placing the magnetization vector at $-y$ with a RF pulse as in Figure 3.4, the magnetization starts to precess around z, the direction of the external magnetic field, with consequent oscillation of the M_x and M_y components at the Larmor frequency ω^0 and a decay due to R_2 relaxation. This generates an electromagnetic induction in the NMR coil with an alternating voltage at the frequency of precession. The NMR spectrum is then obtained by digitally recording such voltage in time and subsequently performing a Fourier transform to the recorded signal yielding a Lorentzian peak centered at ω^0. The linewidth of the peak depends on R_2 which in turn depends on the motion of the spins.

where Ω^0 is called the offset frequency from which the precession frequency can be estimated by the expression

$$\omega^0 \; = \; \Omega^0 \; + \; \omega^{\text{ref}}. \tag{3.12}$$

The other constants in Equation 3.11 are defined as follows. The decay rate of the signal is determined by R_2 referred to as the spin-spin relaxation rate constant. R_2 is connected to relaxation phenomena and will be described in more detail in Chapter 5. ϕ_{rec} is a user-defined receiver phase and from here on it will be assumed that it has been set equal to zero.

The analysis of such NMR signals is normally done by performing the Fourier transform

$$S(\omega) = \int s(t)e^{-i\omega t}dt, \tag{3.13}$$

to get the NMR spectrum, which is the real component of $S(\omega)$ and that can be expressed as

$$I(\omega) = \frac{R_2}{R_2^2 + (\omega - \omega^0)^2}, \tag{3.14}$$

after a normalization procedure. This is illustrated in Figure 3.5. In practice, since the spins are seldom independent of their surroundings, rather than being composed by a single frequency component, the signal is a sum of various

contributions with different frequencies, and accordingly the spectrum contains a number of Lorentzian peaks and may be expressed as

$$I(\omega) = \sum_i a_i \frac{R_{2i}}{R_{2i}^2 + (\omega - \omega_i^0)^2},$$

(3.15)

where the sum goes through all the distinct Lorentzian peaks centered at ω_i^0 and a_i are their corresponding amplitudes.

CHAPTER 4

STRUCTURAL NMR

One aspect that makes NMR a precious tool for molecular structure determination is the fact that the precession frequencies in Equation 3.15 depend on the orientation of molecules in respect to the external magnetic field. Since the macroscopic samples of amphiphilic bilayers often contain multiple sites with distinct alignments of the bilayer symmetry axis in respect to $\mathbf{B_0}$ (Figure 2.4), information about the order parameters $S_{\mathbf{cl}}$ in those sites (Equation 2.3) becomes readily accessible by NMR. Due to the local anisotropy of the systems, complex NMR spectra can be recorded, yielding various multiplets with splittings that are proportional to the order parameters.

4.1 ^{13}C NMR spectra of bilayer systems

The ^{13}C spins in phospholipid or surfactant bilayers cannot be normally treated as single independent spins due to couplings with other particles which also have an intrinsic magnetic moment e.g. protons or electrons. Thus, the Hamiltonian describing the energy of a ^{13}C spin is in practice more complex than the Zeeman Hamiltonian in Equation 3.7. Since the interactions between spins depend on their orientations, such Hamiltonian is time-dependent due to the motion of particles, which complicates solving Equation 3.6. However, according to a secular and motional average approximation procedure for independent ^{13}C–^{1}H spin pairs, it is possible to express the ^{13}C transition frequencies of fluid bilayers in respect to their orientation (see Appendix).
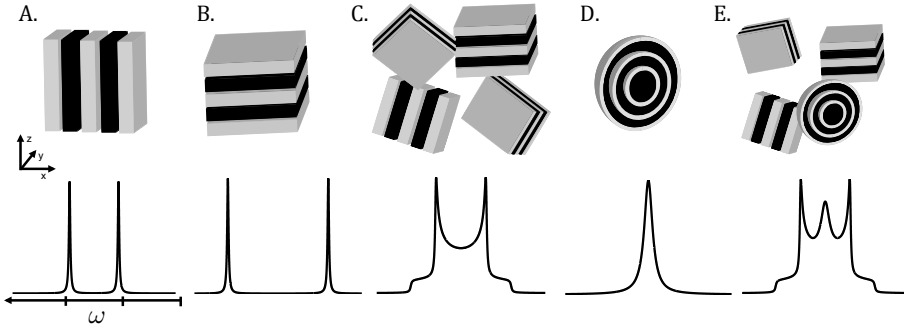
Figure 4.1: The influence of different bilayer arrangements on the ^{13}C NMR spectra of a given ^{13}C–^{1}H spin pair by means of the ^{13}C–^{1}H dipolar coupling. (A and B) Macroscopic samples with oriented lamellar phases exhibit doublets with splittings which depend on the bilayer alignment by $\Delta\omega(\theta_{\mathbf{dl}}) = (3\cos^2\theta_{\mathbf{dl}}-1)d_{\mathrm{CH}}S_{\mathrm{CH}}$ where $\theta_{\mathbf{dl}}$ is the angle between the bilayer symmetry axis $\mathbf{d}$ with the external magnetic field $\mathbf{B_0}$. (C) Random distributions of liquid crystallites originate a Pake or powder pattern line shape which is a sum of the doublets from domains with different alignments. The horns in powder patterns correspond to the most probable angle of the director $\theta_{\mathbf{dl}} = 90^{\circ}$. (D) Small multi-lamellar vesicles give rise to broad multi-Lorentzian line shapes. As the number of shells increase, the spectra will become a superposition of line shapes from smaller vesicles with powder patterns from the shells with higher radius similarly to the case (E). Redrawn from reference [44] with permission.

At a site of a bilayer system with an alignment in respect to the magnetic field given by $\theta_{\mathbf{dl}}$ as described in Figure 2.4, a given ^{13}C–^{1}H spin pair in a lipid or surfactant molecule will give rise to the ^{13}C precession frequencies

$$\omega_{\mathrm{C}}^{\pm}(\theta_{\mathbf{dl}}) = \omega_{\mathrm{C}}^0 \pm \pi J_{\mathrm{CH}} + P_2(\cos\theta_{\mathbf{dl}})\left[\omega_{\mathrm{C}}^{\mathrm{aniso}}\langle P_2(\cos\theta_{\mathbf{pd}}^{\mathrm{C}})\rangle \pm d_{\mathrm{CH}}S_{\mathrm{CH}}\right], \quad (4.1)$$

where ω_{C}^0 is the isotropically shifted Larmor frequency, J_{CH} is the scalar coupling constant of the ^{13}C–^{1}H spin pair on the order of 100-200 Hz, $\omega_{\mathrm{C}}^{\mathrm{aniso}}$ is the maximum value possible for the chemical shift anisotropy (CSA) which depends on the orientation of the CSA principal axis frame in respect to the director $\mathbf{d}$ given by $\theta_{\mathbf{pd}}^{\mathrm{C}}$, S_{CH} is as defined in Equation 2.5, and $d_{\mathrm{CH}}/2\pi$ is the ^{13}C–^{1}H dipolar coupling which is approximately equal to -22 kHz (see Appendix for a thorough description of all the constants).

According to Equation 3.15, the ^{13}C NMR absorption spectrum will depend on the transition frequencies as

$$I(\omega) \propto \int P(\theta_{\mathbf{dl}}) \left\{ \frac{R_2}{R_2^2 + [\omega - \omega_C^+(\theta_{\mathbf{dl}})]^2} + \frac{R_2}{R_2^2 + [\omega - \omega_C^-(\theta_{\mathbf{dl}})]^2} \right\} d\theta_{\mathbf{dl}}, \quad (4.2)$$

where $P(\theta_{\mathbf{dl}})$ is the probability distribution of the distinct bilayer alignments in the macroscopic sample under study. Figure 4.1 illustrates how the possible microstructural arrangements in a macroscopic phase of liquid crystals would affect the ^{13}C NMR spectrum in terms of the dipolar coupling average only - neglecting the CSA interaction. The various pictures suggest that ^{13}C NMR spectrum is a potential source of structural information since distinct aggregate arrangements have characteristic line shapes and splittings.

In practice however, complications invariably arise that make the experimental measurement of such line shapes directly. The effect of the CSA contribution will distort the spectra most often asymmetrically. Additionally, when studying relatively large molecules, such as lipid or surfactant molecules, a number of peaks from magnetically inequivalent carbon sites will be distributed over the ^{13}C spectrum, separated by frequency intervals which are smaller than the dipolar splittings around 1-10 kHz, i.e. the spectrum will contain large overlaps between different carbons. Thus, although the dipolar line shapes contain precious structural details, the information is blurred out with a concomitant loss of the high spectral resolution that is e.g. attained in isotropic liquids. Fortunately, it is possible to emulate the spectral features of isotropic liquids by spinning the samples around a so-called magic angle spinning (MAS) axis and performing NMR experiments simultaneously [77].

4.1.1   Resolution enhancement

If during the NMR acquisition the sample is spun around an axis $\mathbf{r}$ that makes an angle $\theta_{\mathbf{rl}}$ with the direction of the main magnetic field, the alignment of the liquid crystal domains will change periodically over time and the factor $P_2(\cos \theta_{\mathbf{dl}})$ in Equation 4.1 will be on average [74]

$$\langle P_2(\cos \theta_{\mathbf{dl}}) \rangle = P_2(\cos \theta_{\mathbf{rl}}) P_2(\cos \theta_{\mathbf{dr}}), \quad (4.3)$$

where $\theta_{\mathbf{dr}}$ is the angle between the director $\mathbf{d}$ of the liquid crystal and the rotation axis $\mathbf{r}$. If the rotation frequency in cycles per second is much faster than $2d_{\text{CH}} S_{\text{CH}}$, the time average in Equation 4.3 can be included in the motional average approximation. For the so-called magic angle $\theta_{\mathbf{rl}} = \arccos(1/\sqrt{3})$ the ^{13}C transition frequencies become

$$\omega_C^\pm = \omega_C^0 \pm \pi J_{\text{CH}}, \quad (4.4)$$

which are the same as in an isotropic liquid.

Magic angle spinning greatly enhances the ^{13}C NMR spectral resolution, however, since samples are seldom composed of independent ^{13}C-^{1}H spin systems, in practice other contributions, namely the effect of ^{1}H homonuclear dipolar couplings with neighboring protons, render the MAS averaging less effective [74]. In order to increase resolution, the acquisition of a ^{13}C signal under MAS is usually accompanied by an additional averaging by means of RF pulse sequences in the ^{1}H channel referred to as heteronuclear decoupling sequences [78]. The performance of a given decoupling sequence usually depends on the MAS spinning rate used. In general, best performance means achieving narrower NMR peaks at the expense of the least RF power possible to avoid heating up samples. While performing heteronuclear decoupling, the J-coupling interaction is also averaged out, thus the ^{13}C transition frequencies $\omega_C^{\pm}$ become both equal to the isotropic chemical shift ω_C^0. All results presented in this thesis were obtained by signal acquisitions using the TPPM decoupling sequence [79] which is presently the most used decoupling sequence at moderate spinning rates.

4.1.2 Intensity enhancement

The simplest of all MAS NMR experiments to measure ^{13}C spectra is the so-called direct polarization (DP) method, by application of a single 90º hard pulse with subsequent detection of the ^{13}C signal with heteronuclear decoupling. The DP experiment can be used to determine quantitatively the composition of the sample under study, e.g. in multi-component systems, since the area of each distinct Lorentzian in the ^{13}C spectrum depends solely on the quantity of carbons involved. Except for this feature, because of the low gyromagnetic ratio γ_C of ^{13}C (about 1/4 of γ_H for protons), rather than using the raw magnetization of ^{13}C it is often more useful to transfer magnetization from protons to ^{13}C nuclei before signal acquisition. This procedure renders the amplitude of peaks non-quantitative.

The most commonly used polarization transfer pulse sequences in NMR are the INEPT (insensitive nuclei enhanced by polarization transfer) method [80, 81], usually applied to liquids, and the CP (cross polarization) transfer, widely used in solids [82]. While INEPT uses the *J*-coupling between nuclei to induce the magnetization transfer, CP uses direct dipole-dipole couplings. The pulse sequences of the DP, INEPT and CP sequences are shown in Figure 4.2 along with a basic description of their principles.

A. DP

B. INEPT (refocused)

C. CP

D. Intensity enhancement
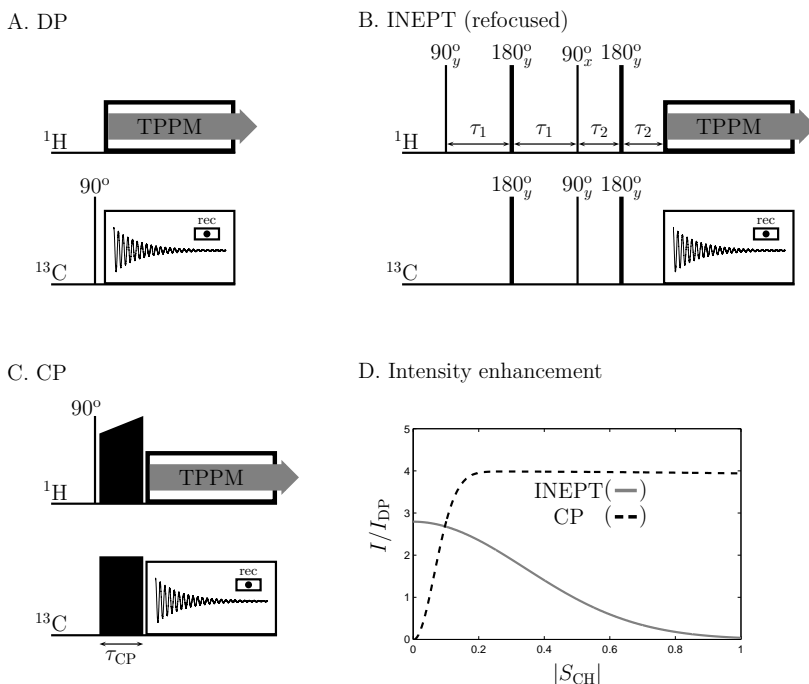
Figure 4.2: (A, B and C) NMR pulse sequences used for acquiring ^{13}C spectra from amphiphilic bilayer systems. All sequences use TPPM decoupling in the proton channel during ^{13}C signal acquisition. (A) Direct polarization - A single 90° pulse is used to flip the carbon magnetization to the transverse plane, followed by acquisition. (B)The proton magnetization is flipped to the transverse plane and evolves under J-coupling generating transverse proton magnetization coupled with ^{13}C longitudinal magnetization, these are then manipulated to refocus as ^{13}C transverse magnetization. (C) Cross polarization from a hot reservoir of magnetization (^{1}H) to a cold one (^{13}C). The spins are both subjected to a double rotating frame using long RF pulses at resonance with their Larmor frequencies. At the rotating frame the only effective magnetic fields are due to the RF pulses. Since the magnetic field exerted in the ^{13}C channel is 4 times higher than for protons, the effective energy levels of the ^{13}C and ^{1}H spins become equal at the rotating frame. Since the ^{13}C and ^{1}H upper energy levels are under- and over- populated, respectively, energy flows from ^{1}H to ^{13}C. A more rigorous description of INEPT and CP may be found in the textbooks of Levitt [71] and Duer [74], respectively. (D) Theoretical predictions for the CP and INEPT enhancement as in Nowacka et. al [83]

In respect to NMR spectroscopy, anisotropic liquid crystals lie somewhere between a solid and a liquid. Thus, choosing between INEPT and CP usually depends on the system under study. The ^{13}C signal enhancement of an INEPT sequence relatively to a DP experiment can be approximately written as [83]

$$\frac{I_{\text{INEPT}}}{I_{\text{DP}}} = \frac{\sqrt{2}}{4}\frac{\gamma_{\text{H}}}{\gamma_{\text{C}}} \exp\left(-\frac{R_2^{\text{H}}}{4J_{\text{CH}}} - \frac{R_2^{\text{C}}}{8J_{\text{CH}}}\right), \tag{4.5}$$

using the optimized time delays $\tau_1 = J_{\text{CH}}^{-1}/4$ and $\tau_2 = J_{\text{CH}}^{-1}/8$. The relaxation rate constants R_2^{H} and R_2^{C} relate to structure by S_{CH} as described in the next Chapter. The buildup of the CP transfer is frequently approximated as [83]

$$\frac{I_{\text{CP}}}{I_{\text{DP}}} = \frac{\gamma_{\text{H}}}{\gamma_{\text{C}}}\frac{\exp(-R_{1\rho}^{\text{H}}\tau_{\text{CP}}) - \exp(-R_{\text{CH}}\tau_{\text{CP}})}{1 - R_{1\rho}^{\text{H}}/R_{\text{CH}}}, \tag{4.6}$$

where τ_{CP} is the contact time as shown in Figure 4.2C and $R_{1\rho}^{\text{H}}$ and R_{CH} are also relaxation rates again dependent on S_{CH} and dynamical properties.

Figure 4.2D illustrates how the ^{13}C intensity enhancements of INEPT and CP are affected by S_{CH} according to a theoretical model in reference [83]. The general trend of the dependency shown is observed in the experimental spectra of lipid bilayers as illustrated in Figure 4.3 through a collection of ^{13}C INEPT, CP and DP peaks from cholesterol.

Lamellar liquid crystals with fluid lamellar phases composed of phospholipids and cholesterol contain both CH bonds with low S_{CH} magnitudes around 0-0.2 and CH bonds with higher S_{CH} magnitudes around 0.2-0.4. For instance, the restricted intramolecular motions of CH bonds in the cholesterol ring and its
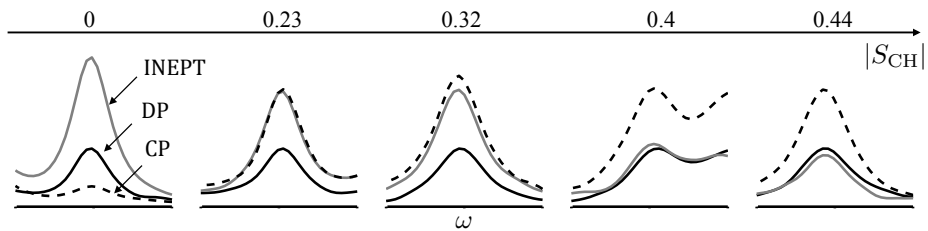
Figure 4.3: A collection of cholesterol ^{13}C peaks ordered by their order parameter magnitudes. The spectrum was measured from POPC/cholesterol MLVs at full hydration, using a MAS rate of 5 kHz and the DP (black), INEPT (gray) and CP (dashed) sequences. Note the CP buildup and the decrease of INEPT intensity with the increase of $|S_{\text{CH}}|$.

overall orientation, with its long axis pointed perpendicular to the bilayer plane, impose order parameters of around 0.4 to a number of C–H bonds. Therefore, CP performs considerably better than INEPT in order to measure ^{13}C signals from the cholesterol ring structure. With respect to the ^{13}C signals from phospholipids the choice is two-fold. In the absence of cholesterol, INEPT generally performs better. With the inclusion of cholesterol, there is a strong buildup of CP signal from carbons of the phospholipids because of the ordering of acyl chains. Thus, when performing studies which require the measurement of ^{13}C signals from lipid MLVs containing cholesterol it is recommendable to combine both INEPT and CP experiments.

4.2 Dipolar recoupling NMR

The spectral resolution of anisotropic liquid crystals is achieved with MAS at the expense of the precious information contained in the CSA and dipolar couplings. Since the anisotropic interactions have such a well defined orientation dependence, they could be used for structural investigations. Indeed, several methods for bringing back the anisotropic interactions under MAS have been reported [84].

A successful method to measure these interactions is by performing 2D NMR. The idea is to introduce a recoupling step in the pulse sequence, prior to acquisition, which modulates the amplitude of the signals measured according to the anisotropic interaction recoupled. If a collection of acquisitions at different recoupling times (the indirect dimension) is recorded, it is possible to obtain a 2D spectrum which contains the isotropic chemical shift site specificity in one dimension, and the structural information in the second dimension [85]. The procedure is usually called Separate Local Field (SLF) since effectively the spin states evolve under the local field of the interaction recoupled during the indirect dimension time step, while during acquisition they evolve under the field due to the Zeeman interaction and the isotropic interactions only.

In this thesis, a type of SLF spectroscopy, denoted R-type Proton Detected Local Field (R-PDLF) spectroscopy, was used to measure ^{13}C–^{1}H dipolar couplings. These couplings are of great interest for structural studies of bilayers since they are linearly proportional to the order parameter S_{CH}. The R-PDLF pulse sequence scheme can be seen in Figure 4.4. A heteronuclear recoupling symmetry block R18$_1^7$ is used to reactive the dipolar coupling between protons and ^{13}C nucleus. It has been shown that the R18$_1^7$ block yields clear modulation frequencies for IS spin systems but less well defined modulations in I_2S and I_3S groups. In the first SLF methods using the R18$_1^7$ recoupling sequence, reported by Zhao et al. [86], the dipolar field was recoupled in order to directly induce a modulation of ^{13}C transverse magnetization which was then recorded at different recoupling time lengths t_1.
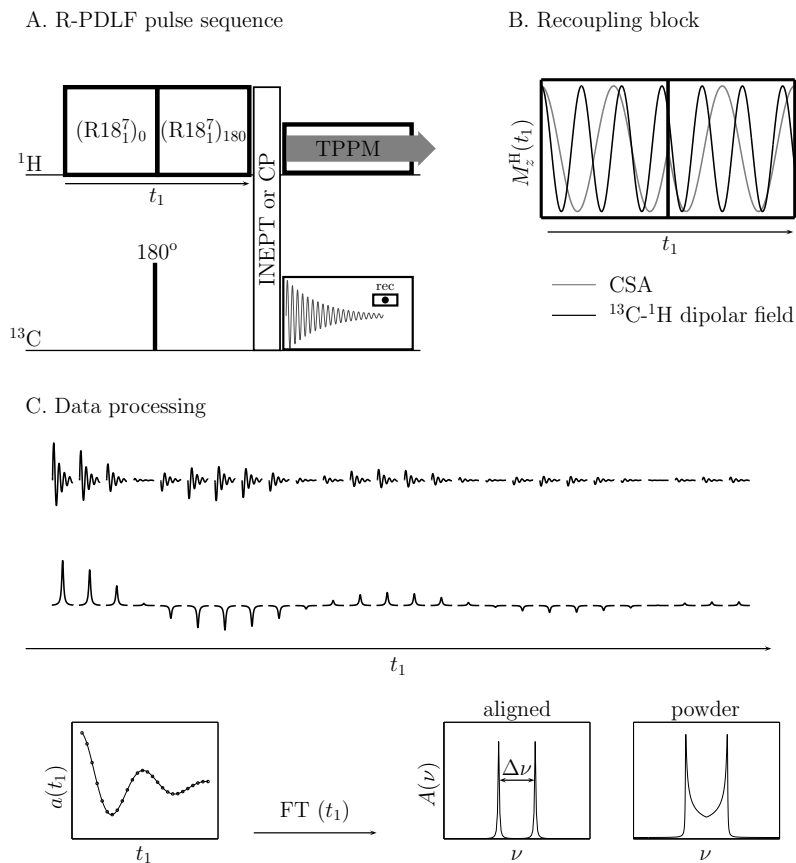
Figure 4.4: (A) During each $R18_1^7$ block in indirect dimension t_1 the proton CSA and the dipolar field from ^{13}C are reactivated inducing a modulation of the proton longitudinal magnetization. The phase shift of the recoupling block mirrors the evolution for both the CSA and dipolar coupling but if a 180° pulse is applied in the ^{13}C channel only the effect of the CSA is refocused at the end of the second recoupling block as illustrated in (B). (C) The data is processed by 2D Fourier transform yielding a NMR spectrum with splittings proportional to S_{CH}. Samples with liquid crystallites aligned at a single angle with the magnetic field give rise to doublets, while samples composed of randomly oriented crystallites give rise to a powder pattern.

Rather than using this approach, the R-PDLF scheme [87] uses the $R18_1^7$ blocks to modulate the proton magnetization through the reactivation of the dipolar field from the dilute ^{13}C nuclei, and then transfers the proton magnetization to ^{13}C i.e. modulates the acquired ^{13}C signals also but by means of the proton magnetization.

The advantage of R-PDLF over the previous method is both due to resolution and specificity enhancements. In terms of resolution, if the ^{13}C transverse magnetization is modulated by the proton local fields directly, there are contributions from a large network of protons, each with a characteristic dipolar coupling. On the other hand, the proton magnetization under $R18_1^7$ recoupling of protons is only modulated by the dipolar field of ^{13}C since just 1.1% of carbon sites are ^{13}C isotopes. In addition to this, it is known that the $R18_1^7$ recoupling is not effective to induce clear modulations of I_2S or I_3S spin systems [88]; R-PDLF circumvents this problem also since the proton magnetization under recoupling evolves on a IS spin system basis, thus conferring the resolution of the two distinct C–H bond couplings in a CH_2 group.

Selectivity in R-PDLF is readily achieved by choosing an INEPT transfer, since only the magnetization of the covalently bonded protons is transferred. However, for C-H bonds with higher order parameters, the INEPT sequence may require a high number of transients which makes the CP transfer more suitable. Using CP is done at the expense of selectivity though, since also the non-covalently bonded protons participate in the polarization transfer. When using R-PDLF with a CP transfer it is thus recommendable to use short contact times in order to remove the contributions from the more distant protons. In Papers **I**,**II** and **III**, a number of bilayers systems have been studied by means of R-PDLF spectroscopy and complete profiles for S_{CH} magnitudes have been determined. One example of an experimental R-PDLF spectrum is shown in Figure 4.5.

A. 1D ^{13}C MAS NMR spectra

INEPT

CP

$\delta(^{13}$C / ppm)

B. Section of a R-PDLF spectra

$\delta(^{13}$C) / ppm

^{13}C–^{1}H dipolar field / kHz

C. Cross sections of B.

$\Delta\nu$

^{13}C–^{1}H dipolar field / kHz
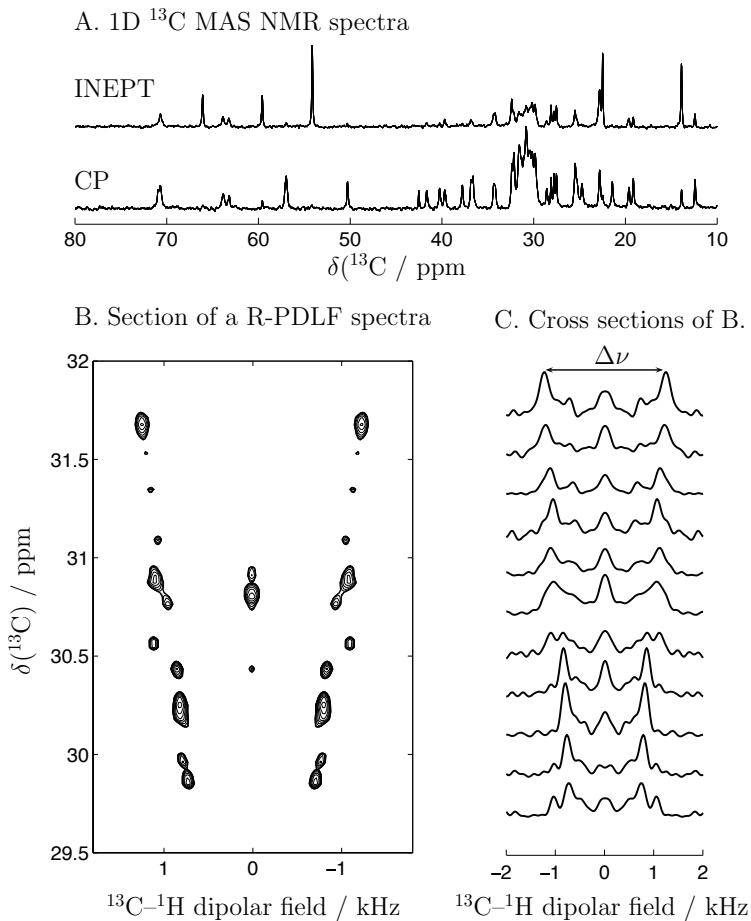
Figure 4.5: Sections of a CP R-PDLF spectrum obtained from a sample of liquid crystals with POPC/cholesterol bilayers (50:50 mol%) at a hydration of 40 wt%. (A) INEPT and CP 1D ^{13}C spectrum showing POPC and cholesterol peaks. Peak assignments are given in Paper **I**. (B) CP R-PDLF spectrum section at the crowded spectral region. (C) Cross-sections of the spectrum in (B) showing dipolar recoupling line shapes at different ^{13}C chemical shift frequencies. The size of the splittings, $\Delta\nu$, at the different chemical shifts is proportional to S_{CH} by $\Delta\nu = \frac{0.315}{2\pi} d_{\mathrm{CH}} S_{\mathrm{CH}}$.

^{13}C NMR RELAXATION

In addition to structural information, NMR spectroscopy may also be used to determine observables related with the time scale of various motions [23, 54, 89]. The free induction decay itself relates to molecular motion by the constant R_2 (Equation 3.11), as well as the intensities of INEPT and CP experiments by other relaxation constants. Such relaxation rates always depend on some form of rearrangement of the nuclear spin magnetic moments towards a thermal equilibrium state similarly to what as been shown in Figure 3.3.

Establishing a theoretical framework to analyze Relaxation NMR phenomena is more complicated than to analyze solely structural parameters from spectral features, since the secular and motional approximations cannot be used. Instead, non-secular terms of the several Hamiltonian interactions need also to be taken into account, and solving Equation 3.6 is more intricate due to the use of a time-dependent Hamiltonian. A proper description of how one may tackle this problem in various ways can be found in the textbooks of Kowalewski and Mäler [75], and Abragam [90].

Within the scope of this thesis, it suffices to introduce the ^{13}C relaxation rates studied and to describe their dependence on the reorientation motions of C–H bonds. It is assumed that the ^{13}C NMR relaxation in all systems depends exclusively on the C–H dipolar coupling. Relaxation effects due to couplings between electrons and nuclei are not considered since they are seldom important when treating ^{13}C–^{1}H spin pairs [75]. It is also assumed that the motion of the C–H bonds studied is axially symmetric.

5.1 Dipolar relaxation of ^{13}C magnetization

The relaxation of ^{13}C magnetization towards a thermal equilibrium state is generated by local fluctuating magnetic fields acting on the ^{13}C nuclear sites [73]. For ^{13}C nuclei in CH, CH$_2$ and CH$_3$ groups, the local fields are originated by the magnetic moments of the covalent protons. Therefore the fluctuations originate mostly due to C–H bond rotational diffusion as illustrated in Figure 5.1. The relaxation of the longitudinal magnetization, M_z (Equation 3.10), is caused by the fluctuations of the transverse components of the local fields, which induce variations in the polar angles of the ^{13}C magnetic moments. Relaxation of the net magnetization in the transverse plane, is caused by both fluctuations of the z-components and transverse components of the local fields. The time taken for magnetization to relax to equilibrium depends on the rates of the local field fluctuations and therefore on the time scales for C–H bond reorientation.
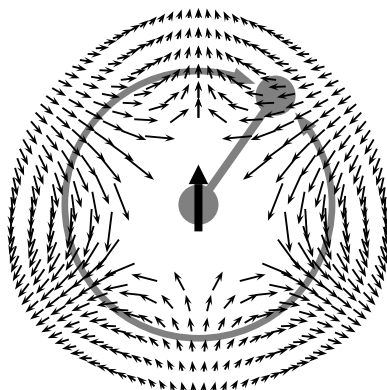
Figure 5.1: A cross section of the symmetric magnetic field induced by the magnetic dipole of a proton (center) to a ^{13}C nuclear site. The dependence with distance was scaled for clarity of the field lines, although in reality it should decay more steeply [75]. Rotational diffusion of the C–H bond induces a fluctuating magnetic field on the ^{13}C nuclei.

5.2 Relaxation rates

The fluctuation of the transverse magnetic field in a carbon site due to the rotational diffusion of the C–H chemical bond can be analyzed by means of the

auto-correlation function [76]

$$g(t) = \langle P_2[\boldsymbol{\eta}(\tau)\boldsymbol{\eta}(\tau + t)]\rangle, \tag{5.1}$$

with $\boldsymbol{\eta}(\tau)$ as the unitary vector with the direction of the chemical bond axis at time τ, and where the average is taken over an infinite number of time instants. The Fourier transform of $g(t)$, denoted the spectral density $J(\omega)$, and can be expressed as

$$J(\omega) = 2 \int_0^\infty \cos(\omega t)g(t)dt. \tag{5.2}$$

NMR relaxation rates are, in general, expressed as linear combinations of spectral density terms $J(\omega_i)$, at frequencies ω_i which depend on the involved relaxation mechanisms [75, 76]. The coefficients for the linear combinations are derived from appropriate quantum theoretical treatments [75, 90]. The most typical ^{13}C NMR relaxation rates measured are the following [76].

- The spin-lattice relaxation rate R_1, defining the time scale of ^{13}C longitudinal magnetization equilibration, and usually expressed as

$$R_1 = \frac{d_{CH}^2 N_H}{20}\left[J(\omega_H - \omega_C) + 3J(\omega_C) + 6J(\omega_C + \omega_H)\right], \tag{5.3}$$

  in which ω_C and ω_H are the Larmor angular frequencies of ^{13}C and ^1H respectively, N_H is the number of bound protons, and the dipolar coupling constant is given by

$$d_{CH} = -\frac{\mu_0 \hbar \gamma_H \gamma_C}{4\pi\langle r_{CH}^3\rangle},$$

  where μ_0 is the magnetic constant or vacuum permeability, $\hbar$ is the reduced Planck constant, γ_C and γ_H are the gyromagnetic constants of ^{13}C and ^1H respectively, and $\langle r_{CH}^3\rangle$ is the average cubic distance of the C–H chemical bond. $d_{CH}/2\pi$ is approximately equal to -22 kHz for a methylene C–H bond [15, 91].

- The spin-spin relaxation rate R_2, defining the equilibration of ^{13}C transverse magnetization on the absence of pulses and normally approximated as

$$R_2 = \frac{d_{CH}^2 N_H}{40}\left[4J(0) + J(\omega_H - \omega_C)\right.$$

$$\left. + 3J(\omega_C) + 6J(\omega_H) + 6J(\omega_C + \omega_H)\right], \tag{5.4}$$

  where ω_H, ω_C, N_H and d_{CH} are as described above.

- The spin-lattice relaxation rate at the rotating frame $R_{1\rho}$, defining the equilibration of ^{13}C transverse magnetization under a spin lock pulse and expressed as

$$R_{1\rho}(\omega_1) = \frac{d_{\text{CH}}^2 N_{\text{H}}}{40}\left[4J(\omega_1) + J(\omega_{\text{H}} - \omega_{\text{C}})\right.$$
$$\left. + 3J(\omega_{\text{C}}) + 6J(\omega_{\text{H}}) + 6J(\omega_{\text{C}} + \omega_{\text{H}})\right], \quad (5.5)$$

where ω_1 is the nutation frequency used during the spin lock pulse, and where ω_{H}, ω_{C} and d_{CH} are as in Equation 5.3.

5.3 Auto-correlation function

The interpretation of above relaxation rates is usually complicated and normally depends on the choice of a guess auto-correlation function $g(t)$. If the motion of the C–H bond were to be completely isotropic at every possible time-scale, $g(t)$ could be expressed as an exponential decay [75]

$$g(t) = e^{-t/\tau_{\text{c}}} \quad (5.6)$$

described by a single correlation time τ_{c}. In practice, for most molecules whether with isotropic or anisotropic tumbling, this form of auto-correlation function for C–H bond reorientation seldom occurs. It may happen for special cases in which molecules are rigid and highly symmetric but not in general.

Assuming a two-step model [68, 92, 93] the auto-correlation function of molecules within bilayers, can be expressed in terms of two independent regimes, one representing the fast rotational anisotropic diffusion of molecules and another describing the slower isotropic motions. Within this framework, one may express $g(t)$ as

$$g(t) = (1 - S_{\mathbf{cn}}^2)g_{\text{f}}(t) + S_{\mathbf{cn}}^2 g_{\text{s}}(t), \quad (5.7)$$

where $S_{\mathbf{cn}}$ is the order parameter introduced in Equation 2.5, $g_{\text{f}}(t)$ describes the anisotropic fast motions of the C–H bond within a time scale during which the angle between the local bilayer normal $\mathbf{n}$ and the external magnetic field is constant, and $g_{\text{s}}(t)$ is a correlation function that represents the rotation of the C–H bond at long time scales due to flip-flops and diffusion along the interfacial surface with the subsequent averaging of the bilayer normal vector in respect to the magnetic field. At the limits $t \to 0$ and $t \to \infty$, $g_{\text{f}}(0)$ and $g_{\text{s}}(0)$ are equal to 1 and $g_{\text{f}}(\infty)$ and $g_{\text{s}}(\infty)$ are equal to 0. According to Equation 2.5, for systems with $S_{\mathbf{nd}} = 1$, Equation 5.7 can also be written as

$$g(t) = (1 - S_{\text{CH}}^2)g_{\text{f}}(t) + S_{\text{CH}}^2 g_{\text{s}}(t), \quad (5.8)$$

since S_{CH} is equal to $S_{\mathbf{cn}}$.

5.4   Spectral density

If the two step model assumption in Equation 5.7 is valid, whenever the time-scales of $g_f(t)$ and $g_s(t)$ are completely separable, the spectral density $J(\omega)$ shows an approximately constant value at frequencies ω_1 around 10-100 kHz (Paper **IV** for the explicit proof). From the properties of Fourier transforms, it can be shown that such plateau value is equal to the integral

$$J(\omega_1) = 2(1 - S_{CH}^2) \int_0^\infty g_f(t)dt \qquad (5.9)$$

which only depends on the area of $g_f(t)$, irrespectively of its shape, and on the order parameter S_{CH}. The auto-correlation function $g_f(t)$ describes all the fast motions occurring at time scales within a time length for complete averaging of S_{CH} equal or below 100 ns. Assuming that $g_f(t)$ can be expressed as a distribution of exponential functions [94], it may be written as

$$g_f(t) = \int_{\tau_f} P(\tau_f)e^{-\frac{t}{\tau_f}} d\tau_f, \qquad (5.10)$$

where $P(\tau_f)$ denotes a distribution of correlation times τ_f. The total area of $g_f(t)$ is equal to the average of the correlation times used in the multi-exponential description

$$\tau_e = \int_{\tau_f} P(\tau_f)\tau_f d\tau_f \qquad (5.11)$$

and is referred to as the effective correlation time τ_e [94]. By using the multi-exponential description in Equation 5.9, one obtains the simple expression

$$J(\omega_1) = 2(1 - S_{CH}^2)\tau_e. \qquad (5.12)$$

The determination of τ_e would enable to access a well defined quantity from the reorientation of a C–H bond, which is easily interpreted e.g. by its visual inspection as illustrated in Figure 5.2. The relaxation rates alone are more difficult to interpret since they have a more intricate dependence on the C–H bond reorientation motions (see e.g. the discussion about the interpretation of R_1 and τ_e given in paper Paper **IV**). In the next section, a method is described for the purpose of measuring τ_e values from the distinct C–H bonds of amphiphilic molecules within a fluid bilayer, and an example of a practical application is given for studying the effect of cholesterol on the molecular dynamics of a phospholipid bilayer. Note that, as shown in section 2.3.2, τ_e is a quantity accessible by means of all-atom MD simulations of bilayers. Thus, it may be used for validating the time-scales of motions predicted in such simulations.
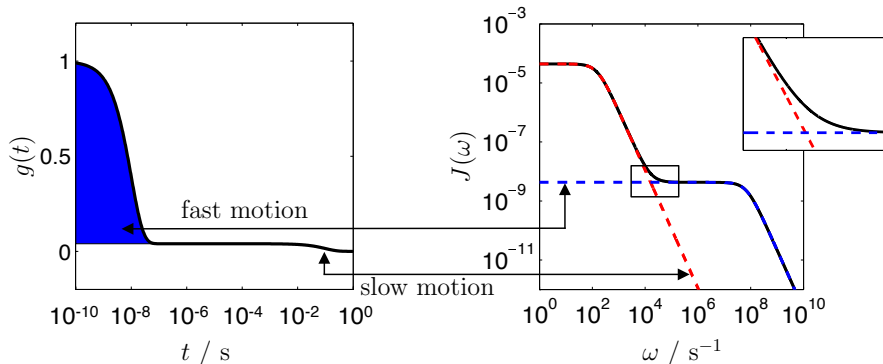
Figure 5.2: Schematic diagram for the concept of C–H bond effective correlation time τ_e in a bilayer system. (Left) Simulacrum of an auto-correlation function $g(t)$ for C–H bond reorientation in a bilayer system, assuming two separable time scales of reorientation motion, a fast anisotropic motion and a slower isotropic motion. The effective correlation time τ_e corresponds to the area in blue scaled by $(1 - S_{CH}^2)^{-1}$. (Right) The Fourier transform of $g(t)$, normally referred to as the spectral density $J(\omega)$, is a sum of contributions from the fast and slow motions. At very low (1-1000 Hz) and very high frequencies (> 50 kHz), $J(\omega)$ depends solely on the slow and fast motions, respectively. At the intermediate range, as shown in the inset, $J(\omega)$ depends on both contributions. The value of $J(\omega)$ at around 50-100 kHz is approximately equal to twice the area in blue in $g(t)$.

5.5 Measurement of the effective correlation time

According to Equation 5.5, the spin-lattice relaxation rate at the rotating frame $R_{1\rho}$ depends on $J(\omega)$, at the frequency used for the spin-lock of the magnetization, usually around 20-100 kHz, and at frequencies around 10^9 Hz with respect to the currently used magnetic field strengths in NMR experiments. Thus for ω_1 frequencies at which $J(\omega_1)$ is approximately equal to the plateau value as shown in Figure 5.2, $R_{1\rho}$ depends solely on the fast correlation function $g_f(t)$ and on the order parameter S_{CH}.

The spin-lattice relaxation rate R_1 also depends exclusively on fast motions, albeit through only the fastest motions described in $g_f(t)$ with time scales on the order of 10^{-9} s or lower. ^{13}C relaxation rates can be measured by various techniques [75]. The ^{13}C R_1 and $R_{1\rho}$ values obtained in this thesis were measured by acquiring 2D data sets using the methodology described in Figure 5.3.
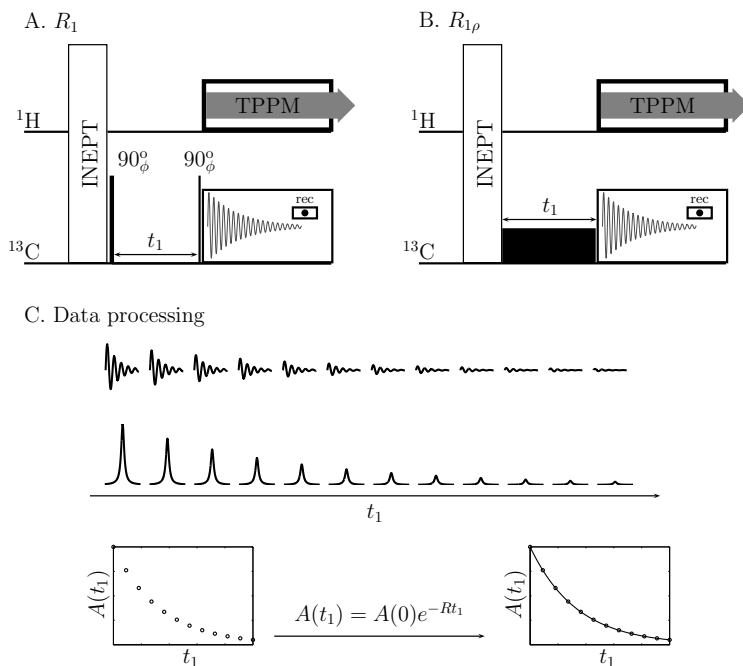
Figure 5.3: (A and B) Pulse sequences used to measure the relaxation rate constants R_1 and $R_{1\rho}$ from amphiphilic bilayers. (A) 13C magnetization R_1 relaxation during the indirect dimension t_1 after INEPT enhancement of the ^{13}C transverse magnetization. A phase cycling scheme for the obtaining the R_1 decay was used as suggested by Torchia [95]. (B) Spin lock of the ^{13}C INEPT enhanced transverse magnetization during t_1. (C) Data processing for both A and B. The FID signals acquired through the indirect dimension are first subjected to Fourer transform in order to yield pure absorption Lorentzian peaks. The amplitude of the peaks in then fitted by a single exponential decay from which the relaxation rate is determined.

As shown in Paper **IV** the R_1 and $R_{1\rho}$ relaxation rates can be combined to determine τ_e within a reasonable approximation as

$$\tau_e \approx \frac{5R_{1\rho} - 3.375R_1}{d_{CH}^2 N_H (1 - S_{CH}^2)}, \tag{5.13}$$

with the requirement that the magnetic field strength used for measuring R_1 and $R_{1\rho}$ is the same, and that the spin lock nutation frequency ω_1 used to obtain $R_{1\rho}$ is around 50-100 kHz.

As discussed in the previous chapter, to achieve proper spectral resolution from anisotropic liquid crystalline samples, it is necessary to spin the samples.

This has also an effect on the spectral density as illustrated in Figure 5.4 and described in Paper **IV**. Since the MAS rates used are usually around 5-10 kHz this effect is not important in the use of Equation 5.13, assuring the requirements described previously.
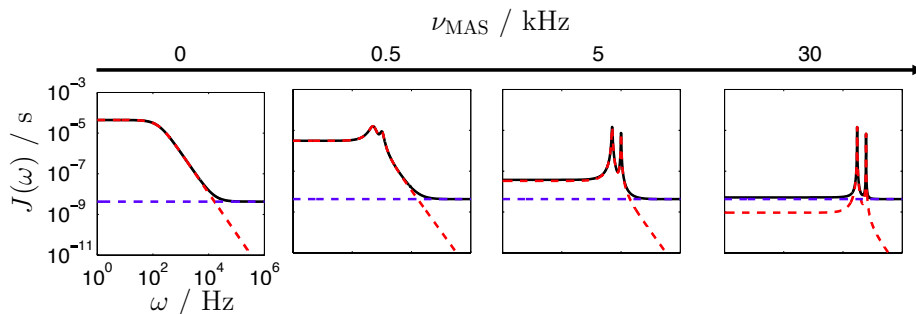
Figure 5.4: The effect of magic angle spinning of the sample on the spectral density $J(\omega)$. Two sharp peaks appear at frequencies corresponding to the spinning rate and to twice of the spinning rate, and $J(0)$ is shifted towards lower values. In the currently used NMR magnets, the most common NMR relaxation rates depend on $J(\omega)$ at particular frequencies in the range(s): 10^9 Hz (R_1), $10^3 - 10^4$ and 10^9 Hz ($R_{1\rho}$), and at 0 and 10^9 Hz (R_2).

5.5.1 Application to POPC/cholesterol bilayers

The use of Equation 5.13 is exemplified in Figure 5.5.1, showing the effect of cholesterol on the C–H reorientation dynamics of the glycerol backbone and choline headgroup of POPC molecules in a lipid bilayer. The origin of the *condensing effect* introduced in section 2.4.2, is not yet very well understood [96]. Different suggestions for the origin of the strong phospholipid-cholesterol interaction have been given, such as: being caused by van der Waals forces between the cholesterol ring and the phospholipid alkyl/acyl chains [97]; by hydrogen bonding of the OH group of cholesterol with the polar part of the phospholipids [98]; or due to the possible existence of a so-called *umbrella effect* [99]. The latter concept is based on the hypothesis of cholesterol being shielded against water by means of the head groups of phospholipids, and often the term reorientation of the head groups is used to describe the effect. The results in Figure 5.5, together with Paper **I**, strongly suggest that cholesterol does not induce a reorientation of the choline headgroup, nor by means of a structural change, nor by a biased rotation of the choline of any kind. Cholesterol does induce a dramatic slow down on the dynamics of the glycerol backbone. This suggests that the rotational diffusion of the choline group is not coupled to the rotational diffusion of the glycerol backbone.
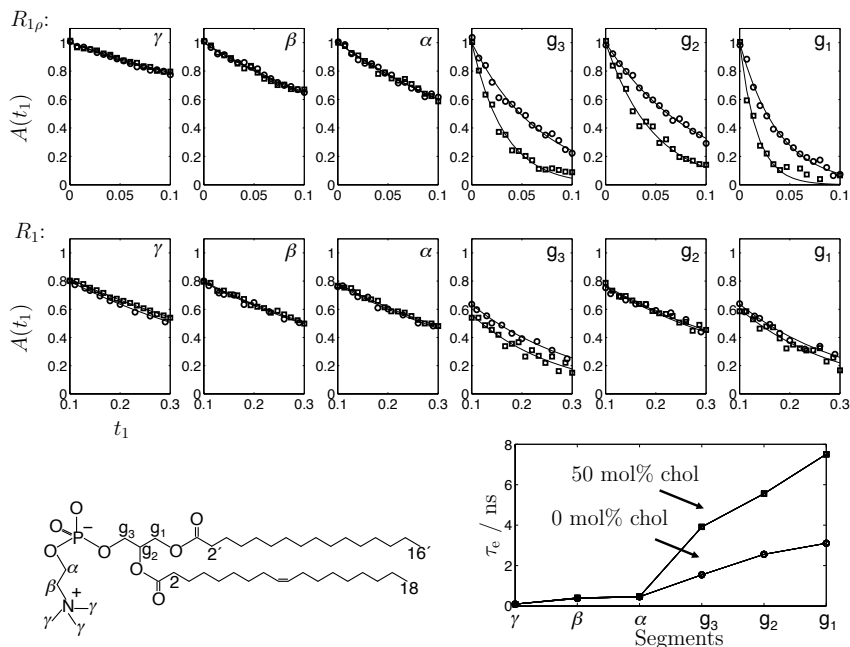
Figure 5.5: Application of the protocol described in Paper **IV** for determining τ_e, to elucidate the effect of cholesterol on the C–H bond rotational diffusion occurring in the polar region of a POPC fluid bilayer. The samples used are composed of ($\circ$) bilayers of POPC, and ($\square$) bilayers with POPC and cholesterol at 50:50 mol%. (Top) R_1 and $R_{1\rho}$ decays from the different segments in the polar part of POPC, labeled as in the chemical structure shown at the lower left corner. By performing the data processing scheme described in Figure 5.3 to determine R_1 and $R_{1\rho}$, and the procedure described in the previous Chapter to determine S_{CH}, one may estimate the effective correlation time by Equation 5.13 for both samples. The profile of τ_e values determined is shown at the lower left corner using units of ns. With the inclusion of cholesterol in the bilayer, the dynamics of C–H bond reorientation are significantly slower in the glycerol backbone, albeit the rotational diffusion motion of the choline seems to be completely unaffected.

MD SIMULATIONS OF BILAYER SYSTEMS

Molecular dynamics (MD) simulation methods enable to predict atomic trajectories in lipid bilayers by using deterministic mathematical models [18]. The application of these methods enhances the interpretation of experiments since, if an experimental observable is predicted by the simulations, other quantities may be also inferred upon from the atomic trajectories. Reciprocally, experimental observables are indispensable to validate force-fields and MD simulation algorithms. With respect to NMR observables, MD simulations of bilayers have been validated by comparisons of S_{CH} order parameters [16] and relaxation times R_1 [16, 100], and have been used to test models for translating NMR observables into other quantities e.g. molecular areas or projection lengths [53, 101]. This chapter presents a brief description of the MD models used in this thesis, and introduces a new procedure for testing the C–H bond reorientation dynamics predicted in MD simulations of amphiphilic bilayers by means of $R_{1\rho}$ relaxation rates.

6.1 Force-fields and MD Algorithms

A MD simulation of a lipid bilayer consists on implementing a given force-field [102–105] describing the interactions between and within molecules in the bilayer, i.e. the potential energy surface, into an MD algorithm [106] that integrates the differential equations of Newton, enabling to record the trajectories of particles from an initial state throughout the course of time.

Since the computational resources are limited, simulating a macroscopic system of bilayers is not possible. Instead, the system is reduced to a simulation

box - with presently a few hundreds of lipid or surfactant molecules and a few thousands of water molecules - and periodic boundary conditions are used, i.e. the outside of the box is represented by replications of the original box through a periodic arrangement. Thus, the amphiphilic bilayer systems simulated are always perfect liquid crystals with a single symmetry director axis.

Several MD software packages are nowadays available; the most popular for lipid bilayer simulations have been GROMACS [20] and NAMD [21], and they may implement a number of available lipid force-fields [105]. In general, the force-fields used comprise a number of parameters that define two major types of interactions between atoms: bonded and non-bonded interactions. Atoms that are bonded are usually treated like spheres connected by springs: Covalent bonds and bending angles are described by harmonic potentials with an associated spring constant and equilibrium distance (or angle) length [107]; Torsional angles are described by Ryckart-Bellemans potentials [108]. The interactions of non-bonded atoms are normally described by electrostatic potentials according to their defined point charges, and as Lennard-Jones spheres [20]. Also tabulated user-defined potentials may be used which are then computed by interpolation procedures.

6.2   Limitations

In order to use MD simulations to interpret lipid bilayer phenomena it is important to know at which degree the trajectories obtained represent the real systems. Excellent reviews on this topic may be found in a number of publications [102–104]. Here, only a few relevant aspects are discussed.

It may be argued that the major limitation is the use of a classical description of atoms rather than of a proper use of a modern quantum description. An accurate quantum mechanical description of a lipid bilayer is at present not possible - due to the number of atoms involved and the limited computer resources presently available - which is the main reason to use the deterministic models instead. Neglecting quantum effects imposes from the start the exclusion of any possible description of chemical reactions that may occur in membranes.

Although the evolution in time during the course of a MD simulation is classical, the potential energy parameters are calculated by using *ab initio* quantum chemistry methods [104]. In practice, the calculation of force-field parameters is never accomplished from first principles only. Invariably, the force-field parameters are determined so that a specific experimental quantity is predicted e.g. molecular density; a proper validation should then be determined by its ability to predict other quantities than the used for parametrization. One force-field limitation that has been under discussion, is the use of spheres with point charges neglecting polarizability effects and the common force-field description given in the preceding section may in this respect change in the future [109].

Another restriction is the time length of the simulation. This depends on both hardware and software and new methods based on optimizing both of these two aspects are presently under development [110, 111]. Since many observables of interest are time averages, it is important to achieve trajectories which are long enough such that convergent averages are calculated. The time length required for a given trajectory will depend on the mechanism under study. For instance, for a reasonable calculation of the C–H bond reorientation correlation function introduced in section 2.3.2, a time length of between 100 ns and 1 μs is needed. Lateral diffusion processes require longer times since the diffusion of a lipid molecule is very slow on the order of $1\mu\text{m}^2/\text{s}$ [54].

The size of the simulation box also matters, i.e. the number of molecules used to describe the system. In this case, a converged average is reached when the quantity calculated does not vary by increasing the size of the system further. For instance, the nonionic surfactant bilayer structures presented in this thesis (section 2.5.1 and Paper **III**) had to be extended to 500 surfactant molecules to achieve equilibrium due to the size of the pores formed. Otherwise, in smaller systems the pores stretch over periodic boundary conditions and an artifact infinite pore size is obtained. Another example is that phospholipid bilayer systems may phase separate laterally, as discussed in section 2.4.2. In such cases the simulation box should be large enough for achieving the size of the separated domains and thus thermodynamic equilibrium.

6.3 Force-field validation by NMR

NMR spectroscopy has been one the main sources of accurate experimental data to validate MD simulations of amphiphilic bilayers both in respect to structural [16, 24, 100, 104, 105, 112] and dynamical [16, 23, 24, 55] features.

6.3.1 C–H bond order parameters

In terms of structure, since the early stage of all-atom simulations of bilayers, whenever an atomic trajectory of a system is reported, usually a detailed comparison of experimental and simulated order parameters S_{CH} as defined in Equation 2.5 is included [16]. Experimental NMR schemes to determine S_{CH} values usually involved complicated deuteration procedures which made the range of systems studied limited [12]. At the present state-of-the art of NMR, as described in section 4.2, it is possible to acquire complete S_{CH} profiles from nearly every distinct bond in simple lipid bilayers without recursion to isotopically modified compounds, e.g. in two component bilayers of phospholipid and cholesterol as shown in Paper **I**. Such new NMR methods will probably be of extreme importance in the near future for force-field optimization since they can virtually apply to all the relevant model systems.

6.3.2   C–H bond reorientation dynamics

Validation of rotational diffusion processes has been done exclusively by comparison with spin-lattice relaxation rates R_1 from different nuclei e.g. ^{2}H, ^{31}P, ^{15}N and ^{13}C at a range of magnetic field strengths [16, 23, 55, 113–118]. ^{13}C R_1 values may be calculated by equation 5.3. The other nuclei have relaxation rates with similar expressions. The comparison of R_1 rates probes the validity of rotational diffusion occurring at short time scales around 0.1 to 10 ns. Such comparisons may originate spurious interpretations. The agreement between experiments and simulations using a set of R_1 values measured at a single magnetic field strength do not necessarily validate a MD model since e.g. motions with differences of about 1 order of magnitude may have the same R_1 value at a given magnetic field strength (see for instance Paper **IV**). A comparison of R_1 values measured at various magnetic field strengths is more appropriate [23, 55, 113]. This presents a technical problem since most NMR laboratories have only a few number of magnets, each with a characteristic magnetic field strength, and thus just a few R_1 studies performed at various field strengths have been published until date [16].

The ^{13}C R_1 values are determined by using the MD simulated trajectories (which at present may extend to 100 ns or even time scales around 1μs) to calculate auto-correlation functions $g(t)$ as defined in Equation 2.6, and by using then Equations 5.2 and 5.3 to calculate $J(\omega)$ and R_1. Distinct numerical methods can be used to find $J(\omega)$. A possible procedure is by fitting $g(t)$ with a discrete version of the multi-exponential decay function in Equation 5.10 as

$$g(t) = (1 - S^2)g_{\mathrm{f}}(t) + S_{\mathrm{CH}}^2 \tag{6.1}$$

and obtaining $J(\omega)$ from the analytical Fourier transform of the multi-exponential function

$$J(\omega) = 2(1 - S_{\mathrm{CH}}^2) \sum_{i=1}^{N} \alpha_i \frac{\tau_i}{1 + \omega^2 \tau_i^2}, \tag{6.2}$$

assuming ω values higher than 1 MHz, and where α_i are the coefficients found by performing a multi-exponential fit using N different correlation times τ_i.

Since R_1 depends on $J(\omega)$ at frequencies near the precession rates of spins i.e. around 50-1000 MHz in the most common NMR spectrometer systems used nowadays, and since there are characteristic motions of lipid bilayers occurring at time-scales around ns, the contributions of slower motions with correlation times above ns will not contribute to R_1 values. Thus, the comparison of the R_1 values predicted by MD simulations with experimental values, is sensitive to the faster motions or, in other words, to the shape of $g(t)$ determined by the time length of a few ns of simulation.
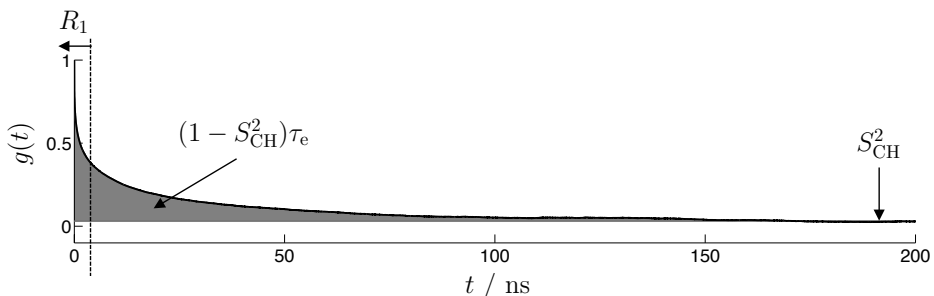
Figure 6.1: Auto-correlation function $g(t)$ for C–H bond reorientation as calculated from a MD simulation of a POPC bilayer. The C–H bond used for the calculation shown was from the g_1 segment in the glycerol backbone of POPC which is the segment with slowest dynamics. The figure depicts the time intervals of $g(t)$ that determine R_1 relaxation rates, around 1 to 10 ns, and τ_e values (or similarly $R_{1\rho}$) around 200 ns. Comparison of the predicted τ_e values in such MD model with experimental values (details in Paper **IV**) indicate that the model underestimates the C–H bond dynamics in the polar and interfacial regions of the phospholipid bilayer e.g. of the shown carbon, but reproduces reasonably well the dynamics in the hydrophobic liquid core. In this case, the comparison of ^{13}C R_1 values calculated for $\omega_C = 125$ MHz, is misleading since e.g. a perfect match for the C–H bond shown is predicted while τ_e is around 4 times slower.

As the time length of the simulation increases other motional processes are described within larger time windows of 10-1000 ns which determine $g(t)$ before it reaches the plateau value equal to S_{CH}^2 as shown in Figure 6.1. Contrarily to R_1, τ_e is independent of the shape of $g(t)$ and depends on the full time interval from 0 to 1000 ns. Therefore, the calculation of τ_e in addition to R_1, and the subsequent comparison with experimental values, measured by the method described in Paper **IV**, enables a more trustworthy validation than from using R_1 values alone.

The calculation of τ_e from $g(t)$ is trivial. For C–H bond trajectories that are long enough, i.e. if $g(t)$ decays to the plateau S_{CH}^2, one may calculate τ_e by numerical integration of the area in gray shown in Figure 6.1. For cases in which $g(t)$ does not reach the plateau completely, an approximation for τ_e may be obtained by fitting a multi-exponential decay to $g(t)$, as described above, and by calculating the average correlation time used in the fit as in Equation 5.11.

Note that a comparison of τ_e is similar to a comparison of $R_{1\rho}$ obtained by

the expression (Equation 19 in Paper **IV**)

$$R_{1\rho}^{\mathrm{plateau}} = \frac{d_{\mathrm{CH}}^2 N_{\mathrm{H}}}{10} \left[2(1-S_{\mathrm{CH}}^2)\tau_{\mathrm{e}} + J(\omega_{\mathrm{H}}-\omega_{\mathrm{C}}) + 3J(\omega_{\mathrm{C}}) + 6J(\omega_{\mathrm{H}}) + 6J(\omega_{\mathrm{C}}+\omega_{\mathrm{H}}) \right].$$
(6.3)

Therefore, if the separation of time scales in Equation 5.8 is valid, additionally to R_1 rates, also $R_{1\rho}$ values can be calculated from MD simulations. In fact, for the purpose of testing MD simulations, the comparison between NMR experiments and MD simulations by means of $R_{1\rho}$ rates is more accurate than a comparison of τ_{e} values, since it does not involve the approximation used to obtain Equation 5.13.

CONCLUDING REMARKS

NMR spectroscopy and MD simulations are two well established methods to obtain molecular scale information from a broad range of materials. The work here presented concerns the application of these methods to the study of molecular structure and dynamics in amphiphilic bilayer systems. The main conclusions of the research conducted are here summarized:

- **Molecular structure**

  Dipolar recoupling NMR spectroscopy is a valuable means to determine C–H bond order parameters in amphiphilic bilayers. Using INEPT and CP polarization transfer methods in a R-PDLF pulse sequence allows to measure complete or nearly complete C–H bond order parameter profiles from single- and two-component bilayers. The profiles are useful to validate structural predictions from MD simulations and to interpret structural bilayer properties.

- **Molecular dynamics**

  The correlation time function for C–H bond reorientation in lipid bilayers can be efficiently described by a two-step model from which the fast component can be fully calculated from MD simulations. This enables to derive an experimental procedure for determining effective correlation times in lipid bilayers, and allows to calculate $R_{1\rho}$ rates from MD simulations, additionally to R_1, that are directly comparable with NMR experiments.

- **Bilayer structure**

  The two types of amphiphilic bilayers studied have rather different order parameter profiles in their hydrophobic tails, ranging from 0-0.2 to 0-0.4 in various POPC/cholesterol bilayers, and within 0-0.1 in the nonionic surfactant bilayers. This suggests that while the POPC/cholesterol bilayers are, at the nm scale, flat extended films impenetrable by water, the bilayers of $C_{12}E_5$ surfactants have a high density of aqueous pores.

- **Phosphatydilcholine/cholesterol bilayers**

  POPC bilayers show C–H bond effective correlation times from 0.1 ns to 3 ns with the glycerol backbone and acyl chain carbons close to the hydrophilic/hydrophobic interface having much slower dynamics comparatively to the dynamics of C–H bonds located in the choline chain or in the remaining acyl chain segments. The structure of acyl chains in phosphatidylcholine bilayers is strongly disturbed by the inclusion of cholesterol. The structure of the polar groups are rather unaffected, albeit the dynamics of the glycerol backbone becomes considerably slower. The dynamics of C–H bond reorientation in the choline chain are not affected.

- **C_mE_n bilayers**

  Poly(ethyleneoxide)-based surfactants generally form bilayers with overall order parameter magnitudes below 0.1. In connection to the MD simulations presented here, this indicates that in general the lamellar phase region of these systems is porous. The exquisite temperature dependence of CH order parameter profiles of poly(ethyleneoxide)surfactant bilayers reflects the contraction of alkyl chains and extension of PEO chains induced by a temperature increase.

CONTRIBUTIONS TO THE PAPERS

I **Cholesterol and POPC segmental order parameters in lipid membranes: solid state ^{1}H–^{13}C NMR and MD simulation studies**
I performed the NMR experiments and MD simulations, processed and analyzed the data, and wrote the article.

II **Segmental order parameters in a nonionic surfactant lamellar phase studied with ^{1}H–^{13}C solid-state NMR**
I performed the NMR experiments, processed and analyzed the experimental data, and wrote the article.

III **Molecular conformation and bilayer pores in a nonionic surfactant lamellar phase studied with ^{1}H–^{13}C solid-state NMR and MD simulations**
I performed the NMR experiments, processed and analyzed the experimental data, and also took part in writing the manuscript.

IV **Model-free estimation of the effective correlation time for C–H bond reorientation in amphiphilic bilayers: ^{1}H–^{13}C solid-state NMR and MD simulations**
I derived the method together with Topgaard and Ollila, performed the NMR experiments, processed and analyzed the NMR data, and wrote the manuscript.

Appendix

Secular and motional average approximation of the ^{13}C frequencies

The interactions of an individual ^{13}C-^{1}H spin pair in a molecule under a strong and homogeneous magnetic field $\mathbf{B_0}$ may be described by the spin Hamiltonian

$$\hat{H} = \hat{H}_\text{Z} + \hat{H}_\text{CS} + \hat{H}_\text{D} + \hat{H}_\text{J}, \tag{1}$$

where the Zeeman term (Z) represents interactions between the two nuclear spins and the main external field $\mathbf{B_0}$, the chemical shift term (CS) denotes the interaction of the two nuclei with their electronic surroundings, and the remaining terms describe the spin interactions between the two nuclei, one by a dipolar coupling through space (D), plus a weaker coupling by means of the electrons in the C–H chemical bond denoted scalar coupling (J).

The Zeeman Hamiltonian, describes the coupling between each spin and a main external field of magnitude B_0 as [71]

$$\hat{H}_\text{Z} = -B_0(\gamma_\text{H}\hat{I}_z - \gamma_\text{C}\hat{S}_z), \tag{1a}$$

whith γ_H and γ_C being the gyromagnetic ratios of the ^{1}H and ^{13}C nuclei, and where $\hat{I}_z$ and $\hat{S}_z$ are the z components of the ^{1}H and ^{13}C spin angular momenta in a laboratory frame with a z axis pointing in the same direction of $\mathbf{B_0}$. The products $\gamma_\text{H}B_0$ and $\gamma_\text{C}B_0$ are the Larmor frequencies of the ^{1}H and ^{13}C nuclei respectively and correspond to the frequencies of precession of ^{1}H and ^{13}C isolated spins.

Since the Zeeman interaction is much stronger than any of the other nuclear spin couplings, the spin state of a ^{13}C-^{1}H spin pair is usually represented as a linear combination of ket products: $|\alpha\rangle^\text{H}|\alpha\rangle^\text{C}$, $|\alpha\rangle^\text{H}|\beta\rangle^\text{C}$, $|\beta\rangle^\text{H}|\alpha\rangle^\text{C}$ and $|\beta\rangle^\text{H}|\beta\rangle^\text{C}$; which are products between the individual Zeeman eigenstates of the ^{1}H and ^{13}C spins. Any spin state $|\psi\rangle$ of a ^{13}C-^{1}H spin pair can thus be expressed as [74]

$$|\psi\rangle = c_{\alpha\alpha}|\alpha\alpha\rangle + c_{\alpha\beta}|\alpha\beta\rangle + c_{\beta\alpha}|\beta\alpha\rangle + c_{\beta\beta}|\beta\beta\rangle,$$

where the coefficients c_{ij} are complex numbers and $|\alpha\alpha\rangle = |\alpha\rangle^{\mathrm{H}}|\alpha\rangle^{\mathrm{C}}$, $|\alpha\beta\rangle = |\alpha\rangle^{\mathrm{H}}|\beta\rangle^{\mathrm{C}}$ and so on. Within this basis, the other interactions are then expressed as a first order perturbation to the main Zeeman Hamiltonian. Such procedure is referred to as the secular approximation and the resulting Hamiltonian expressions as secular Hamiltonians.

In addition, also a motional average approximation can be used in the case of liquids because of the fast tumbling motions of molecules [71]. Within such approximation, the geometrical dependence of each secular Hamiltonian term is accounted as an average factor rather than as an explicit function of time. This removes the time dependence in the Hamiltonian, which greatly simplifies the NMR theoretical framework, and enables to find relations between the NMR observables and the structural parameters of the systems under study.

The application of the secular and motional average approximations yields the following Hamiltonian forms for a molecule in a liquid sample:

- The chemical shift Hamiltonian

$$\hat{H}_{\mathrm{CS}} = -\gamma_{\mathrm{H}}\delta_{\mathrm{H}}B_0\hat{I}_z - \gamma_{\mathrm{C}}\delta_{\mathrm{C}}B_0\hat{S}_z, \tag{1b}$$

where each of the chemical shift parameters δ_{H} and δ_{C} may be split as

$$\delta = \delta^{\mathrm{iso}} + \delta^{\mathrm{aniso}}\langle P_2(\cos\theta_{\mathbf{pl}})\rangle, \tag{2}$$

using one parameter independent of molecular orientation δ^{iso}, and a second term which contains the molecular orientation dependence through the time averaged second Legendre polynomial $\langle P_2(\cos\theta_{\mathbf{pl}})\rangle$, in which $\theta_{\mathbf{pl}}$ is the angle that the principal symmetry axis of the chemical shift interaction makes with the z axis of the laboratory frame. Like for the Zeeman hamiltonian, the strength of the chemical shift hamiltonian depends on the magnitude of the applied magnetic field $\mathbf{B_0}$.

- The scalar or J- coupling Hamiltonian

$$\hat{H}_{\mathrm{J}} = -2\pi J_{\mathrm{CH}}\hat{I}_z\hat{S}_z, \tag{1c}$$

where J_{CH} is the isotropic component of the J-coupling tensor. The anisotropic component of the J-coupling tensor is not considered here since its very small and usually neglected.

- The heteronuclear dipolar Hamiltonian

$$\hat{H}_{\mathrm{D}} = 2d_{\mathrm{CH}}\langle P_2(\cos\theta_{\mathbf{cl}})\rangle\hat{I}_z\hat{S}_z, \tag{1d}$$

which depends on the possible angles $\theta_{\mathbf{cl}}$ formed by the C–H chemical bond axis and the z axis of the laboratory frame, and where the dipolar coupling constant is defined as

$$d_{\mathrm{CH}} = -\frac{\mu_0\hbar\gamma_{\mathrm{H}}\gamma_{\mathrm{C}}}{4\pi\langle r_{\mathrm{CH}}^3\rangle}$$

where μ_0 is the vacuum permeability, $\hbar$ is the reduced Planck constant, and $\langle r_{\mathrm{CH}}^3 \rangle$ is the average cubic distance between ^{13}C and ^{1}H.

By substituting all of these secular Hamiltonians in Equation 1, and after some rearrangements, the obtained time-independent Hamiltonian may be expressed as

$$\hat{H}^0 = \hat{H}_{\mathrm{iso}}^0 + \hat{H}_{\mathrm{aniso}}^0, \tag{3}$$

where the first term represents a secular Hamiltonian independent of orientation

$$\hat{H}_{\mathrm{iso}}^0 = \omega_{\mathrm{H}}^0 \hat{I}_z + \omega_{\mathrm{C}}^0 \hat{S}_z - 2\pi J_{\mathrm{CH}} \hat{I}_z \hat{S}_z,$$

which contains the isotropic chemically shifted Larmor frequencies of the ^{1}H and ^{13}C spins $\omega_{\mathrm{H,C}}^0 = -\gamma_{\mathrm{H,C}} B_0 (1 + \delta_{\mathrm{H,C}}^{\mathrm{iso}})$ and the J-coupling interaction, and the second term representing the orientational dependent contributions

$$\hat{H}_{\mathrm{aniso}}^0 = \omega_{\mathrm{H}}^{\mathrm{CSA}} \langle P_2(\cos\theta_{\mathbf{pl}}^{\mathrm{H}})\rangle \hat{I}_z + \omega_{\mathrm{C}}^{\mathrm{CSA}} \langle P_2(\cos\theta_{\mathbf{pl}}^{\mathrm{C}})\rangle \hat{S}_z + 2 d_{\mathrm{CH}} \langle P_2(\cos\theta_{\mathbf{cl}})\rangle \hat{I}_z \hat{S}_z,$$

with $\omega_{\mathrm{H,C}}^{\mathrm{CSA}} = -\gamma_{\mathrm{C}} B_0 \delta_{\mathrm{H,C}}^{\mathrm{aniso}}$ denoting the maximum chemical shift anisotropies of the ^{1}H and ^{13}C spins.

Within the secular and motional approximations, the allowed ^{13}C nuclear spin transition frequencies in a liquid sample are

$$\omega_{\mathrm{C}}^{\pm} = \omega_{\mathrm{C}}^0 + \omega_{\mathrm{C}}^{\mathrm{CSA}} \langle P_2(\cos\theta_{\mathbf{pl}}^{\mathrm{C}})\rangle \pm \left[d_{\mathrm{CH}} \langle P_2(\cos\theta_{\mathbf{cl}})\rangle + \pi J_{\mathrm{CH}} \right], \tag{4}$$

where ω_{C}^+ and ω_{C}^- are the frequencies of the transitions $|\alpha\rangle^{\mathrm{H}}|\alpha\rangle^{\mathrm{C}} \leftrightarrow |\alpha\rangle^{\mathrm{H}}|\beta\rangle^{\mathrm{C}}$ and $|\beta\rangle^{\mathrm{H}}|\alpha\rangle^{\mathrm{C}} \leftrightarrow |\beta\rangle^{\mathrm{H}}|\beta\rangle^{\mathrm{C}}$ respectively.

For a a given site in a bilayer with an orientation described by $\theta_{\mathbf{dl}}$ as described in Figure 2.4, the following trigonometric relations can be used:

$$\langle P_2(\cos\theta_{\mathbf{pl}})\rangle = P_2(\cos\theta_{\mathbf{dl}})\langle P_2(\cos\theta_{\mathbf{pd}})\rangle, \tag{5}$$

$$\langle P_2(\cos\theta_{\mathbf{cl}})\rangle = P_2(\cos\theta_{\mathbf{dl}}) S_{\mathrm{CH}}, \tag{6}$$

with $\theta_{\mathbf{pd}}$ as the angle between the chemical shift principal symmetry axis $\mathbf{p}$ and symmetry axis $\mathbf{d}$, and where $S_{\mathrm{CH}} = \langle P_2(\cos\theta_{\mathbf{cd}})\rangle$ appears, which is the order parameter in Equation 2.5 and Figure 2.4. The ^{13}C precession frequencies can thus be written as

$$\omega_{\mathrm{C}}^{\pm}(\theta_{\mathbf{dl}}) = \omega_{\mathrm{C}}^0 \pm \pi J_{\mathrm{CH}} + P_2(\cos\theta_{\mathbf{dl}}) \left[\omega_{\mathrm{C}}^{\mathrm{aniso}} \langle P_2(\cos\theta_{\mathbf{pd}}^{\mathrm{C}})\rangle \pm d_{\mathrm{CH}} S_{\mathrm{CH}} \right], \tag{7}$$

REFERENCES

1. H. Wennerström and D. F. Evans. *The Colloidal Domain. Where Physics, Chemistry, Biology and Technology Meet.* Wiley-VCH (1999).

2. K. Holmberg, B. Jönsson, B. Kronberg and B. Lindman. *Surfactants and Polymers in Aqueous Solution.* John Wiley & Sons Ltd (2003).

3. A. P. M. Lockwood. *The Membranes of Animal Cells.* The Camelot Press Ltd London (1971).

4. D. Marsh. *Handbook of Lipid Bilayers.* CRC Press (1990).

5. O. S. Andersen and R. E. Koeppe. *Bilayer thickness and membrane protein function: An energetic perspective.* Annu. Rev. Biophys. Biomolec. Struct. **36**, 107–130 (2007).

6. M. F. Brown. *Curvature Forces in Membrane Lipid-Protein Interactions.* Biochemistry **51**, 9782–9795 (2012).

7. M. F. Brown and G. D. Williams. *Membrane NMR - A dynamic research area.* J. Biochem. Biophys. Methods **11**, 71–81 (1985).

8. K. Gawrisch, N. V. Eldho and I. V. Polozov. *Novel {NMR} tools to study structure and dynamics of biomembranes.* Chemistry and Physics of Lipids **116**, 135 – 151 (2002).

9. G. Lindblom and G. Orädd. *Lipid lateral diffusion and membrane heterogeneity.* Biochimica et Biophysica Acta (BBA) - Biomembranes **1788**, 234 – 244 (2009).

10. A. Grélard, C. Loudet, A. Diller and E. J. Dufourc. *NMR Spectroscopy of Lipid Bilayers.* In *Membrane Protein Structure Determination* volume 654 of *Methods in Molecular Biology* pages 341–359. Humana Press (2010).

11. J. Seelig. *Deuterium Magnetic Resonance - Theory and Application to Lipid Membranes.* Q. Rev. Biophys. **10**, 353–418 (1977).

12. J. H. Davis. *The description of membrane lipid conformation, order and dynamics by ^2H NMR.* Biochim. Biophys. Acta **737**, 117–171 (1983).

13. J. Seelig and W. Niederberger. *Deuterium-labeled lipids as structural probes in liquid crystalline bilayers. Deuterium magnetic resonance study.* J. Am. Chem. Soc. **96**, 2069–2072 (1974).

14. J. D. Gross, D. E. Warchawski and R. G. Griffin. *Dipolar Recoupling in MAS NMR: A Probe for Segmental Order in Lipid Bilayers.* J. Am. Chem. Soc. **119**, 796 (1997).

15. S. V. Dvinskikh, V. Castro and D. Sandström. *Efficient solid-state NMR methods for measuring heteronuclear dipolar couplings in unoriented lipid membrane systems.* Phys. Chem. Chem. Phys. **7**, 607 (2005).

16. A. Leftin and M. F. Brown. *An NMR database for simulations of membrane dynamics.* Biochim. Biophys. Acta-Biomembr. **1808**, 818–839 (2011).

17. R. B. Corey and L. Pauling. *Molecular models of amino acids, peptides, and proteins.* Rev. Sci. Instrum. **24**, 621–627 (1953).

18. J. M. Haile. *Molecular Dynamics Simulation: Elementary Methods.* John Wiley & Sons, Inc. New York (1992).

19. W. L. Ash, M. R. Zlomislic, E. O. Oloo and D. P. Tieleman. *Computer simulations of membrane proteins.* Biochim. Biophys. Acta-Biomembr. **1666**, 158–189 (2004).

20. E. Lindahl, B. Hess and D. van der Spoel. *GROMACS 3.0: a package for molecular simulation and trajectory analysis.* J. Mol. Model. **7**, 306–317 (2001).

21. J. C. Phillips, R. Braun, W. Wang, J. Gumbart, E. Tajkhorshid, E. Villa, C. Chipot, R. D. Skeel, L. Kalé and K. Schulten. *Scalable molecular dynamics with NAMD.* Journal of Computational Chemistry **26**, 1781–1802 (2005).

22. A. J. Gordon. *A survey of atomic and molecular models.* Journal of Chemical Education **47**, 30 (1970).

23. E. Lindahl and O. Edholm. *Molecular dynamics simulation of NMR relaxation rates and slow dynamics in lipid bilayers.* J. Chem. Phys. **115**, 4938–4950 (2001).

24. J. B. Klauda, R. M. Venable, J. A. Freites, J. W. O'Connor, D. J. Tobias, C. Mondragon-Ramirez, I. Vorobyov, A. D. MacKerell, Jr. and R. W. Pastor. *Update of the CHARMM All-Atom Additive Force Field for Lipids: Validation on Six Lipid Types.* J. Phys. Chem. B **114**, 7830–7843 (2010).

25. C. Tanford. *The Hydrophobic Effect: Formation of Micelles and Biological Membranes.* John Wiley & Sons (1980).

26. J. Israelachvili. *Intermolecular & Surface Forces.* Academic Press (1991).

27. J. N. Israelachvili, D. J. Mitchell and B. W. Ninham. *Theory of self-assembly of hydrocarbon mmphiphiles into micelles and bilayers.* Journal of the Chemical Society-Faraday Transactions II **72**, 1525–1568 (1976).

28. P. Morell and R. H. Quarles. *Characteristic Composition of Myelin.* Lippincott-Raven (1999).

29. K. Sumikawa, Z. S. Mu, T. Inoue, T. Okochi, T. Yoshida and K. Adachi. *Changes in erythrocide membrane phospholipid composition induced by physical training and physical exercise.* Eur. J. Appl. Physiol. Occup. Physiol. **67**, 132–137 (1993).

30. E. Zinser, C. D. M. Sperkagottlieb, E. V. Fasch, S. D. Kohlwein, F. Paultaf and G. Daum. *Phospholipid synthesis and lipid composition of subcellular membranes in the unicellular eukaryote saccharomyces cerevisiae .* J. Bacteriol. **173**, 2026–2034 (1991).

31. P. L. Yeagle. *Cholesterol and the Cell Membrane.* Biochimica Et Biophysica Acta **822**, 267–287 (1985).

32. A. Finkelstein and A. Cass. *Effect of cholesterol on water permeability of thin lipid membranes.* Nature **216**, 717–& (1967).

33. J. C. Mathai, S. Tristram-Nagle, J. F. Nagle and M. L. Zeidel. *Structural Determinants of Water Permeability through the Lipid Membrane.* The Journal of General Physiology **131**, 69–76 (2008).

34. A. G. Lee. *How lipids affect the activities of integral membrane proteins.* Biochim. Biophys. Acta-Biomembr. **1666**, 62–87 (2004).

35. K Simons and E Ikonen. *Functional rafts in cell membranes.* Nature **387**, 569–572 (1997).

36. B. A. Hills. *An alternative view of the role(s) of surfactant and the alveolar model.* J. Appl. Physiol. **87**, 1567–1583 (1999).

37. N. Salem, B. Litman, H. Y. Kim and K. Gawrisch. *Mechanisms of action of docosahexaenoic acid in the nervous system.* Lipids **36**, 945–959 (2001).

38. J. A. Barry and K. Gawrisch. *Direct NMR evidence for ethanol binding to the lipid-water interface of phospholipid bilayers.* Biochemistry **33**, 8082–8088 (1994).

39. D. Huster, K. Arnold and K. Gawrisch. *Influence of docosahexaenoic acid and cholesterol on lateral lipid organization in phospholipid mixtures.* Biochemistry **37**, 17299–17308 (1998).

40. K Simons and W L C Vaz. *Model systems, lipid rafts, and cell membranes.* Annu. Rev. Biophys. Biomolec. Struct. **33**, 269–295 (2004).

41. M. A. Kol, A. N. C. van Laak, D. T. S. Rijkers, J. A. Killian, A. I. P. M. de Kroon and B. de Kruijff. *Phospholipid Flop Induced by Transmembrane Peptides in Model Membranes Is Modulated by Lipid Composition.* Biochemistry **42**, 231–237 (2003).

42. F. X. Contreras, S. Lissete, A. Alicia and F. M. Goñi. *Transbilayer (flip-flop) lipid motion and lipid scrambling in membranes.* FEBS Letters **584**, 1779 – 1786 (2010).

43. M. C. Wiener and S. H. White. *Structure of a fluid dioleoylphosphatidyl-choline bilayer determined by joint refinement of X-ray and neutron-diffraction data. 3. Complete structure.* Biophys. J. **61**, 434–447 (1992).

44. T. M. Ferreira, D. Bernin and D. Topgaard. *NMR Studies of Nonionic Surfactants.* Annual Reports on NMR Spectroscopy **79**, 73–127 (2013).

45. A. K. Kenworthy. *Fluorescence Recovery After Photobleaching Studies of Lipid Rafts.* In TJ McIntosh, editor, *Methods in Molecular Biology* volume 398 of *Methods in Molecular Biology* pages 179–192. Humana Press (2007).

46. D. Marsh. *Electron spin resonance in membrane research: protein-lipid interactions from challenging beginnings to state of the art.* Eur. Biophys. J. Biophys. Lett. **39**, 513–525 (2010).

47. N. Kucerka, M. Nieh and J. Katsaras. *Fluid phase lipid areas and bilayer thicknesses of commonly used phosphatidylcholines as a function of temperature.* Biochim. Biophys. Acta-Biomembr. **1808**, 2761–2771 (2011).

48. D. Capitani, A. Yethiraj and E. E. Burnell. *Memory effects across surfactant mesophases.* Langmuir **23**, 3036–3048 (2007).

49. J.M. Seddon and R.H. Templer. *Chapter 3 Polymorphism of lipid-water systems.* In R. Lipowsky and E. Sackmann, editors, *Structure and Dynamics of Membranes* volume 1 of *Handbook of Biological Physics* pages 97 – 160. North-Holland (1995).

50. G. Arvidson, I. Brentel, A. Khan, G. Lindblom and K. Fontell. *Phase equilibria in four lysophosphatidylcholine/water systems.* European Journal of Biochemistry **152**, 753–759 (1985).

51. O. Cruciani, L. Mannina, A. P. Sobolev, C. Cametti and A. Segre. *An Improved NMR Study of Liposomes Using 1-Palmitoyl-2-oleoyl-sn-glycero-3-phospatidylcholine as Model.* Molecules **11**, 334–344 (2006).

52. J. Valério, M. H. Lameiro, S. S. Funari, M. J. Moreno and E. Melo. *Temperature Effect on the Bilayer Stacking in Multilamellar Lipid Vesicles.* The Journal of Physical Chemistry B **116**, 168–178 (2012).

53. H. I. Petrache, S. W. Dodd and M. F. Brown. *Area per lipid and acyl length distributions in fluid phosphatidylcholines determined by H-2 NMR spectroscopy.* Biophys. J. **79**, 3172–3192 (2000).

54. A. Filippov, G. Oradd and G. Lindblom. *The effect of cholesterol on the lateral diffusion of phospholipids in oriented bilayers.* Biophys. J. **84**, 3079–3086 (2003).

55. J. B. Klauda, N. V. Eldho, K. Gawrisch, B. R. Brooks and R. W. Pastor. *Collective and Noncollective Models of NMR Relaxation in Lipid Vesicles and Multilayers.* J. Phys. Chem. B. **112**, 5924 (2008).

56. J. H. Ipsen, G. Karlström, O. G. Mouritsen, H. Wennerström and M. J. Zuckermann. *Phase-equilibria in the phosphatydil-cholesterol system.* Biochim. Biophys. Acta **905**, 162–172 (1987).

57. M. R. Vist and J. H. Davis. *Phase equilibria of cholesterol dipalmitoylphosphatidylcholine mixtures – ^2H nuclear magnetic resonance and differential scanning calorimetry.* Biochemistry **29**, 451–464 (1990).

58. S. L. Veatch, I. V. Polozov, K. Gawrisch and S. L. Keller. *Liquid domains in vesicles investigated by NMR and fluorescence microscopy.* Biophys. J. **86**, 2910–2922 (2004).

59. R. Dong and J. Hao. *Complex Fluids of Poly(oxyethylene) Monoalkyl Ether Nonionic Surfactants.* Chem. Rev. **110**, 4978–5022 (2010).

60. B. Lindman, O. Söderman and H. Wennerström. *Nuclear Magnetic Resonance as a Tool for Surfactant Systems.* Ann. Chim. **77**, 1–48 (1987).

61. D. J. Mitchell, G. J. T. Tiddy, L. Waring, T. Bostock and M. P. McDonald. *Phase-Behavior of Polyoxyethylene Surfactants with Water - Mesophase Structures and Partial Miscibility (Cloud Points).* J. Chem. Soc. Faraday Trans. **79**, 975–1000 (1983).

62. B. Lindman and G. Karlström. *Nonionic polymers and surfactants: Temperature anomalies revisited.* C. R. Chim. **12**, 121–128 (2009).

63. S. Saeki, N. Kuwahara, M. Nakata and M. Kaneko. *Upper and lower critical solution temperatures in poly (ethylene glycol) solutions.* Polymer **17**, 685 – 689 (1976).

64. M. Andersson and G. Karlström. *Conformational Structure of 1,2-Dimethoxyethane in Water and Other Dipolar Solvents, Studied by Quantum Mechanical, Reaction Field, and Statistical Mechanical Techniques.* J. Phys. Chem. **89**, 4957 (1985).

65. G. Karlström. *A New Model for Upper and Lower Critical Solution Temperatures in Poly(Ethylene oxide) Solutions.* J. Phys. Chem. **89**, 4962 (1985).

66. C. E. Fairhurst, M. C. Holmes and M. S. Leaver. *Structure and Morphology of the Intermediate Phase Region in the Nonionic Surfactant $C_{16}EO_6$/Water System.* Langmuir **13**, 4964 (1997).

67. M. Baciu, U. Olsson, M. S. Leaver and M. C. Holmes. ^2H *NMR evidence for the formation of random mesh phases in nonionic surfactant-water systems.* J. Phys. Chem. B **110**, 8184 (2006).

68. T. Ahlnäs, G. Karlström and B. Lindman. *Dynamics and Order of Nonionic Surfactants in Neat Liquid and Micellar Solution from Multifield ^{13}C NMR Relaxation and ^{13}C NMR Chemical Shifts.* J. Phys. Chem. **91**, 4030 (1987).

69. M. C. Holmes. *Intermediate phases of surfactant-water mixtures.* Curr. Opin. Colloid Interface Sci. **3**, 485–492 (1998).

70. G. Klose and Y. K. Levine. *Membranes of Palmitoyloleoylphosphatidylcholine and $C_{12}E_4$. A Lattice Model Simulation.* Langmuir **16**, 671–676 (2000).

71. M. H. Levitt. *Spin Dynamics.* John Wiley & Sons Ltd (2008).

72. J. J. Sakurai and Napolitano J. *Modern Quantum Mechanics.* Pearson (2011).

73. J. Keeler. *Understanding NMR Spectroscopy.* Wiley (2005).

74. M. J. Duer. *Introduction to Solid-State NMR Spectroscopy.* Blackwell (2004).

75. J. Kowalewski and L. M'aler. *Nuclear Spin Relaxation in Liquids: Theory, Experiments, and Applications.* Taylor & Francis (2006).

76. R. K. Harris. *Nuclear Magnetic Resonance Spectroscopy*. Longman Scientific & Technical (1986).

77. J. C. Hennel and Klinowski J. *Magic-Angle Spinning: a Historical Perspective*. Topics in Current Chemistry **246**, 1–14 (2005).

78. S. Paul, N. D. Kurur and P. K. Madhu. *On the choice of heteronuclear dipolar decoupling scheme in solid-state NMR*. J. Magn. Reson. **207**, 140–148 (2010).

79. A. E. Bennett, C. M. Rienstra, M. Auger, K. V. Lakshmi and R. G. Griffin. *Heteronuclear decoupling in rotating solids*. J. Chem. Phys. **103**, 6951–6958 (1995).

80. G. A. Morris and R. Freeman. *Enhancement of Nuclear Magnetic Resonance Signals by Polarization Transfer*. J. Am. Chem. Soc. **101**, 760 (1979).

81. J. D. Gross, P. R. Costa, J. P. Dubacq, D. E. Warchawski, P. N. Lirsac, P. F. Devaux and R. G. Griffin. *Multidimensional NMR in Lipid Systems. Coherence Transfer through J Couplings under MAS*. J. Magn. Reson. B **106**, 187 (1995).

82. A. Pines, M. G. Ginny and J. S. Waugh. *Proton-enhanced NMR of dilute spins in solids*. J. Chem. Phys. **59**, 569–590 (1973).

83. A. Nowacka, P. C. Mohr, J. Norrman, R. W. Martin and D. Topgaard. *Polarization Transfer Solid-State NMR for Studying Surfactant Phase Behavior*. Langmuir **26**, 16848–16856 (2010).

84. G. De Paëpe. *Dipolar Recoupling in Magic Angle Spinning Solid-State Nuclear Magnetic Resonance*. Annual Review of Physical Chemistry **63**, 661–684 (2012).

85. S. Caldarelli, M. Hong, L. Emsley and A. Pines. *Measurement of carbon-proton dipolar couplings in liquid crystals by local dipolar field NMR spectroscopy*. J. Phys. Chem. **100**, 18696–18701 (1996).

86. X. Zhao, M. Edén and M. H. Levitt. *Recoupling of heteronuclear dipolar interactions in solid-state NMR using symmetry-based pulse sequences*. Chem. Phys. Lett. **342**, 353 (2001).

87. S. V. Dvinskikh, H. Zimmermann, A. Maliniak and D. Sandström. *Measurement of motionally averaged heteronuclear dipolar couplings in MAS NMR using R-type recoupling*. J. Mag. Res. **168**, 194 (2004).

88. X. Zhao. *Symmetry-Based Heteronuclear Recoupling in Solid-State NMR.* Doctoral Dissertation (2003).

89. R A Bockmann, A Hac, T Heimburg and H Grubmuller. *Effect of sodium chloride on a lipid bilayer.* Biophys. J. **85**, 1647–1655 (2003).

90. A. Abragam. *Principles of Nuclear Magnetism.* Oxford University Press (1961).

91. J. Becker, A. Comotti, R. Simonutti, P. Sozzani and K. Saalwachter. *Molecular motion of isolated linear alkanes in nanochannels.* J. Phys. Chem. B **109**, 23285–23294 (2005).

92. H. Wennerström, B. Lindman, O. Söderman, T. Drakenberg and J. B. Rosenholm. ^{13}C *magnetic relaxation in micellar solutions - Influence of aggregate motion on T_1.* J. Am. Chem. Soc. **101**, 6860–6864 (1979).

93. B. Halle and H. Wennerström. *Interpretation of Magnetic-Resonance Data from Water Nuclei in Heterogeneous Systems.* J. Chem. Phys. **75**, 1928–1943 (1981).

94. G. Lipari and A. Szabo. *Model-Free Approach to the interpretation of Nuclear Magnetic REsonance Relaxation in MAcromolecules. 1. Theory and Range of Validity.* J. Am. Chem. Soc. **104**, 4546–4559 (1982).

95. D. A. Torchia. *The Measurement of Proton-Enhanced Carbon-13 T1 Values by a Method Which Suppresses Artifacts.* J. Mag. Res. **30**, 613–616 (1978).

96. F. de Meyer and Berend Smit. *Effect of cholesterol on the structure of a phospholipid bilayer.* Proceedings of the National Academy of Sciences **106**, 3654–3658 (2009).

97. T. J. McIntosh, S. A. Simon, D. Needham and C. H. Huang. *Structure and cohesive properties of sphingomyelin/cholesterol bilayers.* Biochemistry **31**, 2012–2020 (1992).

98. P.T.T. Wong, S.E. Capes and H.H. Mantsch. *Hydrogen bonding between anhydrous cholesterol and phosphatidylcholines: an infrared spectroscopic study.* Biochimica et Biophysica Acta (BBA) - Biomembranes **980**, 37 – 41 (1989).

99. J. Huang. *Chapter 12 Model Membrane Thermodynamics and Lateral Distribution of Cholesterol: From Experimental Data to Monte Carlo Simulation.* In *Biothermodynamics, Part A* volume 455 pages 329 – 364. Academic Press (2009).

100. J. B. Lim, B. Rogaski and J. B. Klauda. *Update of the Cholesterol Force Field Parameters in CHARMM.* J. Phys. Chem. B **116**, 203–210 (2012).

101. H. Schindler and J. Seelig. *Deuterium order parameters in relation to thermodynamic properties of a phosdpholipid bilayer – Statistical mechanical interpretation.* Biochemistry **14**, 2283–2287 (1975).

102. D. J. Tobias, T. Kechuan and M. L. Klein. *Atomic-scale molecular dynamics simulations of lipid membranes.* Current Opinion in Colloid & Interface Science **2**, 15 – 26 (1997).

103. D. P. Tieleman, S. J. Marrink and H. J. C. Berendsen. *A computer perspective of membranes: molecular dynamics studies of lipid bilayer systems.* Biochim. Biophys. Acta-Rev. Biomembr. **1331**, 235–270 (1997).

104. J. B. Klauda, R. M. Venable, A. D. MacKerell, Jr. and R. W. Pastor. *Considerations for lipid force field development.* In Feller, S E, editor, *Computational Modeling of Membrane Bilayers* volume 60 of *Current Topics in Membranes* pages 1–48. Elsevier San Diego (2008).

105. S. W. I. Siu, R. Vacha, P. Jungwirth and R. A. Boeckmann. *Biomolecular simulations of membranes: Physical properties from different force fields.* J. Chem. Phys. **128** (2008).

106. W. F. Van Gunsteren and H. J. C. Berendsen. *A leap-frog algorithm for stochastic dynamics.* Mol. Simul. **1**, 173–185 (1988).

107. P. M. Morse. *Diatomic molecules according to the wave mechanics. II. Vibrational levels.* Phys. Rev. **34**, 57–64 (1929).

108. J. P. Ryckaert and A. Bellemans. *Molecular dynamics of liquid normal butane near its boiling point.* Chem. Phys. Lett. **30**, 123–125 (1975).

109. T. G. Kucukkal and S. J. Stuart. *Polarizable Molecular Dynamics Simulations of Aqueous Dipeptides.* The Journal of Physical Chemistry B **116**, 8733–8740 (2012).

110. R. O. Dror, R. M. Dirks, J. P. Grossman, H. Xu and D. E. Shaw. *Biomolecular Simulation: A Computational Microscope for Molecular Biology.* In Rees, DC, editor, *Annu. Rev. Biophys.* volume 41 of *Annual Review of Biophysics* pages 429–452. ANNUAL REVIEWS (2012).

111. C. Predescu, R. A. Lippert, M. P. Eastwood, D. Ierardi, H. Xu, M. O. Jensen, K. J. Bowers, J. Gullingsrud, C. A. Rendleman, R. O. Dror and D. E. Shaw. *Computationally efficient molecular dynamics integrators with improved sampling accuracy.* Mol. Phys. **110**, 967–983 (2012).

112. O. Berger, O. Edholm and F. Jahnig. *Molecular dynamics simulations of a fluid bilayer of dipalmitoylphosphatidylcholine at full hydration, constant pressure, and constant temperature.* Biophys. J. **72**, 2002–2013 (1997).

113. J. B. Klauda, M. F. Roberts, A. G. Redfield, B. R. Brooks and R. W. Pastor. *Rotation of Lipids in Membranes: Molecular Dynamics Simulation, 31P Spin-Lattice Relaxation, and Rigid-Body Dynamics.* Biophys. J. **94**, 3074–3083 (2008).

114. N. V. Eldho, S. E. Feller, S. Tristram-Nagle, I. V. Polozov and K. Gawrisch. *Polyunsaturated Docosahexaenoic vs Docosapentaeoic Acid-Differences in Lipid Matrix Properties from the Loss of One Double Bond.* J. Am. Chem. Soc. **125**, 6409–6421 (2003).

115. S. E. Feller, K. Gawrisch and Jr. A. D. MacKerell. *Polyunsaturated Fatty Acids in Lipid Bilayers: Intrinsic and Environmental Contributions to Their Unique Physical Properties.* J. Am. Chem. Soc. **124**, 318 (2001).

116. Samuli Ollila, Marja T. Hyvonen and Ilpo Vattulainen. *Polyunsaturation in lipid membranes: Dynamic properties and lateral pressure profiles.* J. Phys. Chem. B **111**, 3139–3150 (2007).

117. R. W. Pastor and R. M. Venable. *A simulation based model of NMR T1 relaxation in lipid bilayer vesicles.* J. Chem. Phys. **89**, 1128 (1988).

118. R. W. Pastor, R. M. Venable and S. E. Feller. *Lipid Bilayers, NMR Relaxation, and Computer Simulations.* Acc. Chem. Res. **35**, 438–446 (2002).

Papers

PAPER I

Cholesterol and POPC segmental order parameters in lipid membranes: solid state ^{1}H–^{13}C NMR and MD simulation studies

Ferreira T. M., Gomes-Coreta F., Ollila O. H. S., Moreno M. J., Vaz W. L. C. , and Topgaard D..

PCCP

PAPER

Cholesterol and POPC segmental order parameters in lipid membranes: solid state ^{1}H–^{13}C NMR and MD simulation studies†

Tiago Mendes Ferreira,*[a] Filipe Coreta-Gomes,[b] O. H. Samuli Ollila,[a]
Maria João Moreno,[b] Winchil L. C. Vaz[b] and Daniel Topgaard[a]

The concentration of cholesterol in cell membranes affects membrane fluidity and thickness, and might regulate different processes such as the formation of lipid rafts. Since interpreting experimental data from biological membranes is rather intricate, investigations on simple models with biological relevance are necessary to understand the natural systems. We study the effect of cholesterol on the molecular structure of multi-lamellar vesicles (MLVs) composed of 1-palmitoyl-2-oleoyl-*sn-glycero*-3-phosphocholine (POPC), a phospholipid ubiquitous in cell membranes, with compositions in the range 0–60 mol% cholesterol. Order parameters, $|S_{CH}|$, are experimentally determined by using ^{1}H–^{13}C solid-state nuclear magnetic resonance (NMR) spectroscopy with segmental detail for all parts of both the cholesterol and POPC molecules, namely the ring system and alkyl chain of the sterol, as well as the glycerol backbone, choline headgroup and the *sn*-1 and *sn*-2 acyl chains of POPC. With increasing cholesterol concentration the acyl chains gradually adopt a more extended conformation while the orientation and dynamics of the polar groups are rather unaffected. Additionally, we perform classical molecular dynamics simulations on virtual bilayers mimicking the POPC–cholesterol MLVs investigated by NMR. Good agreement between experiments and simulations is found for the cholesterol alignment in the bilayer and for the $|S_{CH}|$ profiles of acyl chains below 15 mol% cholesterol. Deviations occur for the choline headgroup and glycerol backbone parts of POPC, as well as for the phospholipid and cholesterol alkyl chains at higher cholesterol concentrations. The unprecedented detail of the NMR data enables a more complete comparison between simulations and experiments on POPC–cholesterol bilayers and may aid in developing more realistic model descriptions of biological membranes.

Introduction

The preferred synthesis of cholesterol in mammalian cells over other sterols has been argued as an evolutionary step linked to the optimization of membrane cellular processes.[1–3] Mammals have an intricate homeostasis mechanism allowing precise control of cholesterol levels in their membranes.[4] Failure of these homeostatic processes may lead to severe disease, *e.g.* in humans with the genetic disease familial hypercholesterolemia, cholesterol levels rise manyfold above normal, leading to a

higher probability for heart attacks.[5,6] Cholesterol levels depend on cell and organelle type, being for instance around 17.5% of total dry weight in myelin but almost absent in mitochondrial membranes,[7,8] and ranging from 30–50 mol% of the total lipid fraction in plasma membranes.[9] The composition of biological membranes in terms of other lipid molecules than cholesterol and of membrane proteins also varies between cell and organelle types. Such differences are most likely related to the optimization of distinct functions on different membranes but a clear understanding of the reason for varying concentrations has not yet been established.

One aspect which is not fully rationalized is the dependence of membrane protein functionality on membrane lipid composition.[10] In some cases it may be understood by specific interactions between lipids and proteins while in other cases also the physical properties of the lipid bilayer might play a significant role.[10,11] The presence of cholesterol in biological

[a] *Physical Chemistry, Lund University, P.O. Box 124, SE-221 00 Lund, Sweden.
E-mail: tiago.ferreira@fkem1.lu.se*
[b] *Departamento de Química, Faculdade de Ciências e Tecnologia da Universidade
de Coimbra (FCTUC), Largo D. Dinis, Rua Larga, 3004-535 Coimbra, Portugal*
† Electronic supplementary information (ESI) available: Determination of the gaussian distributions for the cholesterol tilt angle. Calculation of maximum sizes for phase coexistence domains. See DOI: 10.1039/c2cp42738a

Cholesterol and POPC segmental order parameters in lipid membranes: solid state ^1H–^{13}C NMR and MD simulation studies

membranes is probably relevant in both cases. First of all, it increases the order of the lipid molecules as well as the thickness and stiffness of the bilayer. One consequence directly related to this effect is the decrease of the membrane's permeability to small molecules or ions. It has also been suggested, for instance, that the elastic properties of the bilayer may affect rhodopsin function[12] and that the increase in thickness of the endoplasmic reticulum membrane leads to the loss of activity of sarco(endo)plasmic reticulum ATPase.[13] On the other hand, the analysis of membrane protein extracts from cells indicates that cholesterol, or lipid molecules affected by cholesterol, might bind directly to specific proteins (ref. 10 and references therein). Furthermore, cholesterol is believed to play an important role in the formation of lipid rafts, *i.e.* postulated microdomains involved in the cell membrane biosynthetic and endocytic traffic.[14,15] Aside from the importance of cholesterol on the structural properties of membranes, it is also a precursor in the biological synthesis of a number of vital compounds such as bile salts, steroid hormones or vitamin D, to name a few.[16]

A detailed understanding of lipid bilayer properties is necessary to fully understand the biophysical issues discussed above. Here we report a study on bilayers consisting of mixtures with varying compositions of two biologically ubiquitous molecules, 1-palmitoyl-2-oleoyl-*sn-glycero*-3-phosphocholine (POPC) and cholesterol. Even though real biological membranes are substantially more complex, with several different kinds of molecules, these model systems are useful to understand basic effects of cholesterol on a cell membrane-like environment. We perform united-atom MD simulations of POPC–cholesterol bilayers, by using a commonly used united-atom model,[17] together with R-type proton-detected local field (R-PDLF) NMR experiments[18] on POPC–cholesterol multi-lamellar vesicles (MLVs). Atomistic (or nearly atomistic) MD simulation techniques currently provide the most detailed molecular descriptions available on model membrane systems, and NMR is a powerful and non-invasive technique to determine detailed properties of model membranes with atomic resolution. These two techniques complement each other since MD simulations enable the interpretation of NMR data to be more comprehensive while, on the other hand, quantitative comparisons between MD and NMR observables help to optimize the force-fields used in the simulations.

R-PDLF NMR spectroscopy is a recent alternative over the more conventional ^{2}H NMR methods to measure order parameters, S_{CH}, for individual C–H bonds,

$$S_{CH} = \tfrac{1}{2}\langle 3\cos^2\theta - 1\rangle, \qquad (1)$$

where θ is the angle between the direction of the C–H bond and the bilayer normal. In this work we show that by performing R-PDLF NMR on samples with natural abundance of isotopes it is possible to determine $|S_{CH}|$ values for almost all C–H segments in POPC–cholesterol bilayers, both from POPC and cholesterol molecules simultaneously. These experimental measurements show that while the phospholipid acyl chain tails reorient towards having more *trans* conformations,

the orientation and dynamics of the polar groups are rather unaffected through cholesterol concentrations in the range of 0–60 mol%. The highly selective and detailed information from R-PDLF NMR experiments enables a significantly better comparison between the simulation model and experimental results than previously.[19–23] Our results show that the ordering of acyl chains induced by cholesterol is very well described by the MD model at low cholesterol concentration. On the other hand, the choline headgroup, glycerol backbone, and acyl chains at higher concentrations, give different C–H order parameters than the NMR experiments; and the independence of the polar headgroup structure of POPC on cholesterol concentration is not captured. Moreover, a comparison of experimental and MD simulation cholesterol order parameters shows that while the ring structure is well described by simulations, this is not the case for the flexible alkyl chain of the sterol.

We expect that the results and discussion given here – pointing out a number of molecular details on the POPC–cholesterol bilayer structure and confronting the simulations to the new collection of NMR data – will aid in the development of more realistic model descriptions of biological membranes.

Materials and methods

Preparation of POPC–cholesterol MLVs

Cholesterol, 1-palmitoyl-2-oleoyl-phosphatidylcholine (POPC) and POPC deuterated at the *sn*-1 chain (POPC-d31) was from Avanti Polar Lipids (Alabaster, AL). Chloroform and methanol were purchased from Sigma. All reagents used were of the highest commercially available purity. Aqueous suspensions of lipids were prepared as described previously in ref. 24. The multi-lamellar dispersions were then centrifuged, the supernatants were discarded and the pellets were transferred to Bruker 4 mm HR-MAS rotors with a sample volume of 12 µl. Phospholipid concentrations were determined through a modified version of the Bartlett phosphate assay[25] and cholesterol concentrations were determined by the Lieberman–Burchard method as described in ref. 26. Absorption spectra were recorded on a Unicam UV530UV/Vis spectrophotometer. For samples with higher cholesterol content, the cholesterol/POPC ratio was calculated from ^{13}C direct polarization experiments (90° pulse and acquisition with TPPM decoupling[27] on the ^{1}H channel, details below). The quantification was done by integrating the peaks at 13.9 ppm and 12.2 ppm in the ^{13}C spectrum, corresponding to the methyl groups of the acyl chains of POPC and to one of the methyl groups in the cholesterol ring structure respectively. The concentrations studied were as follows: 0%, 7%, 15%, 34%, 50% and 60% of cholesterol (mol%) in the total amount of POPC + cholesterol lipid moles. Two independent samples were used for measurements at each concentration.

R-PDLF, INEPT and CP ^{1}H–^{13}C NMR experiments

The measurements were performed using a Bruker Avance AVII-500 NMR spectrometer operating at a ^{1}H frequency of

                                                                                    Paper

500.23 MHz equipped with a standard bore 4 mm CP-MAS HX probe. All experiments were done with the sample under magic angle spinning (MAS) at the spinning frequency of 5 kHz. The separated local field (SLF) experiment R-PDLF (ref. 18 and 28 for more details) was used with refocused INEPT[29,30] or CP[31] as the polarization transfer method. The following setup was used: spectral width of 149.5 ppm; refocused INEPT with τ_1 and τ_2 of 1.79 ms and 1.19 ms respectively; CP contact time equal to 700 μs; radiofrequency pulses set to give the nutation frequencies: 45.00 kHz (R18$_1^7$ pulses), 63.45 kHz (^{13}C 90° and 180° pulses), 63.45 kHz (^{1}H INEPT pulses), 50 kHz (^{1}H decoupling pulses), 50.76–63.45 kHz (^{1}H CP ramp pulse during contact time), 53.66 kHz (^{13}C CP pulse during contact time); t_1 with increments equal to 399.6 μs (0% colesterol, 7% and 15% cholesterol) and 132.2 μs (34% colesterol, 50% and 60% cholesterol); for each t_1 value, 256 scans were recorded during an acquisition time of 100 ms using 5 s recycle delay. MAS and RF heating effects were checked by using a rotor with methanol.[32] A difference of 1.55 ppm between the two peaks of the ^{1}H NMR spectrum of methanol was measured before and immediately after performing the longest of all R-PDLF experiments, giving a constant effective temperature of 300 K.

After performing a 2D spectral processing scheme to the time domain results as described in ref. 28, one gets a 2D spectrum with a number of splittings at different positions. The two dimensions of the spectrum correspond to the ^{13}C chemical shift that gives resolution for the different segments (direct dimension) and to the dipolar field recoupled during t_1 from which the order parameters may be calculated (indirect dimension). The size of the splittings, $\Delta\nu_{CH}$, at the different chemical shifts is proportional to the effective dipolar coupling, d_{CH}, by $\Delta\nu_{CH} = 0.315\ d_{CH}$, which in turn is proportional to the order parameter magnitude, $|S_{CH}|$ (eqn (1)), through,

$$d_{CH} = \frac{\hbar}{2}\left(\frac{\mu_0}{4\pi}\right)\gamma_H\gamma_C\langle r^{-3}\rangle|S_{CH}|, \qquad (2)$$

with μ_0 being the vacuum permittivity, γ_H and γ_C the gyromagnetic constants for the ^{1}H and the ^{13}C nuclei and $\langle r^{-3}\rangle$ the average inverse cubic length for a CH chemical bond. We assume a ^{1}H–^{13}C rigid lattice value d_{CH}^{max} = 21.5 kHz (for $|S_{CH}|$ = 1).[33]

MD simulation setup of the POPC–cholesterol bilayers

Molecular dynamics simulations were run by using the GROMACS 4.5.3 simulation package.[34–37] For POPC we used the same force-field as in ref. 38 which is based on the Berger parametrization for lipids,[39] except that dihedrals next to double bonds are described as in ref. 40. A GROMOS based force-field for cholesterol was taken from ref. 41. The use of these force-fields is a common procedure in several previous simulations (ref. 17 and references therein). The molecule types in the cholesterol force-field were changed from CH_2/CH_3 to LP_2/LP_3 to avoid overcondensation of the bilayer as suggested in ref. 42. All the initial structures were bilayers – consisting of
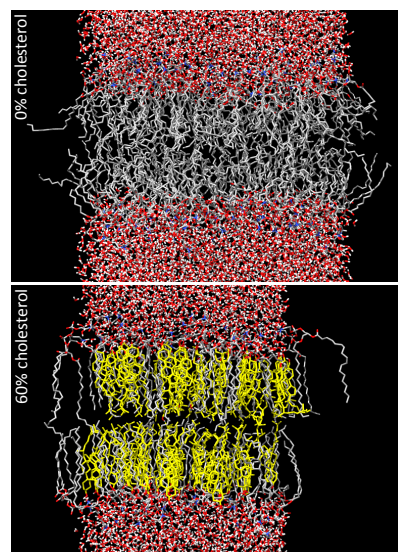
Fig. 1 MD simulation snapshots of a POPC bilayer and a POPC–cholesterol bilayer after 20 ns of equilibration. The colors identify different atoms/molecules: red is used for oxygen, white for hydrogens, blue for nitrogen, and grey and yellow denote the carbons from POPC and cholesterol respectively. The view scale used to generate the pictures was the same. Periodic boundary conditions were used in all directions.

two leaflets, each with 64 lipid molecules, and both having the same composition – hydrated with at least 3000 water molecules. Snapshots for two of the systems simulated are shown in Fig. 1. Energy minimization *via* the steepest descent method was done for all initial structures.

All simulations were carried out with the Berendsen thermostat and barostat[43] with pressure and temperature coupling constants of 1.0 ps and 0.1 ps respectively. The phospholipid, cholesterol and water molecules were separately coupled to a heat bath at 300 K, and the semi-isotropic pressure coupling was applied separately in the xy-direction (bilayer plane) and the z-direction (bilayer normal) with a coupling constant of 1 bar. Cutoff radius for van der Waals interactions was set to 1.0 nm. Particle mesh Ewald (PME) summations[44] were applied for long-range electrostatic interactions with a grid spacing of 0.12 nm and a cutoff radius of 1.0 nm was employed for real space summation. The time step was 2 fs, using LINCS[45] to constrain all bond lengths of lipids, whereas the SETTLE[46] algorithm was used for the SPC water.[47] The atoms coordinates were saved each 10 ps. The total time for simulations was 100 ns for each system from which only the last 80 ns were used for calculating averages.

Cholesterol and POPC segmental order parameters in lipid membranes: solid state ^{1}H–^{13}C NMR and MD simulation studies

C–H order parameters were calculated by first generating the hydrogen locations for all molecules in each time configuration. Then we use the equation

$$S_{CH} = \frac{1}{2NM} \sum_{m=1}^{M} \sum_{n=1}^{N} \left(\frac{3r_{nm,z}^{2}}{|\vec{r}_{nm}|^{2}} - 1 \right), \qquad (3)$$

where $\vec{r}_{nm}$ is the C→H vector of the C–H bond at molecule m and time frame n, with coordinates relative to an axis coordinate frame which has the z-axis parallel to the bilayer normal. The sum goes through all M molecules and N time frames. Note that in some cases the order parameter can be different for the different hydrogens connected to the same carbon. We calculate and report order parameters separately for all hydrogens. This discrimination is important since the two separate values can often be measured from experiments as well.

Results

Assignment of the ^{13}C chemical shifts and complete $|S_{CH}|$ profile of the phospholipid bilayer

A R-PDLF spectrum of POPC MLVs at full hydration is shown in Fig. 2 (for an explanation of the spectrum see the last paragraph of NMR experiments in Materials and Methods). Assignments for the glycerol, choline and some of the acyl chain ^{13}C peaks can be found in the literature,[48] but there is no previous detailed assignment of the several peaks in the crowded spectral region between 29 and 31 ppm. To determine the complete $|S_{CH}|$ profile from 2D (chemical shift–dipolar coupling) NMR spectroscopy such ^{13}C assignments must also be performed. In order to identify the previously unassigned ^{13}C peaks, we first distinguish the sn-1 (palmitoyl) peaks from the sn-2 (oleoyl) peaks. This distinction is done by performing R-PDLF experiments for two different samples of POPC MLVs in excess water: one having natural abundance of isotopes and another where the phospholipids have a fully deuterated sn-1 chain (POPC-d31). At the bottom of Fig. 2 we show
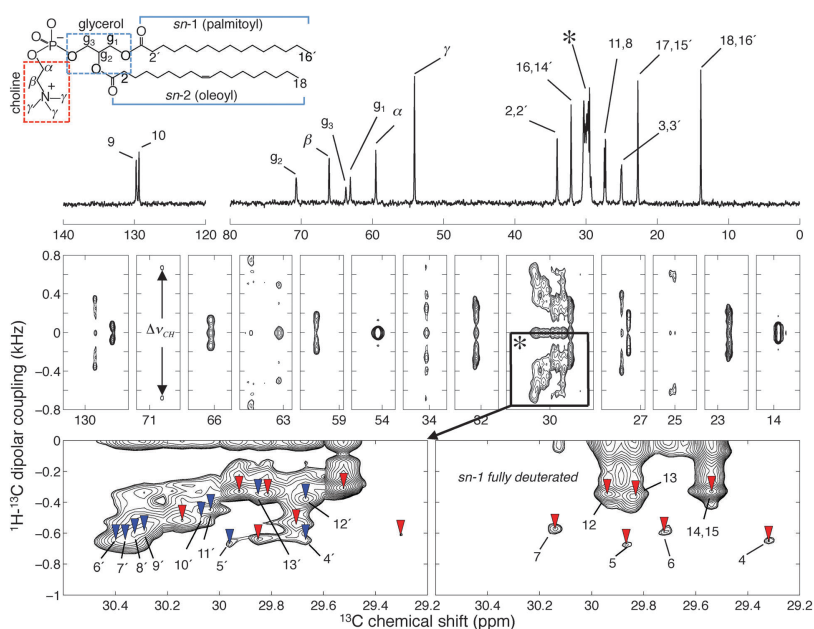
Fig. 2 2D ^{1}H–^{13}C R-PDLF spectrum of fully hydrated POPC multi-lamellar vesicles recorded at 300 K and B_0 = 11.74 T with INEPT polarization transfer, 5 kHz magic-angle spinning, 50 kHz TPPM ^{1}H decoupling during ^{13}C acquisition, and 45 kHz R18$_1^7$ ^{1}H–^{13}C dipolar recoupling in the indirect dimension. The peak for the CH$_3$ carbons C$_{18}$ and C$_{16'}$ is used as chemical shift reference at 13.9 ppm. Peak assignments as reported by Volke et al.[48] (*) Previously unassigned crowded spectral region around 30 ppm shown in detail for POPC (bottom, left) and POPC-d31 (bottom, right) multi-lamellar vesicles. Peaks from the sn-1 (palmitoyl) and sn-2 (oleoyl) chains are labeled with blue and red triangles respectively. The order parameters of the distinct carbons can be calculated from their splittings, $\Delta\nu_{CH}$.

magnifications of the R-PDLF spectra for POPC and POPC-d31 at the crowded spectral regions. The *sn*-1 chain ^{13}C signals in the deuterated sample are not present since the source of magnetization transfer from protons to carbons was removed. Likewise, the bottom right spectra in Fig. 2 only shows peaks from the *sn*-2 chain. By comparing these spectra it is then possible to identify which peaks belong to the *sn*-1 and *sn*-2 chains. The next step is performing the peak assignment for each of these sets of palmitoyl and oleoyl segments. Our choice here is made such that, for these previously unassigned ^{13}C peaks, the $|S_{CH}|$ profile mimics the profile predicted from the MD simulation. This identification based on MD is done exclusively for the previously unassigned ^{13}C peaks and solely for the sample without cholesterol. The initial ^{13}C NMR assignment is then kept consistently throughout the study.

The complete order parameter profiles obtained from both experiments and simulations are shown in Fig. 3. For

comparison we also show previously measured order parameters for *sn*-1 chain,[49] *sn*-2 chain[49,50] and for the polar headgroup region.[51] Note that, when it comes to simulations, we always show the individual order parameters from the two distinct hydrogens in a CH$_2$ group, while from the NMR experiments we can often only measure one order parameter from each methylene. If only one point is visible from simulations (red dots) it means that the two points overlap.

Cholesterol $|S_{CH}|$ profile

At higher concentrations of cholesterol it is also possible to determine a large number of cholesterol ^{1}H–^{13}C dipolar splittings from CP based R-PDLF experiments as shown in Fig. 4. The efficiency of the CP polarization transfer depends on both the order parameter and correlation time, τ_c, for C–H reorientation.[52] Since τ_c is most likely the same for both hydrogens in the same CH$_2$ group, the C–H pair with a higher $|S_{CH}|$ value will have a higher CP signal,[52] hence obscuring the signal of its complementary C–H pair. Thus, although two distinct ^{13}C–^{1}H dipolar couplings are expected for each CH$_2$ segment at the cholesterol ring structure, due to their rigid nature, it is only possible to measure directly the dipolar coupling corresponding to the highest $|S_{CH}|$ value. We resolve unambiguously order parameters for all the CH$_2$, CH$_3$ and C–H
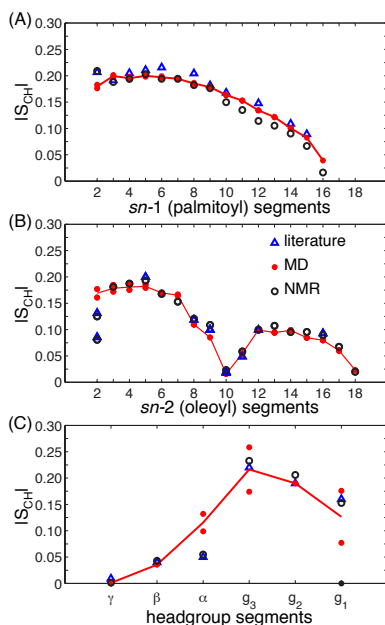
Fig. 3 Order parameter magnitude $|S_{CH}|$ *vs.* carbon segment number for the *sn*-1 and *sn*-2 acyl chains of POPC (A and B respectively); and for the choline and glycerol backbone of the POPC headgroup (C). Data from fully hydrated POPC at 300 K obtained with ^{1}H–^{13}C solid-state NMR (black dots) and MD simulations (red dots), as well as literature data (blue triangles) from ^{2}H NMR (*sn*-1[49] and *sn*-2[49,50] at 300 K) and ^{1}H–^{13}C NMR (headgroup in samples of egg yolk lecithin at 305 K[51]).
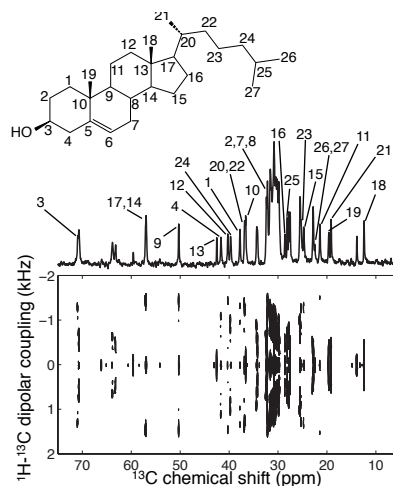
Fig. 4 2D ^{1}H–^{13}C R-PDLF spectrum of fully hydrated POPC–cholesterol multi-lamellar vesicles with 60 mol% cholesterol at 300 K and B_0 = 11.74 T with CP polarization transfer, 5 kHz magic-angle spinning, 50 kHz TPPM ^{1}H decoupling during ^{13}C acquisition, and 45 kHz R18$_1^7$ ^{1}H–^{13}C dipolar recoupling in the indirect dimension. The contact time for the CP transfer was 700 μs. A ^{13}C CP 1D spectrum is also shown with assignments of the cholesterol peaks. The assignment was based on the publication by Soubias *et al.*[53]

segments of cholesterol, with the exception of C_6, from samples with natural abundance of isotopes. The assignment of the sterol peaks was based on a previous report by Soubias *et al.*[53] Previous measurements for cholesterol order parameters were restricted to C–H segments that may be selectively deuterated, such as C_2–C_7, C_{22} and C_{24}–C_{26}.[54–57]

Cholesterol effect on the phospholipid order parameters

To measure the cholesterol effect on the C–H order parameters of POPC, a combination of R-PDLF experiments with CP and INEPT as polarization transfer methods was used. The molecular dynamics and molecular structure in the membrane determine the intensities obtained from INEPT and CP experiments. While INEPT gives higher signal intensities than CP for spin systems with faster dynamics and low order parameters, as the dynamics slow down and/or the order parameters increase, there is a buildup of the CP intensities and concomitant decrease of the INEPT efficiency. A theoretical analysis of this effect may be found elsewhere.[52] To determine $|S_{CH}|$ for the different C–H segments

one may then choose to use two R-PDLF versions to measure order parameters from more dynamical segments (INEPT version) and from more rigid segments (CP version).

The effect of cholesterol on the C–H order parameters of the *sn*-1 (palmitoyl), *sn*-2 (oleoyl) and headgroup segments is shown in Fig. 5, as well as cholesterol C–H order parameters for the ring and tail parts of the sterol, from both MD simulations and NMR experiments. Note that again, individual values for the separate C–H bonds in CH$_2$ groups are always shown for simulations (red dots). Experimental values show only one order parameter value from the methylene groups (with exception of the segments g_1 and C_2 at the *sn*-2 chain of POPC). This observation results from the fact that the two distinct C–H pairs in the CH$_2$ group have the same motional average, $\langle \cos^2 \theta \rangle$, which is the case for phospholipid acyl chains, or that only one of the C–H pairs have appreciable efficiency of polarization transfer, which applies to the cholesterol ring structure.

Cholesterol induces an increase of the population of *trans* conformers in the *sn*-1 and *sn*-2 acyl chains of the phospholipid, and hence induces an increase of the $|S_{CH}|$ values from
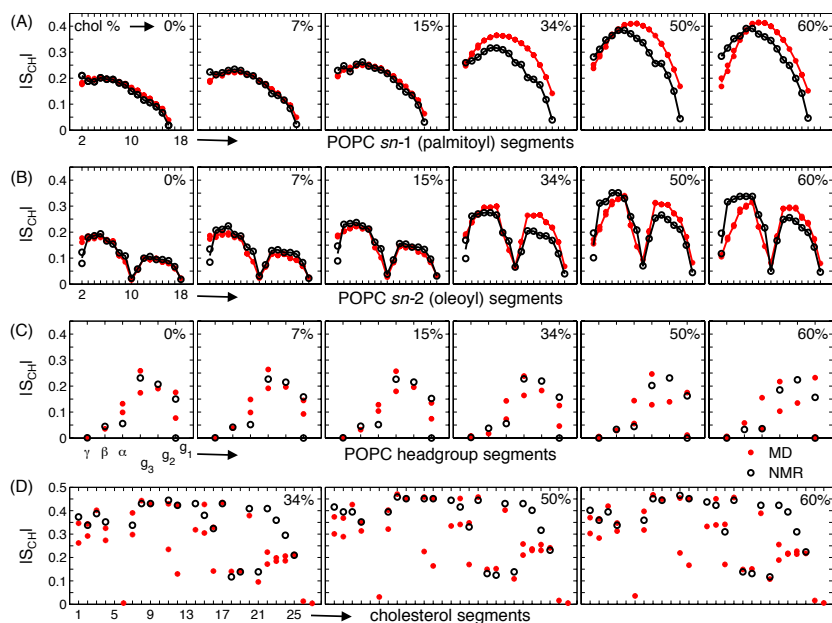
Fig. 5 Order parameter magnitude $|S_{CH}|$ *vs.* carbon segment number for the POPC *sn*-1 (palmitoyl), *sn*-2 (oleoyl) and headgroup chains (A, B and C respectively); as well as for the cholesterol ring and alkyl chain (D); in fully hydrated POPC–cholesterol bilayers at 300 K and a series of cholesterol concentrations. The $|S_{CH}|$ values were determined by ^1H–^{13}C solid-state NMR spectroscopy (black) and MD simulations (red). The solid lines in (A) and (B) follow the average values for each CH$_2$ segment. Note that, when it comes to simulations, we always show the individual order parameters from the different C–H bonds in a CH$_2$ group, while the NMR experiments often only yield the largest of the two values.

the hydrophobic region. This effect is seen from both MD simulations and experiments. On the other hand, the experimental $|S_{CH}|$ values for the polar headgroup are rather unaffected by cholesterol. This experimental observation is not captured in the MD simulations that predict $|S_{CH}|$ values for the g_1, g_2, g_3, α and β segments which generally vary with respect to the cholesterol concentration. Moreover, all the experimental order parameters from the polar part of POPC are single valued for each carbon, with the exception of segment g_1, while the MD simulations predict two distinct order parameters for carbons g_1, g_3 and α.

Discussion

The pure phospholipid bilayer structure: MD *vs.* NMR

Hydrophobic region. Order parameters for acyl chains in pure phospholipid bilayers have been extensively studied by means of NMR experiments and simulations. The first ^{2}H NMR measurements were done in the 70's and since then the techniques have been widely used on these systems. Less publications exist with order parameters determined by ^{1}H–^{13}C NMR. A NMR database for both these types of measurements in lipid bilayers has been reported recently.[58] Generally, the $|S_{CH}|$ values obtained in different experimental studies are in good agreement and MD simulations reproduce these results well. This observation applies also to our experimental and NMR results as seen in Fig. 3. Slight deviations between our experimental $|S_{CH}|$ values and the previous ^{2}H NMR $|S_{CD}|$ values might be due to experimental imperfections, such as amplitude missettings and inhomogeneities in the ^{1}H rf field that may lead to 5–10% error in the R-PDLF NMR measurements.[59] The good agreement between our experimental order parameter profiles and previous experimental measurements indicates that our ^{13}C peak assignment is reasonable.

Only the simulated order parameters for carbon C_2 of the *sn*-2 chain deviate considerably from the experimentally measured ones (Fig. 3B). R-PDLF NMR gives two distinct C–H order parameters for C_2 with lower values than the single order parameter value from the $C_{2'}$ methylene at the *sn*-1 chain (triple splitting pattern around 34 ppm in Fig. 2). This feature has also been systematically observed from phospholipids other than POPC with ^{2}H NMR experiments.[60] It has previously been shown that the Berger force-field, which is used in this work, gives equal order parameters for C_2 and $C_{2'}$,[61] but that other force-fields such as GAFF[61] and CHARMM C36[62] predict different values. However, these last force-fields also do not give distinct values for the different C–H bonds of the C_2 carbon in the *sn*-2 chain. It is known that the separate order parameters for C_2 are due to different motional averaging of the two C–H bonds,[63] *i.e.* the different bonds point on average in different directions with respect to the bilayer normal. Moreover, this difference is most likely due to different orientations of the C_1–C_2 bonds at the *sn*-1 (perpendicular to the membrane plane) and the *sn*-2 (parallel to the membrane plane) chains according to X-ray studies.[64,65] A correct prediction of these distinct C–H bond alignments by simulation models is most likely important for a proper description of the intermolecular interactions with the *sn*-2-carbonyl.

Table 1 Comparison between headgroup order parameters from different phospholipid bilayers

Carbon label	$|S_{CH}|^a$ POPC	S_{CH}^b DMPC	$|S_{CD}|^c$ DPPC	$|S_{CD}|^d$ E. coli
g_1	0.00	0.00	0.00	—
	0.15	−0.15	0.13	—
g_2	0.21	−0.20	0.20	—
g_3	0.23	−0.23	0.23	0.20
	—	—	0.21	0.21
α	0.06	+0.04	0.05	0.08
β	0.04	−0.03	0.04	0.03
γ	0.00	0.00	0.01	0.00

^{a} $|S_{CH}|$ from POPC MLVs at 300 K. ^{b} S_{CH} measured by Gross *et al.*[67] for DMPC at 303 K. ^{c} $|S_{CD}|$ from ^{2}H NMR on DPPC bilayers at 322 K published by Seelig and co-workers.[66] ^{d} $|S_{CD}|$ from ^{2}H NMR on *E. coli* phospholipids at 310 K by Gally *et al.*[68] Note that all columns show the absolute values of the order parameters except one, from Gross *et al.*,[67] who also measured the sign of the order parameters.

Choline headgroup and glycerol backbone. The order parameters of the headgroup and the glycerol backbone in other phospholipids than POPC have been investigated by means of ^{2}H NMR.[66–68] Previously published order parameters are shown in Table 1 together with our results. From the table we see that our results are very similar to the ones measured from phospholipid membranes containing dipalmitoylphosphatidylcholine (DPPC), dimyristoylphosphatidylcholine (DMPC) and lipids extracted from *E. coli*. As previously suggested by Gally *et al.*,[68] the similarity of the polar headgroup and glycerol backbone configuration in the four systems indicates that the general behavior of these groups is independent of the molecular structure in the hydrophobic region.

Table 1 shows that the two CH_2 segments in the glycerol backbone, C_{g1} and C_{g3}, have two distinct order parameters each. These differences are due to a motional non-equivalence of the individual C–H bonds of these segments. For C_{g1}, the difference between the two distinct C–H order parameters is large, with one of the C–H bonds retaining an angle close to the magic angle relative to the motional axis, and thus giving an order parameter very close to zero.[67]

On the other hand, the difference between the distinct $|S_{CH}|$ values from C_{g3} is very small. Although we could not measure such a slight difference because of insufficient resolution in the [1]H–[13]C dipolar coupling dimension of the R-PDLF experiment, it has been detected in previous ^{2}H NMR studies.[66,68]

Other types of anisotropic NMR interactions have been measured for the glycerol and choline moieties, *e.g.*, the ^{31}P chemical shift anisotropy (CSA) and a number of [31]P–[1]H and [31]P–[13]C dipolar couplings.[69] A large set of NMR observables available may be used as constraints to find an average structure for the polar group. The first detailed model for the structure of the choline headgroup and glycerol backbone was built based on ^{2}H and ^{31}P NMR results from DPPC bilayers and crystallography studies.[66,70] This model assumes rapid transitions between two enantiomeric choline states, a free rotation around the C_{g1}–C_{g2}–C_{g3}–O dihedral, and the assumption that the C_{g2}–C_{g3} bond is on average perpendicular to the plane of the bilayer.[66] Such description captures almost all

Cholesterol and POPC segmental order parameters in lipid membranes: solid state
^{1}H–^{13}C NMR and MD simulation studies

NMR parameters; however, the last two assumptions are not compatible with the two distinct order parameters for C_{g3}, and thus other models were proposed *e.g.* in which the angle of the C_{g1}–C_{g2}–C_{g3}–O dihedral was completely fixed.[69] In general, all the different models proposed share a strong similarity with the glycerol–choline headgroup structure of the DMPC-B conformer identified in DMPC solid crystals by Pearson and Pascher,[70] and a common feature in all the NMR-based descriptions is that the P–N electric dipole is oriented almost parallel to the plane of the membrane.

MD simulations would be a reasonable method for trying to find the more realistic description over the set of different models. However, the order parameters of the polar part of POPC calculated from our MD simulation model are rather different than the experimental values as seen in Fig. 3C, indicating that the used simulation model cannot describe the structure of the glycerol and choline groups with a high level of detail. Despite the experimental values available, this kind of comparisons to MD simulations have been rare. Only recently it was shown that the careful refinement of torsional parameters improved the all-atom CHARMM model for the polar headgroups.[62] Correct modeling of the choline headgroup and glycerol backbone orientation is highly important. For instance, a different orientation of the P–N dipole may lead to a different electrostatic potential around the membrane.

Cholesterol effect on the bilayer structure

Ordering of the acyl chains. In Fig. 5A and B we see a systematic increase in the acyl chain order parameters for both *sn*-1 and *sn*-2 chains when the cholesterol concentration increases. This effect, linked to condensation upon addition of cholesterol,[71,72] has been investigated by MD simulations and ^{2}H NMR for a large number of systems due to its possible implications on *lipid raft* formation and/or protein function regulation.[14,15] Also a ^{1}H–^{13}C recoupling NMR study on the effect of cholesterol on DOPC bilayers has been reported previously.[73] However, systematic and quantitative comparison between simulations and experiments has not been presented for the dependency of the complete acyl chain order parameter profile on cholesterol concentration.

At cholesterol molar fractions below 15%, Fig. 5A and B show a good agreement between measured and simulated acyl chain order parameters for both chains. The agreement is not as good for higher cholesterol concentrations, where the simulation model gives an overestimate of the ordering, mostly to the methylenes towards the center of the bilayer. Conversely, the order of carbons closer to the headgroup is underestimated at the highest concentrations. The most obvious reason for this discrepancy would be an inaccurate force-field description. Especially inter-molecular van der Waals interactions are difficult to parametrize and would be a plausible reason, although we removed one common feature that leads to over-condensation (we have changed CH_2/CH_3 groups in cholesterol to LP_2/LP_3 groups to make it more consistent with the Berger parameters).[42] Several other reasons related to the simulation force-field could explain the differences, such as the incorrect

orientation of the C_1–C_2 bond at the *sn*-2 chain or a wrong positioning of cholesterol molecules in the bilayer. Moreover, we cannot exclude also that the simulation might be too small in number of lipid molecules (128) and/or too short in time length (100 ns), since it is not clear from experimental studies if a change in phase morphology occurs above 15 mol% cholesterol. This possibility is discussed in more detail in a separate section.

The acyl chain ordering is related to the number of *gauche* and *trans* configurations along the chain, which in turn relates to how much the chain is stretched, *e.g.* the maximum stretch of the chain corresponds to an all-*trans* conformation. A number of models based on statistical mechanics have been proposed to describe this feature quantitatively. Such models provide relations between S_{CH} values of saturated acyl chains and methylene travel values,

$$\langle D_i \rangle = \langle z_{i-1} \rangle - \langle z_{i+1} \rangle, \tag{4}$$

where $\langle D_i \rangle$ is the average distance between two carbons, C_{i+1} and C_{i-1} bonded to carbon C_i, projected onto the bilayer normal.[74–76] Fig. 6A shows how well two of these models, namely the *diamond lattice* (DL)[75] and the *mean torque* (MT)[74] models, reproduce our MD data. The explicit equations for the relations $S_{CH} \rightarrow \langle D_i \rangle$ can both be found in ref. 74. Since the MT relation seems to give a better prediction of the values $\langle D_i \rangle$ for our MD simulations, we use this model to convert the ^{1}H–^{13}C NMR
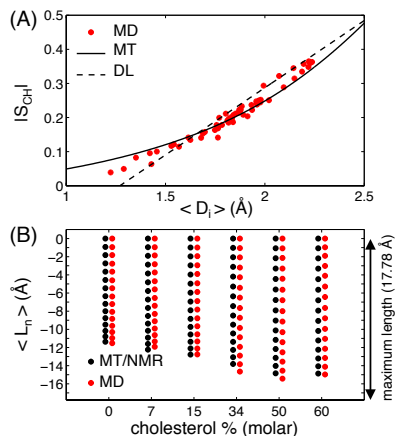
Fig. 6 (A) Acyl chain order parameter $|S_{CH}|$ *vs.* methylene travel $\langle D_i \rangle$ calculated with the mean torque (MT, solid line) and diamond lattice (DL, dashed line) models, as well as estimated directly from the MD simulations (red dots) for the *sn*-1 (palmitoyl) chains of all simulated systems. (B) Projected length in the bilayer normal of the *sn*-1 chain from MD simulations and by using the MT model[74] on ^{1}H–^{13}C NMR order parameters from fully hydrated POPC–cholesterol mixtures at 300 K.

order parameters of the POPC *sn*-1 chain to $\langle D_i \rangle$ values. Here, the projected length from carbon 2 to carbon n is defined as

$$\langle L_n \rangle = 1/2 \sum_{i=3}^{n} \langle D_i \rangle - D_n/2, \qquad (5)$$

Fig. 6B shows how the projected lengths of the *sn*-1 (palmitoyl) chain change as function of cholesterol concentration. The NMR data together with the MT model suggest that the *sn*-1 chain will stretch, with increasing cholesterol concentration, until it reaches a plateau value at around 50 mol% cholesterol. The directly simulated distance $\langle z_{16} \rangle - \langle z_2 \rangle$ and the total projected length determined using the experimental order parameters and the MT model of Petrache *et al.*[74] agree within an error of 1 Å. This indicates that even though a discrepancy between the $|S_{CH}|$ values from MD simulations and NMR experiments is found above 15 mol% of cholesterol, the length of the extension of the acyl chains in the MD simulations might be very close to the real one.

Effect on the structure and dynamics of the glycerol backbone and choline headgroup. A very small increase of the order parameters for segment C_{g2} and a more significant decrease for segment C_{g3} are seen with increasing cholesterol concentration, particularly at 50 and 60 mol% cholesterol, whereas segment C_{g1} maintains a constant order parameter through the entire range of cholesterol concentrations studied. It is also evident from the data presented in Fig. 5C that while the values for the order parameters for C_{g2} and C_{g3} maintain a fixed pattern relative to each other up to 34 mol% cholesterol, this trend changes at and above 50 mol% cholesterol. Equal order parameters for these segments would be expected to result from a parallel orientation of the C_{g2}–C_{g3} bond with respect to the bilayer normal.

Thus, we may interpret the unequal trends on C_{g2} and C_{g3} order parameters as a slight change of either the *gauche/trans* conformational distribution around the C_{g1}–C_{g2} bond, that may change the C_{g2}–C_{g3} bond orientation, and/or due to a possible change of the *gauche/trans* conformational distribution around the C_{g2}–C_{g3} bond. The variations in the $|S_{CH}|$ values of C_{g2} and C_{g3} may be a consequence of an increase in conformational entropy of the polar headgroup at the higher (50 and 60 mol%) cholesterol concentrations, *i.e.* an increase in free space available at the hydrophilic region.

For the choline group, a very modest decrease is seen for the C_α and C_β order parameters. This observation is in agreement with previous ^{2}H NMR studies on DPPC–cholesterol bilayers.[77] These changes can be explained by a slight change of 2.5° in the average dihedral angle N–C–C–O.[77] Moreover, a redistribution of conformational states usually leads to a variation of the ^{13}C chemical shifts (ref. 78 and references therein). The chemical shifts from the choline and glycerol carbons are essentially unchanged with the highest variation being 0.1 ppm for g_1, which is quite small compared to variations of about 1.5 ppm observed in the acyl chain groups. This indicates that unlike the *sn*-1 and *sn*-2 chains, the conformations of the glycerol and choline groups are rather unchanged.
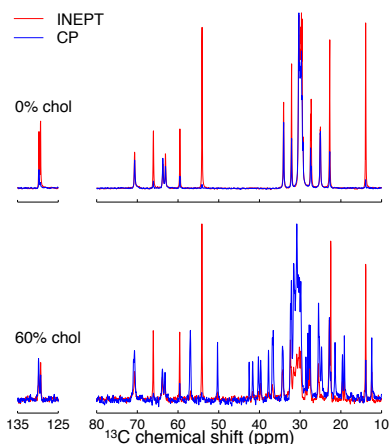

Fig. 7 Comparison of ^{13}C CP (blue) and refocused INEPT (red) spectra of fully hydrated multi-lamellar vesicles with different POPC–cholesterol compositions recorded at 300 K and $B_0 = 11.74$ T with 5 kHz magic-angle spinning and 50 kHz TPPM ^{1}H decoupling. The CP contact time was 700 μs. All four spectra were recorded with accumulation of 256 transients.

Qualitative information about C–H bond reorientation dynamics can be obtained from the ratios between the CP and INEPT peak intensities, which depend on both the order parameter and correlation time for reorientation.[52] CP and INEPT spectra are shown in Fig. 7 where ^{13}C peaks can be seen for the choline headgroup and glycerol backbone measured from POPC membranes with and without cholesterol. For choline headgroup carbons (54.1, 59.6 and 66.1 ppm) the CP/INEPT peak intensity ratio is low and does not change, but for the glycerol backbone carbons (63.1, 63.7 and 70.7 ppm) the CP signal is slightly enhanced when cholesterol is added. Since the order parameters are essentially unchanged for all the polar groups, we interpret the different CP/INEPT peak intensities as a slight slow down of the glycerol backbone dynamics due to incorporation of cholesterol and a high flexibility of the choline group which is not affected by cholesterol concentration.

Altogether, the present NMR results suggest that the choline headgroup order and dynamics are not significantly affected by cholesterol, while a very small effect is observed in the glycerol backbone. This observation is in good agreement with previous ^{2}H-NMR data on DPPC[77] and T_1(^{14}N) relaxation studies.[79] Such small variations in the order parameters and dynamics of the glycerol backbone obtained in this work are not reproduced by the MD simulations. Therefore, models for the effect of cholesterol on the headgroup structure based on the MD simulations using the present GROMOS and Berger force-fields or other force-fields lacking previous comparison with NMR experiments, as *e.g.* in ref. 80 and 81, may be misleading since the MD simulation outcome is unrealistic at this level of detail.

Cholesterol orientation in the bilayer

There is good agreement between simulations and experiments for the ring structure of cholesterol, except for C_{14} as shown in Fig. 5D. The discrepancy for C_{14} is surprising since all the other values in the rigid ring seem rather reasonable. In respect to the cholesterol alkyl chain, we observe clearly lower $|S_{CH}|$ values from simulations compared to the experimental ones for three carbons, C_{22}–C_{23}–C_{24}. Based on these observations, we suggest that while the behavior of the sterol rigid structure is well described by the simulation model, the cholesterol tail is either too flexible or incorrectly oriented. Just recently, Lim and coworkers have proposed a new CHARMM force-field for cholesterol which gives perfect agreement with C–D order parameters for the C_{22} and C_{24}–C_{26} cholesterol segments in DMPC bilayers.[82]

Since the rigid structure of the cholesterol ring system is known, a single value measured from any of the rings is enough to determine the average angle between the director axis of the cholesterol molecule and the membrane normal.[54,83] The precise orientation distribution of cholesterol is however not possible to be determined from these data alone, *i.e.* the same order parameters can be measured from a molecular axis vector fixed to a certain angle or fluctuating around it.[84] Below, we show how to determine the different possible orientation distributions from our NMR results and how MD simulations are specially useful to interpret the NMR measurements in this case.

In the traditional NMR approach, the order parameter for the director axis of the cholesterol molecule with respect to the bilayer normal, $S_\alpha = \frac{1}{2}\langle 3\cos^2\alpha - 1\rangle$, where α stands for the angle between the molecular director and the bilayer normal, is determined by using the equation

$$S_{CH} = \tfrac{1}{2}\langle 3\cos^2\alpha - 1\rangle\, \tfrac{1}{2}\langle 3\cos^2\beta - 1\rangle = S_\alpha S_\beta, \qquad (6)$$

where S_{CH} is the order parameter measured by NMR and S_β is the order parameter of the C–H bond relative to the molecular director which may be determined by knowing the rigid cholesterol structure.[83] This equation applies for any C–H bond in the rigid cholesterol ring. S_α can arise from several possible angle distributions, $f(\alpha)$, which satisfy the equation

$$S_\alpha = \frac{\int_0^\pi f(\alpha)\tfrac{1}{2}(3\cos^2\alpha - 1)\mathrm{d}\alpha}{\int_0^\pi f(\alpha)\mathrm{d}\alpha}, \qquad (7)$$

and the average angles for the different distributions may then be determined by

$$\langle \alpha \rangle = \frac{\int_0^\pi \alpha f(\alpha)\mathrm{d}\alpha}{\int_0^\pi f(\alpha)\mathrm{d}\alpha}. \qquad (8)$$

Generally, normal distribution functions are assumed,

$$f(\alpha) = \sin\alpha\, e^{-\frac{(\alpha-\alpha_0)^2}{\sigma^2}}, \qquad (9)$$

where $\sin\alpha$ accounts for the equal probability of the different orientations in a sphere. The gaussian term can be interpreted such that the cholesterol fluctuates around an angle α_0 with respect to the membrane normal, and an amplitude of fluctuations determined by σ. The assumption that these fluctuations have a gaussian form has also been used to analyze data from other rigid molecules such as pyrene or WALP23.[84–86] Since by using eqn (6) we may calculate S_α, it is possible then to determine which α_0 and σ values satisfy eqn (7).[83] Note that with the analysis above we get only a set of possible values for α_0, σ and $\langle\alpha\rangle$. On the other hand, the distribution for α can also be directly calculated numerically from molecular dynamics simulations.

We show in Fig. 8 such type of analysis for the cholesterol tilt in POPC–cholesterol bilayers containing 34 mol% cholesterol (see the ESI† for the explicit procedure). Fig. 8A shows that the average angle can be determined relatively unambiguously but the distribution can be something between two extreme cases: a tilt angle fixed at $17°$ or fluctuating in the range $0°$–$40°$. By comparing the possible gaussian distributions, from the set of solutions of eqn (7), with the numerical distribution obtained from the MD simulation (Fig. 8B, red), we find that the best analytical function to describe that the orientation
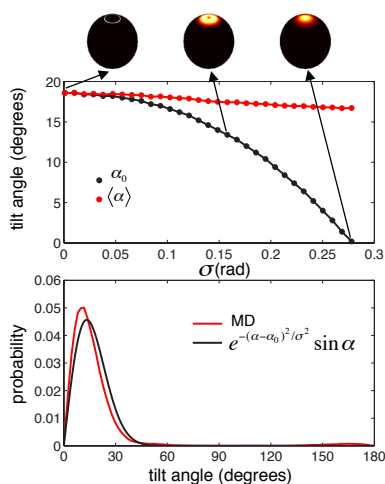

Fig. 8 (A) Possible gaussian distributions of the orientation of cholesterol in POPC–cholesterol MLVs (34 mol% cholesterol) at 300 K, based on the ^1H–^{13}C NMR dipolar coupling of the carbon bound to the hydroxyl group (C_3). For a particular distribution (σ and α_0, black), the standard deviation σ defines the range of angles that the molecular director of cholesterol ($C_{17}\rightarrow C_3$) may adopt relative to the bilayer normal and α_0 stands for the most energetically favorable angle. The average tilt angle for each possible distribution is also shown (red), as well as spheres mapping the probability of different orientations (dark to white is from lower to higher probability) for three distinct gaussian distributions. (B) Cholesterol tilt angle distributions in POPC–cholesterol bilayers (34 mol% cholesterol, 300 K) from MD simulations (red) and the gaussian distribution (black) which best fits the MD simulation: $\alpha_0 = 0°$ with a standard deviation of $\sigma = 16°$.

distribution has $\alpha_0 = 0°$ with standard deviation of $\sigma = 16°$ and average angle $\langle\alpha\rangle = 17°$, *i.e.* the tilt angle fluctuates between $0°–40°$ and the most energetically favorable orientation is when cholesterol is parallel to the bilayer normal.

Is there phase heterogeneity in the POPC–cholesterol system?

As discussed above, there is excellent agreement between acyl chain order parameters of POPC measured by NMR and calculated by MD simulations for concentrations of cholesterol up to 15 mol%. Above this value the simulated and experimentally measured order parameters diverge. Possible explanations regarding force-field issues have been discussed above. Another possibility is that some kind of lateral heterogeneity occurs for the POPC–cholesterol mixture above a certain cholesterol content. Since the initial configurations for our MD simulations were laterally homogeneous, the simulations of 100 ns may be too short and/or the size of the simulated systems too small to reach lateral heterogeneity. A liquid disordered/liquid ordered (L_d/L_o) phase coexistence has been suggested from fluorescence studies at 300 K (the temperature at which the present work was done) between 8 and 40 mol%[87] or between 12 and 45 mol%[88] cholesterol in the bilayers. Macroscopic phase separation into L_d and L_o would be detected in the R-PDLF experiment as the presence of both lower and higher distinct order parameters for each C–H bond. Just as in an earlier ^{2}H NMR study,[89] there are no indications of more than one order parameter per C–H bond for the fully hydrated POPC–cholesterol MLVs at 300 K. As justified in the ESI,† these observations show that if there is L_d/L_o separation, molecular exchange between the two phases must occur on a time scale much smaller than 10^{-5} s, corresponding to a lateral domain size much smaller than 100 nm.

Although the L_d/L_o coexistence[71] is generally accepted for binary mixtures of cholesterol and phospholipids with saturated acyl chains, such as DPPC[90,91] or sphingomyelin,[92] the existence of a phase separation in bilayers prepared from binary mixtures of cholesterol with phospholipids that have one saturated and one unsaturated acyl chain is not universally accepted and has been contested by various laboratories using very different methods: on the basis of in-plane translational diffusion studies without use of invasive probes,[93] from dilatometric studies (also without use of invasive probes),[94] from studies on the kinetics and thermodynamics of insertion of amphiphiles into lipid bilayers,[24] from the visualization of fluorescent membrane domains in giant lipid vesicles,[95] and most recently from a combination of several techniques[96] and from spin-label EPR studies.[97] Alternatively, 2D micelles formation in lipid bilayers prepared from binary mixtures of cholesterol and phospholipids with one saturated and one cis-unsaturated acyl chain, such as POPC, has been proposed, in which cholesterol represents the 2D core with the POPC molecules oriented such that the saturated acyl chain faces the sterol and the unsaturated point towards the outer part of the 2D micelle.[24] Since the components of the putative micelles would be in rapid equilibrium with the bulk lipid phase of the bilayers, this would be a case of microscopic heterogeneity, thermodynamically quite distinct from a phase separation. Due to the fast dynamics of micellization, this type of heterogeneity would not be detectable in our NMR experiments and the POPC–cholesterol bilayer would appear to be a single homogeneous phase.

We can neither rule out nor confirm the presence of any type of lateral heterogeneous domains smaller than 100 nm. Thus, it is not clear if the deviation between the $|S_{CH}|$ values from simulations and experiments is related to: (I) the onset of a certain phase transition, which could not be captured by the simulations due to the computational restrictions on system size and/or number of time steps performed; (II) simply because the force-field parametrization is not accurate enough to predict the effect of cholesterol on the acyl chains at this level of detail.

Conclusion

R-PDLF NMR, with CP and INEPT as alternate polarization transfer methods, is useful to study POPC bilayers which contain cholesterol since it provides a large set of detailed data on the molecular structure of both the phospholipid and cholesterol. The experimental data obtained suggest that, while acyl chains adopt more *trans* configurations, the behavior of the glycerol backbone and the choline headgroup of POPC is rather independent of the cholesterol concentration.

We have shown that a widely used MD simulation model for phospholipid–cholesterol mixtures reproduces well the ordering effect of cholesterol upon the POPC acyl chains at cholesterol concentrations up to 15 mol% but deviates from the experimentally observed NMR results above this concentration. The cholesterol ring structure is also well reproduced at all cholesterol concentrations examined.

The unprecedented detail of the experimental data allows us to point out four main deficiencies of the MD simulation model:

(I) The experimental order parameters for the POPC choline headgroup and glycerol backbone and their qualitative behavior as a function of cholesterol are not correctly predicted by the used simulation model. The development of a more accurate model of the phospholipid headgroup is most likely important since such type of models are often used to study detailed interactions between the phospholipid headgroup and other molecules, like cholesterol or proteins.[17,98]

(II) Acyl chain order parameters are not well reproduced with cholesterol concentrations of 34 mol% cholesterol and higher. It is not clear though if this deviation arises from problems in the force-field or from lateral heterogeneity in the bilayer which could not be captured in the present simulations.

(III) The experimental order parameters of the cholesterol alkyl chain are not reproduced by simulations, meaning an incorrectly oriented or too flexible alkyl chain. The most likely reason is that the dihedral angle parameters for the alkyl chain are not properly defined in this model. A better description of the cholesterol alkyl chain is important for interactions between cholesterol and other molecules at the center of the bilayers.

(IV) The distinct POPC experimental order parameters for segment C_2 for each acyl chain may be interpreted to be due to a different orientation of the C_1–C_2 bond of the *sn*-2 chain (parallel to the bilayer plane) compared to the orientation of the C_1–$C_{2'}$ at the *sn*-1 chain (parallel to the bilayer normal). This difference is not captured by the simulation model and may be important for describing phospholipid–cholesterol interactions.

The main relevance of this work is that it has been possible to measure a vast number of C–H order parameters, from both POPC and cholesterol molecules, that had not been previously measured by ^2H NMR methods. We believe that the experimental data presented here may be an important contribution to the development of more realistic force-fields for MD simulations.

References

1 K. E. Bloch, *Crit. Rev. Biochem.*, 1979, **7**(1), 1–5.
2 K. E. Bloch, *Crit. Rev. Biochem.*, 1983, **14**(1), 47–92.
3 D. E. Vance and H. V. den Bosch, *Biochim. Biophys. Acta, Mol. Cell Biol. Lipids*, 2000, **1529**(1–3), 1–8.
4 J. L. Goldstein and M. S. Brown, *Nature*, 1990, **343**(6257), 425–430.
5 F. R. Maxfield and I. Tabas, *Nature*, 2005, **438**(7068), 612–621.
6 D. W. Bilheimer, S. M. Grundy, M. S. Brown and J. L. Goldstein, *PNAS*, 1983, **80**, 4124–4128.
7 G. Saher, B. Brugger, C. Lappe-Siefke, W. Mobius, R. Tozawa, M. Wehr, F. Wieland, S. Ishibashi and K. Nave, *Nat. NeuroSci.*, 2005, **8**(4), 468–475.
8 J. Montero, A. Morales, L. Llacuna, J. M. Lluis, O. Terrones, G. Basañez, B. Antonsson, J. Prieto, C. García-Ruiz, A. Colell and J. C. Fernandez-Checa, *Cancer Res.*, 2008, **68**(13), 5246–5256.
9 L. Miao, M. Nielsen, J. Thewalt, J. H. Ipsen, M. Bloom and M. J. Zuckermann, *Biophys. J.*, 2002, **82**(3), 1429–1444.
10 A. G. Lee, *Biochim. Biophys. Acta, Biomembr.*, 2004, **1666**(1–2), 62–87.
11 R. Phillips, T. Ursell, P. Wiggins and P. Sens, *Nature*, 2009, **459**(7245), 379–385.
12 O. H. S. Ollila, T. Rog, M. Karttunen and I. Vattulainen, *J. Struct. Biol.*, 2007, **159**(2), 311–323.
13 Y. K. Li, M. T. Ge, L. Ciani, G. Kuriakose, E. J. Westover, M. Dura, D. F. Covey, J. H. Freed, F. R. Maxfield, J. Lytton and I. Tabas, *J. Biol. Chem.*, 2004, **279**(35), 37030–37039.
14 K. Simons and W. L. C. Vaz, *Annu. Rev. Biophys. Biomol. Struct.*, 2004, **33**, 269–295.
15 K. Simons and E. Ikonen, *Nature*, 1997, **387**(6633), 569–572.
16 T. Kurzchalia and S. Ward, *Nat. Cell Biol.*, 2003, **5**(8), 684–688.
17 T. Rog, M. Pasenkiewicz-Gierula, I. Vattulainen and M. Karttunen, *Biochim. Biophys. Acta, Biomembr.*, 2009, **1788**(1, SI), 97–121.
18 S. V. Dvinskikh, H. Zimmermann, A. Maliniak and D. Sandström, *J. Magn. Reson.*, 2004, **168**, 194.
19 T. Rog and M. Pasenkiewicz-Gierula, *Biochimie*, 2006, **88**(5), 449–460.
20 J. Aittoniemi, P. S. Niemela, M. T. Hyvonen, M. Karttunen and I. Vattulainen, *Biophys. J.*, 2007, **92**(4), 1125–1137.
21 S. Mondal and C. Mukhopadhyay, *Chem. Phys. Lett.*, 2007, **439**(1–3), 166–170.
22 S. A. Pandit, S.-W. Chiu, E. Jakobsson, A. Grama and H. L. Scott, *Langmuir*, 2008, **24**(13), 6858–6865.
23 S. Jo, H. Rui, J. B. Lim, J. B. Klauda and W. Im, *J. Phys. Chem. B*, 2010, **114**(42), 13342–13348.
24 L. M. B. B. Estronca, M. J. Moreno and W. L. C. Vaz, *Biophys. J.*, 2007, **93**(12), 4244–4253.
25 G. R. Bartlett, *J. Biol. Chem.*, 1959, **234**, 466–468.
26 R. P. Taylor, A. V. Broccoli and C. M. Grisham, *J. Chem. Educ.*, 1978, **55**, 63–64.
27 A. E. Bennett, C. M. Rienstra, M. Auger, K. V. Lakshmi and R. Griffin, *J. Chem. Phys.*, 1995, **103**(16), 6951–6958.
28 T. M. Ferreira, B. Medronho, R. W. Martin and D. Topgaard, *Phys. Chem. Chem. Phys.*, 2008, **10**(39), 6033–6038.
29 G. A. Morris and R. Freeman, *J. Am. Chem. Soc.*, 1979, **101**, 760.
30 J. D. Gross, P. R. Costa, J. P. Dubacq, D. E. Warchawski, P. N. Lirsac, P. F. Devaux and R. G. Griffin, *J. Magn. Reson., Ser. B*, 1995, **106**, 187.
31 A. Pines, M. G. Ginny and J. S. Waugh, *J. Chem. Phys.*, 1973, **59**(2), 569–590.
32 A. L. V. Geet, *Anal. Chem.*, 1970, **42**, 679.
33 S. V. Dvinskikh, V. Castro and D. Sandström, *Phys. Chem. Chem. Phys.*, 2005, 7, 607.
34 H. J. C. Berendsen, D. van der Spoel and R. van Drunen, *Comput. Phys. Commun.*, 1995, **91**(1–3), 43–56.
35 E. Lindahl, B. Hess and D. van der Spoel, *J. Mol. Model.*, 2001, **7**(8), 306–317.
36 D. Van der Spoel, E. Lindahl, B. Hess, G. Groenhof, A. E. Mark and H. J. C. Berendsen, *J. Comput. Chem.*, 2005, **26**(16), 1701–1718.
37 B. Hess, C. Kutzner, D. van der Spoel and E. Lindahl, *J. Chem. Theory Comput.*, 2008, **4**(3), 435–447.
38 S. Ollila, M. T. Hyvonen and I. Vattulainen, *J. Phys. Chem. B*, 2007, **111**(12), 3139–3150.
39 O. Berger, O. Edholm and F. Jahnig, *Biophys. J.*, 1997, **72**(5), 2002–2013.

40 M. Bachar, P. Brunelle, D. P. Tieleman and A. Rauk, *J. Phys. Chem. B*, 2004, **108**(22), 7170–7179.

41 M. Höltje, T. Förster, B. Brandt, T. Engels, W. von Rybinski and H. D. Holtje, *Biochim. Biophys. Acta, Biomembr.*, 2001, **1511**(1), 156–167.

42 D. P. Tieleman, J. L. MacCallum, W. L. Ash, C. Kandt, Z. T. Xu and L. Monticelli, *J. Phys.: Condens. Matter*, 2006, **18**(28), S1221–S1234.

43 H. J. C. Berendsen, J. P. M. Postma, W. F. Vangunsteren, A. Dinola and J. R. Haak, *J. Chem. Phys.*, 1984, **81**(8), 3684–3690.

44 U. Essmann, L. Perera, M. L. Berkowitz, T. Darden, H. Lee and L. G. Pedersen, *J. Chem. Phys.*, 1995, **103**(19), 8577–8593.

45 B. Hess, H. Bekker, H. J. C. Berendsen and J. G. E. M. Fraaije, *J. Comput. Chem.*, 1997, **18**(12), 1463–1472.

46 S. Miyamoto and P. A. Kollman, *J. Comput. Chem.*, 1992, **13**(8), 952–962.

47 H. J. C. Berendsen, J. P. M. Postma, W. F. van Gunsteren and J. Hermans, *Interaction models for water in relation to protein hydration*, Reidel Publishing Company, 1981.

48 F. Volke, R. Waschipky, A. Pampel, A. Donnerstag, G. Lantzsch, H. Pfeiffer, W. Richter, G. Klose and P. Welzel, *Chem. Phys. Lipids*, 1997, **85**(2), 115–123.

49 J. Seelig and N. Waespesarcevic, *Biochemistry*, 1978, **17**(16), 3310–3315.

50 B. Perly, I. C. P. Smith and H. C. Jarrell, *Biochemistry*, 1985, **24**(4), 1055–1063.

51 M. Hong, K. Schmidt-Rohr and D. Nanz, *Biophys. J.*, 1995, **69**(5), 1939–1950.

52 A. Nowacka, P. C. Mohr, J. Norrman, R. W. Martin and D. Topgaard, *Langmuir*, 2010, **26**(22), 16848–16856.

53 O. Soubias, F. Jolibois, V. Reat and A. Milon, *Chem.–Eur. J.*, 2004, **10**(23), 6005–6014.

54 E. Oldfield, M. Meadows, D. Rice and R. Jacobs, *Biochemistry*, 1978, **17**(14), 2727–2740.

55 M. G. Taylor, T. Akiyama and I. C. P. Smith, *Chem. Phys. Lipids*, 1981, **29**(4), 327–339.

56 E. J. Dufourc, E. J. Parish, S. Chitrakorn and I. C. P. Smith, *Biochemistry*, 1984, **23**(25), 6062–6071.

57 P. Marsan, I. Muller, C. Ramos, F. Rodriguez, E. J. Dufourc, J. Czaplicki and A. Milon, *Biophys. J.*, 1999, **76**(1, Part 1), 351–359.

58 A. Leftin and M. F. Brown, *Biochim. Biophys. Acta, Biomembr.*, 2011, **1808**(3), 818–839.

59 P. Schanda, B. H. Meier and M. Ernst, *J. Magn. Reson.*, 2011, **210**(2), 246–259.

60 J. H. Davis, *Biochim. Biophys. Acta*, 1983, **737**(1), 117–171.

61 S. W. I. Siu, R. Vacha, P. Jungwirth and R. A. Boeckmann, *J. Chem. Phys.*, 2008, **128**(12), 125103.

62 J. B. Klauda, R. M. Venable, J. A. Freites, J. W. O'Connor, D. J. Tobias, C. Mondragon-Ramirez, I. Vorobyov, A. D. MacKerell, Jr. and R. W. Pastor, *J. Phys. Chem. B*, 2010, **114**(23), 7830–7843.

63 A. K. Engel and D. Cowburn, *FEBS Lett.*, 1981, **126**(2), 169–171.

64 J. P. Douliez, A. Leonard and E. J. Dufourc, *Biophys. J.*, 1995, **68**(5), 1727–1739.

65 H. Hauser, I. Pascher, R. H. Pearson and S. Sundell, *Biochim. Biophys. Acta*, 1981, **650**(1), 21–51.

66 J. Seelig, H. Gally and R. Wohlgemuth, *Biochim. Biophys. Acta*, 1977, **467**(2), 109–119.

67 J. D. Gross, D. E. Warchawski and R. G. Griffin, *J. Am. Chem. Soc.*, 1997, **119**, 796.

68 H. U. Gally, G. Pluschkep, P. Overath and J. Seelig, *Biochemistry*, 1981, **20**(7), 1826–1831.

69 M. Hong, K. Schmidt-Rohr and H. Zimmermann, *Biochemistry*, 1996, **35**(25), 8335–8341.

70 R. Pearson and I. Pascher, *Nature*, 1979, **281**(5731), 499–501.

71 J. H. Ipsen, G. Karlström, O. G. Mouritsen, H. Wennerström and M. J. Zuckermann, *Biochim. Biophys. Acta*, 1987, **905**(1), 162–172.

72 D. P. Tieleman, S. J. Marrink and H. J. C. Berendsen, *Biochim. Biophys. Acta, Rev. Biomembr.*, 1997, **1331**(3), 235–270.

73 D. Warschawski and P. Devaux, *Eur. Biophys. J. Biophys. Lett.*, 2005, **34**(8), 987–996.

74 H. I. Petrache, S. W. Dodd and M. F. Brown, *Biophys. J.*, 2000, **79**(6), 3172–3192.

75 H. Schindler and J. Seelig, *Biochemistry*, 1975, **14**(11), 2283–2287.

76 L. R. De Young and K. A. Dill, *Biochemistry*, 1988, **27**(14), 5281–5289.

77 M. F. Brown and J. Seelig, *Biochemistry*, 1978, **17**(2), 381–384.

78 J. B. Rosenholm, T. Drakenberg and B. Lindman, *J. Colloid Interface Sci.*, 1978, **63**(3), 538–550.

79 K. Koga, Y. Tanaka and Y. Kanazawa, *Chem. Phys. Lipids*, 1985, **36**(3), 285–295.

80 M. Alwarawrah, J. Dai and J. Huang, *J. Chem. Theory Comput.*, 2012, **8**(2), 749–758.

81 M. C. Pitman, F. Suits, A. D. MacKerell and S. E. Feller, *Biochemistry*, 2004, **43**(49), 15318–15328.

82 J. B. Lim, B. Rogaski and J. B. Klauda, *J. Phys. Chem. B*, 2012, **116**(1), 203–210.

83 N. O. Petersen and S. I. Chan, *Biochemistry*, 1977, **16**(12), 2657–2667.

84 L. Monticelli, D. P. Tieleman and P. F. J. Fuchs, *Biophys. J.*, 2010, **99**(5), 1455–1464.

85 B. Hoff, E. Strandberg, A. S. Ulrich, D. P. Tieleman and C. Posten, *Biophys. J.*, 2005, **88**(3), 1818–1827.

86 E. Strandberg, S. Esteban-Martin, J. Salgado and A. S. Ulrich, *Biophys. J.*, 2009, **96**(8), 3223–3232.

87 C. R. Mateo, A. U. Acuna and J. C. Brochon, *Biophys. J.*, 1995, **68**(3), 978–987.

88 R. F. M. de Almeida, A. Fedorov and M. Prieto, *Biophys. J.*, 2003, **85**(4), 2406–2416.

89 J. L. Thewalt and M. Bloom, *Biophys. J.*, 1992, **63**(4), 1176–1181.

90 M. R. Vist and J. H. Davis, *Biochemistry*, 1990, **29**(2), 451–464.

91 T. McMullen, R. Lewis and R. McElhaney, *Curr. Opin. Colloid Interface Sci.*, 2004, **8**(6), 459–468.

92 M. B. Sankaram and T. E. Thompson, *Biochemistry*, 1990, **29**(47), 10670–10675.

93 A. Filippov, G. Oradd and G. Lindblom, *Biophys. J.*, 2003, **84**(5), 3079–3086.

94 A. I. Greenwood, S. Tristram-Nagle and J. F. Nagle, *Chem. Phys. Lipids*, 2006, **143**(1–2), 1–10.

95 S. Veatch and S. Keller, *Phys. Rev. Lett.*, 2005, **94**(14), 148101.

96 T. M. Konyakhina, S. L. Goh, J. Amazon, F. A. Heberle, J. Wu and G. W. Feigenson, *Biophys. J.*, 2011, **101**(2), L8–L10.

97 I. V. Ionova, V. A. Livshits and D. Marsh, *Biophys. J.*, 2012, **102**(8), 1856–1865.

98 S. Deol, P. Bond, C. Domene and M. Sansom, *Biophys. J.*, 2004, **87**(6), 3737–3749.

PAPER II

Segmental order parameters in a nonionic surfactant lamellar phase studied with ^{1}H–^{13}C solid-state NMR

Ferreira T. M., Medronho B., Martin R. W., and Topgaard D..

Segmental order parameters in a nonionic surfactant lamellar phase studied with ^{1}H–^{13}C solid-state NMR

Tiago Mendes Ferreira,[*a] **Bruno Medronho,**[ab] **Rachel W. Martin**[c] **and Daniel Topgaard**[*a]

A lyotropic nonionic lamellar system composed of pentaethyleneglycol mono *n*-dodecyl ether and D_2O was studied using natural abundance ^{13}C NMR under magic-angle spinning. Applying a two-dimensional recoupling method proposed by Dvinskikh (R-PDLF), ^{1}H–^{13}C dipolar couplings were estimated over a range of temperatures (300–335 K), thus enabling analysis of structural changes in the liquid crystalline system. The results obtained are used to correlate the conformation and mobility of local sites in the surfactant molecule with overall changes in the lamellar structure.

I. Introduction

The relationship between the phase transitions of lyotropic systems such as oligo(oxyethylene) surfactants in aqueous solutions and the microscopic variations of the molecules, *i.e.*, redistribution between conformational states due to changes in temperature and/or differences in concentration, has been the subject of a large number of studies.[1] Over the last three decades, ^{2}H NMR has proven to be a very useful tool for this purpose.[2–9] The measurement of the ^{2}H quadrupolar couplings provides an insight into the order profiles of C–D bonds and can reveal information about molecular orientation and motion in lipid membranes as well as other liquid crystalline systems.

The drawbacks of ^{2}H NMR spectroscopy methods result from the need for isotopic enrichment because of the low natural abundance (0.01%) of deuterium. Although tedious selective labeling of specific segments can be avoided by using fully ^{2}H labeled samples, this is at the expense of resolution due to overlap of the different ^{2}H Pake patterns in the spectrum. Various NMR methods have been developed to obtain the ^{13}C–^{1}H dipolar couplings as an alternative to the more traditional ^{2}H NMR spectroscopy.[10–16] These methods are less straightforward because the experiments are carried out under MAS. However, appropriate recoupling pulse sequences enable measurement of the heteronuclear dipolar couplings in an orthogonal dimension. This combines the high resolution of chemical sites provided by MAS with information about conformational and dynamical constraints.[17,18]

In this study, we probe a mixture of pentaethyleneglycol mono *n*-dodecyl ether (abbreviated as $C_{12}E_5$) and D_2O (57 wt% $C_{12}E_5$), in the temperature range 300–335 K, using

^{a} Department of Physical Chemistry 1, Lund University, P.O. Box 124, SE-221 00 Lund, Sweden. E-mail: Tiago.Ferreira@fkem1.lu.se; Daniel.Topgaard@fkem1.lu.se
^{b} Departamento de Química, Universidade de Coimbra, 3004-535 Coimbra, Portugal
^{c} Department of Chemistry, University of California, Irvine, CA 92697-2025, USA

a recoupling scheme proposed by Dvinskikh, called R-PDLF (R-type proton detected local field).[16] This scheme was recently used to probe the segmental order of lipid membranes.[19–21] Here, we apply the R-PDLF method for the first time to a surfactant system. According to the phase diagram reported by Imai *et al.*[22] the temperature range studied is within the lamellar phase region.

Every 2D NMR experiment is based on assembling 1D free induction decays from increasing times t_1 in the indirect dimension. The modulation of the signal depends on the anisotropic interactions chosen during this time period. The Hamiltonian terms ($H_{CSA} + H_{II} + H_{IS}$); H_{CSA}, chemical shift anisotropy, H_{II}, homonuclear dipolar coupling, H_{IS}, heteronuclear dipolar coupling; can be activated or deactivated during t_1, depending on the information that one wants to get from the indirect dimension.[23]

When performing MAS NMR the H_{CSA}, H_{II} and H_{IS} terms of the Hamiltonian are suppressed when the condition, *spinning frequency > interaction frequency* is met. This means achieving high resolution spectra at the expense of valuable information. A wide range of recoupling methodology under MAS has been proposed in the last two decades to selectively restore the information of the heteronuclear dipolar couplings.[13,15,18,24–28] In this study we use an R-type proton detected local field method (R-PDLF).

This experiment (Fig. 1) was proposed by Dvinskikh *et al.*[16] and results from the incorporation of an RF scheme, R18$_1^7$, presented by Zhao *et al.*,[15] into a proton detected local field (PDLF)[11] protocol. The R18$_1^7$ scheme allows the recoupling of heteronuclear dipolar couplings and chemical shift anisotropies (CSAs) while homonuclear dipole couplings are suppressed under MAS. The ^{1}H CSAs can be deactivated by a ^{13}C 180° pulse followed by a 180° shift of the first R18$_1^7$ block phase. Each R18$_1^7$ block consists of a repeated sequence of 180°$_{70}$180°$_{290}$ pulses, each one with a length of 1/18 of the rotor period. Increasing the time length t_1, modulates the effect of the dipolar field on each proton attached to a ^{13}C atom. This step is then followed by a polarization transfer from ^{1}H to ^{13}C using a rotor synchronized refocused INEPT (insensitive

Segmental order parameters in a nonionic surfactant lamellar phase studied with ^1H–^{13}C solid-state NMR
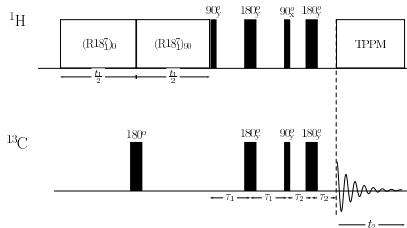

Fig. 1 Pulse sequences in the R-PDLF experiment. The dipolar couplings are activated during t_1 and modulate the amplitude of the isotropic chemical shifts during t_2.

nuclei enhanced by polarization transfer).[29,30] After this transfer, the free induction decay of the ^{13}C nuclei is recorded while applying TPPM[31] decoupling of the protons. Performing Fourier transformation in both the direct and indirect dimensions, a 2D spectrum is obtained that correlates the ^{13}C chemical shifts and the heteronuclear dipolar couplings.

The advantage of the R-PDLF over other recoupling schemes is that it enables measurement of the average dipolar field that the protons of a ^{13}C–H_x spin system experience from the rare ^{13}C nucleus during the time t_1. This is accomplished because the dipolar field that protons feel is most likely originated by a single ^{13}C nucleus (natural abundance of 1%), and due to the selectivity of the INEPT transfer. The splitting shown by a ^{13}C–^1H spin pair in an R-PDLF experiment is given by $\Delta v_{CH} = 0.315d_{CH}$, where 0.315 is an effective scaling factor and d_{CH} is the ^{13}C–^1H dipolar coupling. d_{CH} can be written as $d_{CH} = b_{CH}(3\cos^2\theta - 1)$, with $b_{CH} = -(\mu_0/4\pi) \times (\gamma_H\gamma_C\hbar/r^3)$ as the ^{13}C–^1H dipolar coupling constant and θ as the angle between the internuclear vector and the magnetic field. In the case of rapid motion due to conformational changes and/or diffusion of the molecules, the splitting, Δv, is proportional to the segmental order parameter $S_{CH} = \frac{1}{2}\langle 3\cos^2\theta - 1 \rangle$.

Temperature-dependent transitions from classical lamellar phases to random mesh phases or "porous" lamellar phases have been shown to exist in numerous studies.[6,9,22] It has been argued that the fluctuations of order parameters with temperature in nonionic surfactant mixtures can be interpreted as a measure of perforation density. In this paper we interpret the temperature dependence of the dipolar couplings from a simple conformational basis.

2. Experimental

2.1 Sample preparation

Pentaethylene glycol dodecyl ether ($C_{12}E_5$) with a purity higher than 99.8% was purchased from Nikko Chemical Co. (Tokyo, Japan). Deuterium oxide (D_2O) was obtained from Sigma Chemicals (Steinheim, Germany). Samples containing 57 wt% surfactant were prepared by weighing the desired amounts of surfactant and water into vials, mixing them in a vortex mixer and centrifuging them in order to remove air bubbles.

2.2 NMR measurements

The experiments were performed using a Bruker Avance AVII-500 NMR spectrometer operating at a ^1H frequency of 500.23 MHz equipped with a standard bore CP-MAS HX probe. All experiments were done at the spinning frequency of 5 kHz. The 2D NMR spectra were measured using the pulse sequence shown in Fig. 1 with the following parameters: spectral width of 100.4 ppm, $\tau_1 = 1.78$ ms and $\tau_2 = 1.19$ ms ($\tau_1 = \frac{1}{4J_{CH}}$ and $\tau_2 = \frac{1}{6J_{CH}}$ with $J_{CH} = 140$ Hz), power levels were set to give the following nutation frequencies: $R18_1^7$ pulses = 45.00 kHz, ^{13}C pulses = 63.45 kHz, ^1H INEPT pulses = 63.45 kHz, ^1H decoupling pulses = 25 kHz. t_1 increased up to 51.1488 ms taking values of 11.1 μs × m × 18 × 2 with m = 1,...,64, each $R18_1^7$ block being composed of 18 × $m\pi$ pulses of length 11.1 μs. For each t_1 value, 32 scans were measured with a recycle delay of 4 s. With a shorter delay, RF-heating could be detected *via* changes in chemical shift at the longest values of t_1. For each scan 10 098 time domain points were acquired using a spectral width of 100.4 ppm. The experiments were performed at temperatures 335, 330, 326, 323, 320, 317, 314, 310, 305 and 300 K in both increasing and decreasing directions. The temperature was calibrated using a methanol sample (see ref. 32 for more details). A 2D spectral processing scheme was applied. After Fourier transformation in both dimensions, each frequency domain signal in the indirect dimension was processed as follows. The zero frequency component in the indirect dimension was fixed as the value of the adjacent points. After inverse Fourier transform, sine-bell apodization and zero filling were performed on the time signal obtained. The frequency signal was recalculated and splittings measured. Because small splittings were obscured by the characteristic middle peak of the R-PDLF dipolar frequency signal (Fig. 2A), these were calculated directly from the time domain, using the expression, $\Delta v = 2/t_{min}$, where t_{min} is the position of the minimum in the time signal (Fig. 2B).

3. Results

Fig. 3 shows the ^{13}C NMR spectrum of a $C_{12}E_5$/water mixture with 57.7 wt% $C_{12}E_5$ at 300 K using the R-PDLF method. The peak assignments were made on the basis of previous reports for $C_{12}E_6$[33] and $C_{12}E_8$.[34] In the last one, it is shown that the highest band at approximately 70 ppm, corresponds to the interior chain of oxyethylene units (from the penultimate group to the most inner one) as the intensity of this band increases with increasing oxyethylene content. With respect to the assignment of the peaks to the carbons of the alkyl chain, C_1 (C_α), C_9, C_{10}, C_{11}, C_{12}, all of these were assigned as in the previous publications. The peak at 37 ppm that was previously assigned as being C_2 was here assigned as C_4. The new assignment was based on the assumption that the first derivative, $\partial\delta/\partial T$, of the chemical shifts as a function of temperature should decrease from C_1 to C_4 (Fig. 4).

Fig. 5 shows a contour plot of the relevant regions of a 2D spectrum taken at 335 K. The assignment of the partially overlapping peaks in both oxyethylene and alkyl carbon highest bands, 70 and 29 ppm, respectively, was based on
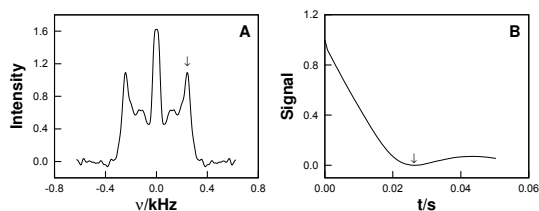
Fig. 2 (A) Frequency domain signal from C_3 and (B) time domain signal from C_{12}. The arrows show the maximum used to calculate splittings from the frequency domain, and the minimum used to calculate small splittings.
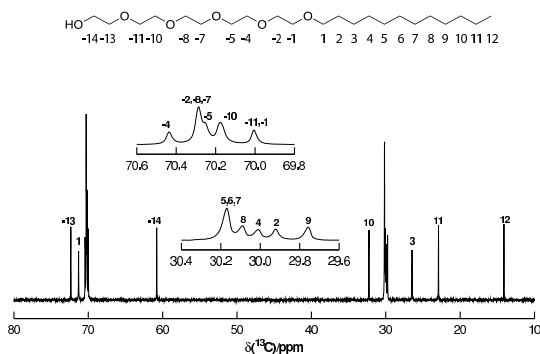

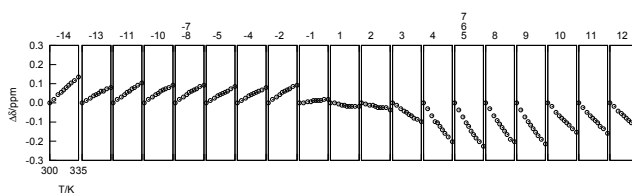**Fig. 3** ^{13}C NMR spectrum of a $C_{12}E_5/D_2O$ mixture with 57.7 wt% $C_{12}E_5$ at 300 K.

Fig. 4 Chemical shift dependence on temperature. $\Delta\delta = \delta - \delta_{300\ K}$. The numbers on top identify the different carbons.

the assumption that the splittings decrease in the direction of the terminal groups in agreement with previous ^2H NMR experimental results.[3,8]

The cause of the ordering for C–H bonds in the molecules can be split into three different classes (Fig. 6).

(I) **MAS effects** In static experiments, lamellar phases orient with the normal vector perpendicular to the magnetic field.[35] Under MAS, mechanical forces from the spinning dominate, giving rise to different distributions in the orientation of the lamellae. Even at equal MAS frequency values, a different averaging between orientations may be expected depending on the viscosity of the sample.

(II) **Lamellar phase morphology** The curvature of the individual lamellae will have an effect on the average orientation of the molecules.

(III) **Molecular mobility** On the single molecule level, the conformational distribution along the C–C and C–O bonds will produce different average orientations with respect to each ^1H–^{13}C–^1H spin system.

The effects described in I and II are unlikely to change much with temperature, provided the temperature change is not large enough to cause a phase transition, and they should produce a similar trend on the order parameters of the different segments. Therefore, comparison of the change in
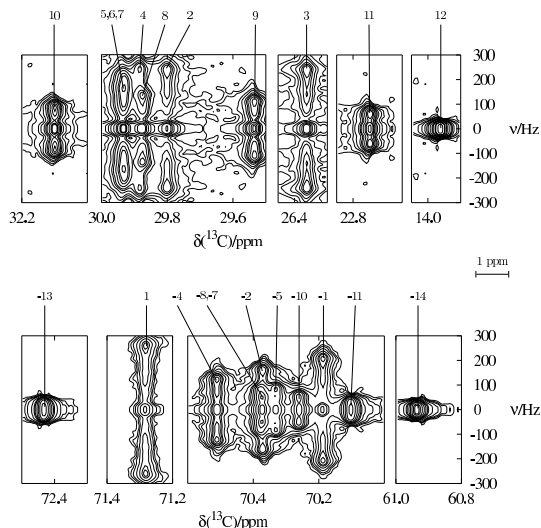
Segmental order parameters in a nonionic surfactant lamellar phase studied with ^1H–^{13}C solid-state NMR

Fig. 5 2D ^{1}H–^{13}C R-PDLF spectrum of a C$_{12}$E$_5$/D$_2$O mixture with 57.7 wt% C$_{12}$E$_5$ at 335 K.
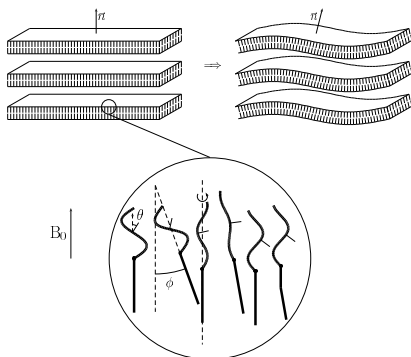

Fig. 6 Sketch illustrating the three types of orientational dependence of dipolar couplings referred to in the text. $\vec{n}$ represents the normal vector of the lamellar surface. ϕ is the tilting angle between the molecular axis and $\vec{n}$. It can be seen that θ, the angle between the C–H bond and the magnetic field, B$_0$, is dependent on the direction of $\vec{n}$, ϕ, and the conformation of the molecule. The arrow from left to right indicates the increase in lamellar undulation amplitude with temperature.

dipolar couplings with temperature provides information about conformational changes along the surfactant chain. These functions can be seen in Fig. 7.

Assuming that the ^{13}C–H bonds of the α carbon (labeled 1 in Fig. 3) have minor deviations with respect to the long axis direction of the molecule, then one can think of the C$_\alpha$ coupling magnitude as a measure of the lamella curvature. In fact, this assumption, combined with results obtained using other techniques,[22] has been the basis of a large number of ^{2}H NMR studies,[6,9,36] where the maximum of the C$_\alpha$ quadrupolar coupling as function of temperature was interpreted as the transition of the lamellar phase, L$_\alpha$, to a porous lamellar phase, L$_\alpha^H$. As the curvature is related to the degree of hydration, then the C$_\alpha$ splitting is mainly dependent on the fraction of hydrated EO units. Surprisingly, it was shown by Baciu *et al.* that the quadrupolar splitting from heavy water in a C$_{12}$E$_5$/D$_2$O system, is directly proportional to the splitting obtained from an α-deuterated surfactant.[9]

Experimental results[8,37–39] as well as theoretical models,[40,41] molecular dynamics[42] and Monte Carlo simulations[43] predicted that the lowest energy conformations for the –OCCO– segments correspond to a *gauche* conformation around the C–C bond and *anti* around the C–O bond. This is the dominant conformation at low temperature but with a low statistical weight over the complete set of possible conformations and it has the highest dipole moment of all conformers.[44,45] Also, it has been shown that the fraction of EO units in the C–C *gauche* conformation is dependent on the water content.[8,46] At higher temperature, conformations with low dipole moment become more populated as well as zero dipole moment *trans* conformations. This results in an increase of the order in the oxyethylene chains and the solute–solute interaction becomes more favorable than the solute–polar solvent
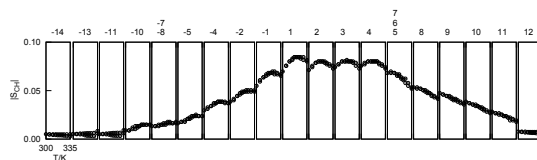
100

Fig. 7 Order parameters of the different C–H bonds in $C_{12}E_5/D_2O$ (lamellar phase with 57 wt% of surfactant) as function of temperature. Measurements obtained in both increasing and decreasing temperature directions are plotted.

interaction. It is then straightforward to interpret the increase in the splitting of the oxyethylene carbons (Fig. 7) as being a consequence of the higher order proportioned by this change in the conformation distribution.

At higher temperatures, the decrease in splitting of the EO C-H bonds is expected. The fast motion of the molecules and the increase in amplitude undulations of the lamellar phase[47,48] oppose the effect of dehydration (Fig. 6). From a close inspection of the functions (-10 to 5), in Fig. 7 one can see that a maximum appears. Also, one can see a shift in the temperature value of the maximum, which decreases in the direction of the outer hydrophobic segments. The behavior of the hydrophobic tails with temperature is opposite to that of the headgroups, as can be seen in Fig. 7. At higher temperature the population of *gauche* conformations increases with the concomitant decrease of the order parameter. This suggests that the maximum in the α carbon, previously interpreted as being a consequence of a mesh phase, may have a simpler explanation, that is the compromise between the opposite trends of the EO and tail groups.

The balance between the contraction (*trans* → *gauche*) and extension (*gauche* → *trans*) of the tail and headgroup, respectively, with increasing temperature, agrees with the observation that the thickness of the lamella remains nearly constant with temperature.[49] This conformational behavior is also observed in the chemical shifts, as, with increasing temperature, the chemical shifts of the headgroup carbons decrease while in the tail carbons an increase is observed (Fig. 4) as already had been pointed out by Ahlnäs *et al.*[38]

4. Conclusion

The R-PDLF method offers a complete S_{CH} analysis of the L_α surfactant liquid crystalline systems. The maximum observed for the α-labeled $C_{12}E_5$ was previously interpreted as a mesh phase. A complete S_{CH} profile suggests that the maximum observed for the central region may be a consequence of the opposing trends for the alkyl and oxyethylene parts.

Acknowledgements

References

1 P. Alexandridis and B. Lindman, *Amphiphilic Block Copolymers (Self-Assembly and Applications)*, Elsevier Science BV, Amsterdam, 2000.
2 J. P. Douliez, A. M. Bellocq and E. J. Dufourc, *J. Chem. Phys.*, 1994, **91**, 874.
3 W. Schnepp and C. Schmidt, *Ber. Bunsen-Ges. Phys. Chem.*, 1994, **98**, 248.
4 M. Lukaschek, S. Müller, A. Hasenhindl, D. A. Grabowski and C. Schmidt, *Colloid Polym. Sci.*, 1996, **274**, 1.
5 F. Auguste, J. P. Douliez, A. M. Bellocq and E. J. Dufourc, *Langmuir*, 1997, **13**, 666.
6 C. E. Fairhurst, M. C. Holmes and M. S. Leaver, *Langmuir*, 1997, **13**, 4964.
7 S. Müller, C. Börschig, W. Gronski, C. Schmidt and D. Roux, *Langmuir*, 1999, **15**, 7558.
8 A. Tonegawa, K. Ohno, H. Matsuura, K. Yamada and T. Okuda, *J. Phys. Chem. B*, 2002, **106**, 13211.
9 M. Baciu, U. Olsson, M. S. Leaver and M. C. Holmes, *J. Phys. Chem. B*, 2006, **110**, 8184.
10 M. Munowitz, R. G. Griffin, G. Bodenhausen and T. H. Huang, *J. Am. Chem. Soc.*, 1981, **103**, 2529.
11 D. P. Weitekamp, J. R. Garbow and A. Pines, *J. Chem. Phys.*, 1982, **77**(6), 2870.
12 Y. K. Lee, N. D. Kurur, M. Helme, O. G. Johannessen, N. C. Nielsen and M. H. Levitt, *Chem. Phys. Lett.*, 1995, **242**, 304.
13 J. D. Gross, D. E. Warchawski and R. G. Griffin, *J. Am. Chem. Soc.*, 1997, **119**, 796.
14 M. Caravetta, M. Edén, X. Zhao, A. Brinkmann and M. H. Levitt, *Chem. Phys. Lett.*, 2000, **321**, 205.
15 X. Zhao, M. Edén and M. H. Levitt, *Chem. Phys. Lett.*, 2001, **342**, 353.
16 S. V. Dvinskikh, H. Zimmermann, A. Maliniak and D. Sandström, *J. Magn. Reson.*, 2004, **168**, 194.
17 A. E. Bennet, R. G. Griffin and S. Vega, in *NMR Basic Principles and Progress*, Springer-Verlag, Berlin Heidelberg, 1994, vol. 33, pp. 3–77.
18 M. H. Levitt, *J. Chem. Phys.*, 2008, DOI: 10.1063/1.2831927.
19 S. V. Dvinskikh, V. Castro and D. Sandström, *Phys. Chem. Chem. Phys.*, 2005, **7**, 607.
20 V. Castro, S. V. Dvinskikh, G. Widmalm, D. Sandström and A. Maliniak, *Biochim. Biophys. Acta*, 2007, **1768**, 2432.
21 C. Leal, D. Sandström, P. Nevsten and D. Topgaard, *Biochim. Biophys. Acta*, 2008, **1778**, 214.
22 M. Imai, A. Saeki, T. Teramoto, A. Kawaguchi, K. Nakaya, T. Kato and K. Ito, *J. Chem. Phys.*, 2001, **115**, 10525.
23 D. D. Laws, H. L. Bitter and A. Jerschow, *Angew. Chem., Int. Ed.*, 2002, **41**, 3096.
24 T. G. Oas, R. G. Griffin and M. H. Levitt, *J. Chem. Phys.*, 1988, **89**, 1988.
25 T. Gullion and J. Schaefer, *J. Magn. Reson.*, 1989, **81**, 196.
26 J. C. C. Chan and H. Eckert, *J. Chem. Phys.*, 2001, **115**, 6095.
27 M. H. Levitt, in *Encyclopedia of Nuclear Magnetic Resonance: Supplementary Volume*, ed. D. M. Grant and R. K. Harris, Wiley, Chichester, UK, 2002.

Phys. Chem. Chem. Phys., 2008, **10**, 6033–6038 | **6037**

101

28 X. Zhao, W. Hoffbauer, J. S. auf der Günne and M. H. Levitt, *Solid State Nucl. Magn. Reson.*, 2004, **26**, 57.

29 G. A. Morris and R. Freeman, *J. Am. Chem. Soc.*, 1979, **101**, 760.

30 J. D. Gross, P. R. Costa, J. P. Dubacq, D. E. Warchawski, P. N. Lirsac, P. F. Devaux and R. G. Griffin, *J. Magn. Reson., Ser. B*, 1995, **106**, 187.

31 A. E. Bennet, C. M. Rienstra, M. Auger, K. V. Lakshmi and R. G. Griffin, *J. Chem. Phys.*, 1995, **103**, 6051.

32 A. L. V. Geet, *Anal. Chem.*, 1970, **42**, 679.

33 L. Zheng, M. Suzuki, T. Inoue and B. Lindman, *Langmuir*, 2002, **18**, 9204.

34 A. A. Ribeiro and E. A. Dennis, *J. Phys. Chem.*, 1977, **81**, 957.

35 P. Quist, B. Halle and I. Furó, *J. Chem. Phys.*, 1991, **95**(9), 6945.

36 B. Medronho, M. G. Miguel and U. Olsson, *Langmuir*, 2007, **23**, 5270.

37 V. Viti and P. Zampetti, *Chem. Phys.*, 1973, **2**(2), 233.

38 T. Ahlnäs, G. Karlström and B. Lindman, *J. Phys. Chem.*, 1987, **91**, 4030.

39 S. A. Wahab and H. Matsuura, *Chem. Lett.*, 2001, **3**, 198.

40 M. Andersson and G. Karlström, *J. Phys. Chem.*, 1985, **89**, 4957.

41 G. Karlström, *J. Phys. Chem.*, 1985, **89**, 4962.

42 S. Bandyopadhyay, M. Tarek, M. L. Lynch and M. L. Klein, *Langmuir*, 2000, **16**, 942.

43 Y. C. Kong, D. N. N. G. Parsonage and L. Thompson, *J. Chem. Soc., Faraday Trans.*, 1994, **90**(16), 2375.

44 B. Lindman, A. Carlsson, G. Karlström and M. Malmsten, *Adv. Colloid Interface Sci.*, 1990, **32**, 183.

45 G. Karlström and B. Lindman, in *Organized Solutions*, ed. S. E. Friberg and B. Lindman, Marcel Deker, Inc., New York, 1992, pp. 49–65.

46 O. Engkvist and G. Karlström, *J. Phys. Chem. B*, 1997, **101**, 1631.

47 W. Helfrich, *Z. Naturforsch.*, 1978, **33a**, 305.

48 H. Bagger-Jörgensen and U. Olsson, *Langmuir*, 1996, **12**, 4057.

49 K. Minewaki, T. Kato, H. Yoshida, M. Imai and K. Ito, *Langmuir*, 2001, **17**, 1864.